Lehrstuhl für Hochfrequenztechnik
Technische Universität München

Analysis of Space-Borne Antennas by Higher-Order Method of Moments and Inverse Equivalent Current Methods

Ismatullah

Vollständiger Abdruck der von der Fakultät für Elektrotechnik und
Informationstechnik der Technischen Universität München zur Erlangung des
akademischen Grades eines

– *Doktor-Ingenieurs* –

genehmigten Dissertation.

Vorsitzender:	Univ.-Prof. Dr.-Ing. habil. Dr. h.c. Alexander W. Koch
Prüfer der Dissertation:	1. Univ.-Prof. Dr.-Ing. Thomas Eibert
	2. Univ.-Prof. Dr. techn. Wolfgang Rucker, Universität Stuttgart

Die Dissertation wurde am 21.01.2010 bei der Technischen Universität
München eingereicht und durch die Fakultät für Elektrotechnik und
Informationstechnik am 13.04.2010 angenommen.

To
Prophet Jesus
Whose Return is Promised
to Accomplish the Law of
His Brother Prophet Muhammad
(*Peace and Blessing of ALLAH be upon Them All*).

Acknowledgment

All praises be to ALLAH Almighty who sent His messengers for the guidance of mankind to recognize the hidden truths of the universe in order to be eligible for everlasting success. To be brought into being while bearing witness about Muhammad (*peace and blessing of ALLAH be upon him*) as His final messenger is His exceptional blessing which has been bestowed without any effort. The work carried out in the past few years and presented in this text would have never been possible without His Kindness.

The work presented in this text was carried out at Institute of Radio Frequency Technology, Universität Stuttgart, Stuttgart, Germany and Lehrstuhl für Hochfrequenztechnik, Technische Universität München, Munich, Germany under the collaborative Ph.D. scholarship scheme between Higher Education Commission of Pakistan and Deutscher Akademischer Austausch Dienst, Germany. Their sponsorship for this work is strongly accredited.

The accomplishment of this contribution would have never been successful without the concrete and authentic advices of Prof. Dr.-Ing. Thomas Eibert at each and every step. While living far away from the family, the compassionate care by Prof. Eibert was never less than the paternal sympathy. In all ups and downs of the time span spent in Germany, his motivation was always optimistic. I express my heartiest gratitudes to Prof. Eibert for his special kindness for which i don't find suitable words for their complete expression.

Nevertheless, prayers, wishes and motivation of my parents, sisters, brothers, friends and colleagues serve as the foundations in the successful completion of my studies. The appreciation that I get from Rukhsana, Najm, Anis, Atiq, Fehmeeda, Mother and Father during this tough time is unforgettable. Moreover, I must say thanks to all my colleagues from Stuttgart and Munich who always put their own work aside to resolve my issues. I am specially grateful to Yves Mutschelknaus from Stuttgart and Dr.-Ing. Uwe Siart from Munich for their valuable supports. The friendship of Abdul Aziz and Atif Shahbaz has always played significant role in stepping a step forward during the course of tough times often encountered during the present work. Very rarely one meets a person in his life who grasps all emotions and affections. The deeply engraved support of Diana Jefišova during the course of this work can never be forgotten. Finally thanks go to all those who contributed in various ways in this work but couldn't appear here, they live in my heart.

Abstract

Modern radio, wireless, and satellite communication and radar systems often require accurate and efficient modeling, analysis, and/or synthesis of the electrically large, uniquely designed beam pattern antennas operating in the presence of geometrically complex environments. The electromagnetic analysis and synthesis of such electrically large and complex structures pose a challenging problem in terms of computer resources.

In the work being presented here, the efficient and accurate analysis of the radiation and scattering problems for arbitrarily shaped perfect electrically conducting (PEC) as well as impedance boundary objects have been accomplished by solving the numerically exact surface integral equation (IE) formulations through the method of moments (MoM), where the adaptive singularity cancellation technique based near-coupling evaluation, higher-order (HO) modeling of the surface current densities, and the efficient storage capability of the $\hat{k}$-space representations of spherical harmonics expansion (SE) based multilevel fast multipole method (MLFMM) have played significant role. The synthesis of specialized antennas with uniquely designed tailor-made beam patterns have been considered using inverse equivalent current method (ECM), where HO basis functions have been incorporated in the modeling of unknown surface current densities.

The near-coupling double surface integrals encountered in the MoM solution of IEs, need special treatment for their accurate evaluation because of the singular nature of the integrand which involves Green's function. Singularity cancellation technique with the adaptive choice of quadrature points in the evaluation of interaction between a neighboring pair of planar source and test domains has major contribution towards the efficient and accurate evaluation of the near interactions. The low-order (LO) Rao-Wilton-Glisson (RWG) basis functions, despite their widespread usage in the expansion of unknown surface current densities suffer from the fundamental shortcoming that often dense geometrical discretization is necessary for sufficiently good accuracies. With the implementation of hierarchical HO basis functions in the mixed order formulation in the modeling of surface current densities, better accuracies with given number of unknowns compared with the LO counterparts have been achieved. Further, sufficient reduction in the number of unknowns for a given problem and same accuracy has also been observed with HO modeling. Large scale problems are hardly solvable without the proper use of fast solvers like the fast multipole method (FMM) or its associated multilevel version MLFMM. Unfortunately the traditional MLFMM approaches become less efficient with HO due to their larger element dimensions. In contrast, the SE-MLFMM considerably reduces the usual high memory demands of traditional MLFMM with HO, because of the efficient storage of the $\hat{k}$-space representations of the individual basis functions, and hence allows for very efficient iterative solution of the resulting equation system.

The inverse equivalent surface currents on the surface of an exemplary paraboloidal reflector have been investigated from the knowledge of a custom made radiation pattern through the use of inverse equivalent current method (ECM). For the realization of thus obtained equivalent surface currents, a few propositions have also been discussed to be carried out in future. The technique considered here may serve as a future candidate in the synthesis of antenna structures for customized radiation characteristics.

Table of Contents

List of Figures

List of Tables

List of Abbreviations

Abbreviation	Description
ABC	Absorbing boundary condition
Bi-RCS	Bistatic RCS
BVP	Boundary value problem
CFIE	Combined field integral equation
ECM	Equivalent current method
EFIE	Electric field integral equation
FDTD	Finite-difference time-domain
FEBI	Finite-element boundary integral
FEM	Finite element method
F-GMRES	Flexible-GMRES
FMM	Fast multipole method
GMRES	Generalized minimal residual algorithm
GO	Geometrical optics
GTD	Geometrical theory of diffraction
HO	Higher order
IBC	Impedance boundary condition
IE	Integral equation
ISB	Incident shadow boundary
LMS	Least mean square
LO	Low order
MFIE	Magnetic field integral equation
MLFMA	Multilevel fast multipole algorithm

Abbreviation	Description
MLFMM	Multilevel fast multipole method
MoM	Method of moments
PDE	Partial differential equation
PEC	Perfect electric conductor
PML	Perfectly matched layer
PO	Physical optics
PTD	Physical theory of diffraction
RA-R^2	Radial angular-R^2
RMS	Root mean square
RSB	Reflection shadow boundary
RWG	Rao-Wilton-Glisson
SE	Spherical harmonics expansion
SE-MLFMM	SE based MLFMM
UTD	Uniform theory of diffraction

1 Introduction

Modern advent in science and technology is undoubtedly by virtue of the significant role of Mathematics which enabled scientists and technologists to solve complex problems. Significant contributions of Al-Khwarizmi in the first systematic solution of linear and quadratic equations [1], of Newton in the better understanding of physical laws of mechanics, of Navier and Stokes in the realm of physics of fluids, and of Maxwell in the theory of electromagnetics are a few to mention [2]. With the knowledge that most of the governing mathematical formulations, which are typically partial differential equations, for the representation of physical behavior of devices and systems encountered in various branches of science and engineering have no closed form solution, mathematicians have been looking for the numerical means to solve such governing principles.

Electromagnetic devices and systems e.g. television, radio, satellite communication systems, radar systems, medical imaging systems, electrical power networks, and many more are essential elements of modern era. Undoubtedly, electromagnetic phenomena have a profound impact on contemporary society. The understanding of electromagnetic phenomena is treated by electromagnetics which describes interaction between sources (charges and currents) and field quantities and is governed by Maxwell's equations. As analytical solutions in closed form are known for only a very limited number of special cases, which hardly ever are directly applicable to real-world applications, numerical solutions are often sought for such purposes. Furthermore, large scale and complex problems often pose challenging constraints for their efficient and accurate treatment [3]. Examples include design and analysis of gigantic reflector antennas for radio astronomy observatories, sonar and radar tracking and identification of full-size ships and airplanes, propagation of communication signals in complex environments, modeling of antennas on vehicles, mine location, and geophysical remote sensing. These problems may involve models with millions of unknowns. With the advent of modern fast and efficient computational resources together with the availability of efficient solution strategies (e.g. [4–7]), the large scale practical problems have become possible to be addressed in a profound way. Computational electromagnetics therefore plays significant role in faster and cost effective design of modern electromagnetic systems by minimizing the use of time-consuming and expensive experiments with prototypes.

The traditional way to solve ultra-large problems when the sizes are many orders of wavelengths is to use high frequency asymptotic methods such as physical optics, geometrical theory of diffraction etc. [8, 9]. However, because of underlying approximations made by asymptotic methods in the governing Maxwell's equations, their use is limited for some simpler problems. Furthermore, the error incurred in these methods cannot be systematically controlled through enhancements in memory and computations resources [10]. More precise treatments are possible with the aid of so-called full-wave techniques such as finite-difference time-domain (FDTD), finite element method (FEM) and method of moments solution of surface integral equations.

The matrix system associated with surface integral equation methods are usually dense whereas the differential equation solvers result in sparse matrix system which greatly reduce the storage requirements. However, for impenetrable scatterers, the advantage of solving a surface integral equation is that often the unknown quantity (for present course of work it is current source $\boldsymbol{J}$) resides on a 2D surface, whereas in case of differential equation solvers the unknown quantity (which can be field $\boldsymbol{E}$) fills the whole 3D space. Consequently, for large problem sizes, more unknowns are required to be solved with a differential equation compared to a surface integral equation [11]. In the present work, surface integral equation formulations have been opted for the treatment of problem under-consideration and have been reviewed in chapter 3.

In method of moments solution of integral equation formulations, the singular nature of integrand requires proper treatment for the evaluation of the integrals involved. The Duffy method [12], the singularity subtraction approach [13–17], regularization techniques [18, 19], and the singularity cancellation approaches [20–22] are among the popular techniques. The aim of the work presented here has been to develop a general purpose solver suitable for the solution of radiation and scattering problems of arbitrarily shaped open as well as closed surfaces composed of metallic and dielectric materials, where the unknown current densities are modeled with higher order polynomial expansion functions to achieve higher accuracies. For this purpose, the singularity cancellation technique which is a purely numerical treatment has been improved to its adaptive version [22–24] and has therefore been opted as a tool for the treatment of singular integrals in the surface integral equation formulations. Detailed discussion can be found in chapter 4.

In the MoM solution of integral equation formulations, the low-order basis based modeling of the unknown current density requires the average size of the surface and/or volumetric geometrical elements on the order of $\frac{\lambda}{10}$ in each dimension, λ being the wavelength in the medium. This results in a very large number of unknown current/field expansion coefficients [25–31]. Furthermore, the accuracy of the solution while using the LO bases is improved slowly with increasing the number of unknowns. Great reduction of the number of unknowns for a given problem and desired accuracy is achievable through the use of higher-order basis functions [25–33]. In our implementation, nearly-orthogonal set of field basis functions [29, 30] for flat triangles is our choice for possibly better conditioned system matrix. Moreover, the curl-free components of first-order and curl space of the second-order were added to the existing low-order RWG [34] bases, which makes the formulation complete to full first order with respect to the curl of the basis functions. More discussion on higher order basis functions can be found in chapter 5.

In the standard fast multipole method and multilevel fast multipole method approaches [3,5,35,36], based on edge-to-edge interactions, the minimum FMM group size and the number of FMM levels are limited by the size of the largest elements in the geometrical modeling of the object, as long as the group sizes are larger than that dictated by the so-called low-frequency breakdown of FMM [5]. Now because of the larger element size with the HO basis functions, the FMM group size is larger than that with LO basis functions. Equivalently, fewer number of FMM levels are permissible which in turn restricts full utilization of the MLFMM memory and computational efficiencies for high-frequency applications, where the basis function density is kept as low as possible. A point-based multilevel fast multipole algorithm (MLFMA) [37], as an example, has tackled this problem by considering the point-to-point interactions permitting two more FMM levels compared to the traditional basis-based MLFMM. However, the spherical harmonics expansion based MLFMM [6] is inherently more efficient in terms of memory and computational cost even with edge-to-edge interactions due to the efficient storage of the k-space representations of the individual basis functions. SE-MLFMM has therefore been utilized in the current implementation to accelerate the HO bases based MoM solution of IEs. A review of SE-MLFMM for HO basis can be seen in section 5.5.

In various applications of practical interest, e.g. antenna pattern measurements, synthesis of antennas with customized radiation pattern etc., the investigation of the radiated fields or the equivalent electric/magnetic surface currents on the object surface from the knowledge of electric/magnetic near-field intensities defined on an arbitrary grid around the object under test is often desired. The aim of this task is to determine surface current sources such that their radiated fields best fit with the field strengths given at certain grid of sample points. Out of various techniques available in the literature (e.g. [38,39]), the inverse equivalent current methods e.g. [40,41] etc. are most attractive because of their diverse applicability and robustness in the solution accuracies. The Huygens equivalent surface currents defined on the object under consideration have therefore been investigated to account for the known near-field characteristics using method of moments like solution strategy for the governing integral equation. High efficiency has been achieved through the application of SE-MLFMM and better accuracy was possible with higher-order modeling of current densities. This is presented in chapter 6.

Synthesis of antenna structures for tailor-made radiation characteristics is often appreciated in radar systems and satellite communications. Customizations such as improvement/reduction in radiated power in certain directions, pattern shaping etc., have been typically obtained (e.g. [42–44]) with the aid of optimization algorithms (e.g. [45–49]). In the present work, investigation has been made in the reconstruction of reflector surface currents for customized radiation pattern through the use of inverse equivalent current method. Radiated fields which construct the desired radiation pattern have been first mapped to the Huygens surface current on the surface of a preliminarily designed parabolic surface. For the realization of thus obtained equivalent surface currents, a few propositions have been discussed to be carried out in future. This is discussed in chapter 7.

2 Basics of Electromagnetics

In order to investigate the electromagnetic behavior of a system, numerous computational methods can be found in literature where the solution of governing Maxwell's partial differential equations is sought. Some of these methods, such as the asymptotic methods, solve an approximation of the Maxwell equations. Others seek numerical solutions for exact Maxwell's equations or a set equivalent to them. The latter methods e.g. integral equation methods and finite element methods are the most widely used approaches. In this chapter, some of well-known techniques of computational electromagnetics are reviewed.

2.1 Maxwell's Equations

The Maxwell's Equations are a set of fundamental equations governing the behavior of electromagnetic fields. These equations are functions of space and time and are given below[1].

Faraday's law:

$$\nabla \times \boldsymbol{E} = -\mu \frac{\partial \boldsymbol{H}}{\partial t} \tag{2.1}$$

Maxwell-Ampère law:

$$\nabla \times \boldsymbol{H} = \epsilon \frac{\partial \boldsymbol{E}}{\partial t} + \boldsymbol{J} \tag{2.2}$$

Gauss's law:

$$\nabla \cdot \epsilon \boldsymbol{E} = \rho \tag{2.3}$$

Gauss's law for Magnetism (absence of magnetic monopoles):

$$\nabla \cdot \mu \boldsymbol{H} = 0 \tag{2.4}$$

---

[1] The original Maxwell's equations were expressed in some 20 equations [11]. It was Heaviside [50, 51] who distilled Maxwell's equations into the four equations.

Equation of Continuity (Law of conservation of charge): The equation of continuity is another fundamental equation, which can be derived from (2.2) and (2.3).

$$\nabla \cdot \boldsymbol{J} = -\frac{\partial \rho}{\partial t}\,, \tag{2.5}$$

where

$\boldsymbol{E}$ = electric field intensity (Volt per meter)
$\boldsymbol{H}$ = magnetic field intensity (Ampere per meter)
ρ = free electric charge density (Coulomb per cubic meter)
$\boldsymbol{J}$ = free current density (Ampere per square meter)
ϵ = permittivity of the medium (Farad per meter)
μ = permeability of the medium (Henry per meter)
σ = conductivity of the medium (Siemens per meter).

The constitutive parameters (ϵ, μ, σ) are scalar quantities in isotropic media and tensor quantities in anisotropic media. Similarly, these parameters are independent of position in case of homogeneous media and dependent on position in case of inhomogeneous media. The charge and current densities ρ, $\boldsymbol{J}$ may be considered as the sources of the electromagnetic fields $\boldsymbol{E}$, $\boldsymbol{H}$ and does not include any induced polarization charges and currents [52]. For wave propagation problems, these densities are localized in space; for example, they are restricted to flow on an antenna. The generated electric and magnetic fields are radiated away from these sources and can propagate to large distances to the receiving antennas. Away from the sources, that is, in source-free regions of space, ρ and $\boldsymbol{J}$ vanish in Maxwell's equations.

Field quantities $\boldsymbol{E}$ and $\boldsymbol{H}$ in above equations are dependent on spatial ($\boldsymbol{r}$) and temporal (t) coordinates. When field quantities in Maxwell's equations are harmonically oscillating functions with a single frequency, say ω, the field is referred to as *time-harmonic*. Using Fourier analysis, any time-varying field can be expressed in terms of time-harmonic components. Assuming that the time portion of the vector fields $\boldsymbol{E}$ and $\boldsymbol{H}$ is the fundamental harmonic in a Fourier series, the electric and magnetic fields may take the form

$$\boldsymbol{E}\left(\boldsymbol{r},t\right) = \boldsymbol{E}\left(\boldsymbol{r}\right)e^{j\omega t} \quad \text{and} \quad \boldsymbol{H}\left(\boldsymbol{r},t\right) = \boldsymbol{H}\left(\boldsymbol{r}\right)e^{j\omega t}\,. \tag{2.6}$$

The time factor $e^{j\omega t}$ divides out of Maxwell's equations so that (2.1), (2.2), and (2.5) can be written in simplified form as

$$\begin{aligned} \nabla \times \boldsymbol{E} &= -j\omega\mu\boldsymbol{H} \qquad (2.7) \\ \nabla \times \boldsymbol{H} &= j\omega\epsilon\boldsymbol{E} + \boldsymbol{J} \qquad (2.8) \\ \nabla \cdot \boldsymbol{J} &= -j\omega\rho \qquad (2.9) \end{aligned}$$

2.2 Computational Electromagnetics

The Maxwell equations (2.7)-(2.9) are a set of first-order partial differential equations connecting the temporal derivatives of vector fields namely $\boldsymbol{E}$ and $\boldsymbol{H}$ to their partial spatial derivatives. As any partial differential equation or a set of partial differential equations, the Maxwell's equations are satisfied by an infinite number of solutions. But unique solution to a problem may be obtained by enforcing the appropriate initial and boundary conditions [25, 53]. Initial conditions define that the field quantities are impressed in a given volume at an initial time. Boundary conditions define that at any instant of time the field quantities are impressed upon the whole surface enclosing the given volume. In order to avoid any unphyiscal solution, the solutions of Maxwell's equations are also subject to the Sommerfeld radiation condition [54]. Mathematically speaking, the electric and magnetic fields have to satisfy the following condition at infinity [25,55]

$$\lim_{r\to\infty} r \left[\nabla \times \begin{pmatrix} \boldsymbol{E} \\ \boldsymbol{H} \end{pmatrix} + jk_0\hat{r} \times \begin{pmatrix} \boldsymbol{E} \\ \boldsymbol{H} \end{pmatrix} \right] = 0, \qquad (2.10)$$

where k_0 is the free space wave number, $r = |\boldsymbol{r}|$ is the magnitude of position vector $\boldsymbol{r}$ and $\hat{r} = \frac{\boldsymbol{r}}{r}$ gives its direction. With the enforcement of Sommerfeld radiation condition (2.10), only the solution which corresponds to the fields radiating from sources to infinity is filtered out and all other unphysical solutions, e.g. corresponding to the energy coming from infinity and sinking in sources, are rejected.

Unfortunately, Maxwell's equations can be solved analytically only for a very few idealized geometries of scattering/radiating structures [55]. For example, when a linear antenna can be approximated as an infinitesimally short current element or a finite wire with a known current distribution, its radiated field can be calculated analytically. When a biconical antenna is assumed to extend to infinity, its radiated field and input impedance can also be obtained analytically. Without an approximation, antennas cannot be analyzed analytically primarily because of their structural configurations. Whereas a variety of approximate analytical techniques have been developed for relatively simple geometries, accurate and complete analysis of complex structures can be accomplished only through a numerical method that solves Maxwell's equations numerically with the aid of high-speed computers.

Almost all numerical approaches in solving Maxwell's equations find the fields in either the time domain or frequency domain. Time-domain models contain many frequencies and can model transient behavior. On the other hand, frequency-domain methods calculate solutions for one frequency at a time and are appropriate for steady-state behavior. According to [55], it is difficult to model nonlinear devices/media accurately using a frequency-domain-based method. Fourier transforms allow transforming between the two domains.

Most numerical methods discretize the unknown quantity (fields or currents) in spatial and/or temporal domains. The Nyquist rate requires sampling the waveform at at least twice the highest frequency. However, due to the presence of sharp corners or other singular geometrical features of the scatterer, variations in the surface current with higher spatial frequency may occur [56]. Generally, the accuracy of the solution is related to the discretization. Usually the finer the discretization, the better the accuracy of the solution but at the cost of increased solution time. However, experiments imply a consideration of some lower limit on the element size or equivalently maximum number of unknowns or basis functions in a given problem. The discretization of about 10 subdivisions per wavelength results in the condition number of the system matrix typically smaller than 100, which increases badly for finer discretization [57, 58]. Therefore, in most cases, discretization of the order of $\lambda/10 - \lambda/20$ is chosen as the element size for good accuracies. Furthermore, the numerical solutions of some[2] integral equations begin to lose the accuracy or even fail in the frequency region when the wavelength is much larger than the dimensions of the structure – a phenomenon known as the *low-frequency breakdown* (e.g. [58–61]). The reason for low-frequency breakdown is usually traced in the different frequency scaling of the magnetic vector potential part and the electric scalar potential part in the mixed-potential formulation of the electric field integral equation. When the frequency is sufficiently low, the magnetic vector potential contributions almost vanish in the moment matrix and the remaining scalar potential contributions depend only on the $\nabla \cdot \boldsymbol{J}$. The knowledge of $\nabla \cdot \boldsymbol{J}$ is not sufficient to determine $\boldsymbol{J}$ which results in inaccurate solutions in the low frequency region [59]. As a remedy to the low frequency breakdown, loop-star and loop-tree basis decomposition method for

---

[2] Electric field integral equations suffer from low-frequency breakdown [59], whereas magnetic field integral equations can be solved at an arbitrarily low frequency without encountering this low-frequency breakdown [60].

RWG basis functions were introduced for EFIE [59, 61], which represent two kinds of physical currents at low frequencies.

Variety of numerical treatments for the solutions of Maxwell's equations are available in literature [62–67]. The most commonly encountered methods for numerically finding the solution of electromagnetic problems are briefly reviewed below.

2.2.1 High-Frequency Methods

High-frequency methods assume the wavelength approaches zero which works well when applied to very large objects (at least a few order of wavelengths). These high-frequency methods and hence their solutions are also known as asymptotic in the sense that their accuracy increases as some characteristic dimension associated with the scatterer becomes electrically large with increasing frequency.

A well-known high-frequency method is geometrical optics (GO) [68–73], also known as ray tracing, in which the electromagnetic rays, which are trajectories orthogonal to the phase fronts (in an isotropic medium), travel in straight lines (in a homogeneous medium) and their direction is governed by so-called Snell's law[3]

$$n_1 \sin\theta_1 = n_2 \sin\theta_2\,, \tag{2.11}$$

where, θ_1 and θ_2 are the angles subtended by the two rays with the surface normal at the media interface. n_1 and n_2 are the indices of refraction in two media. The GO field behaves locally like a plane wave at any point $\boldsymbol{r}$. Geometrical optics however, ignores diffraction effects.

Another most frequently encountered high frequency method, known as physical optics (PO), also viewed as a wave optical method [71–73], computes approximate surface currents from the tangential components of incident magnetic fields

$$\boldsymbol{J}_s = \begin{cases} 2\hat{n} \times \boldsymbol{H}\,, & \text{illuminated region,} \\ 0\,, & \text{elsewhere,} \end{cases} \tag{2.12}$$

where $\hat{n}$ is the unit normal to the surface. The PO current only exists where the incident field directly illuminates a surface (lit region). Once the current is found, the radiated fields are calculated using the appropriate radiation

---

[3] Although well-known now-a-days as Snell's law, however, according to [74], Snell's law was first accurately described in a mathematical form by Ibn Sahl, of Baghdad, in the manuscript: On Burning Mirrors and Lenses (984).

integral [70]. For edged bodies, the PO based radiation integral provides a PO approximation to the edge-diffracted fields if the edges fall within the illuminated region. However, the discontinuity in the current at the boundary between the illuminated and shadow region can introduce a spurious diffraction contribution to the PO integral. Hence, PO approximation may be erroneous for edge diffractions [70, 75].

GO and PO work reasonably well for large objects and at angles near the specular direction. However, both GO and PO are unable to describe nonzero fields in the shadow region. Diffracted rays are postulated to arise from geometrical and/or electrical discontinuities on the scattering obstacle [70]. For example diffracted rays can arise when an incident wave impinges on an edge, corner, or tip of scatterers. It also occurs as a creeping ray around a smooth object when the incident field is at grazing incidence. Discontinuities in surface electrical properties (e.g., discontinuity in surface impedance that models thin material coatings on PEC surfaces) and shadow boundaries on a smooth surface also produce diffracted rays. The geometrical theory of diffraction (GTD) [76] adds a diffracted field to the GO approximation. The GTD based dyadic edge diffraction coefficient becomes singular at the incident shadow boundary (ISB) and the reflection shadow boundary (RSB) [70] which makes GTD invalid at and near these boundaries. This deficiency in GTD can be overcome via the uniform theory of diffraction (UTD) [70, 77]. The physical theory of diffraction (PTD) [70, 78] adds correction term in PO to include the diffraction effects. GTD/UTD are ray-based method while the PTD requires an integration of the currents on the scattering object.

While high-frequency methods are well suited for modeling the scattering properties of electrically large complex shapes, such methods have difficulty in treating non-metallic material composition and volumetric complexity of a structure [79].

2.2.2 Finite-Difference Time-Domain Method

The direct time-domain solutions of Maxwell's equations on spatial grids may be obtained by replacing the partial derivatives with finite difference formulas. The finite-difference time-domain [80] directly solves the governing differential equations where it replaces the partial derivatives with respect to space and time with second-order finite difference approximation of the form [71]

$$\frac{d\,\phi}{d\,x_i} \approx \frac{\phi(x_{i+1}) - \phi(x_{i-1})}{2h}\,, \tag{2.13}$$

where x_i represent the grid coordinate and h is the grid spacing. Unlike the integral equation formulations, FDTD method doesn't need Green's functions. FDTD solves for both $\boldsymbol{E}$ and $\boldsymbol{H}$ using the coupled Maxwell's (curl) equations rather than solving for individual fields alone using a wave equation. This makes the solution more robust. The basic FDTD makes use of rectangular grid for the approximation of fields $\boldsymbol{E}$ and $\boldsymbol{H}$. The FDTD method is also often an explicit approach, that is, no matrix equation is set up and solved. The sampling in spatial grid is typically 10–20 samples per wavelength. The time steps must be less than a certain time which ensures numerical stability of the algorithm and can also capture the transient behavior of the system and is governed by the well-known *Courant condition* [79,81,82]

$$\Delta t \leq \frac{\Delta x}{c\sqrt{n}}, \tag{2.14}$$

where Δx is spatial resolution, Δt is temporal resolution, c is velocity of wave propagation in the medium, and n represents the space dimension.

FDTD does not include the radiation condition [65]. For closed regions (e.g. waveguide devices or cavities) this is of no concern. However, in applications where the solution domain extends to infinity, such as radiation or scattering problems, absorbing boundary conditions (ABC) , the numerical analogy of an anechoic chamber, are employed at the outer truncation planes which ideally permit all outgoing waves to exit the region with negligible reflection. The perfectly matched layer (PML) [53,83] is very common in FDTD, which absorbs the electromagnetic waves from any angle of incidence and of any frequency.

Due to time domain of FDTD, computation of wideband response of a system can be computed efficiently through the use of wideband sources. However, in reality many RF devices are quite narrow band or high-Q devices, which require number of time steps to obtain sufficient frequency resolution. Systems exhibiting dispersive (frequency dependent) characteristics, for instance, waveguides etc., pose a challenge to FDTD solutions because of convolution [65]. Basic implementation of FDTD is simple and straightforward for inhomogeneities. However, it is noteworthy that as the relative permittivites at RF and microwave frequencies rarely exhibit significant variation, and the dielectric properties of material usually play significant role, the material treatments in FDTD for typical RF applications is direct. Whereas, low frequency magnetostatic problems are mostly influenced by relative permeabilities which may exhibit large variations, resulting in complications for accurate modeling [65]. Furthermore, the FDTD formulation poses significant complications for non-orthogonal grids. As with FEM, the FDTD solutions become inefficient compared to MoM for highly conducting scatterers/radiators.

Some of the commercially available tools for FDTD based solution of electromagnetic problems include CST Microwave Studio[4], REMCOM's XFDTD, SEMCAD X.

2.2.3 Finite Element Method

In the finite element methods, the Maxwell's equations are solved in direct manner by using either the variational analysis or the weighted residuals. Both formulations start with the partial differential equation (PDE) form of the Maxwell'equations and for most applications, result in identical equations. Like FDTD, FEM doesn't require a Green's function.

The first step is to find a *functional* whose minimum corresponds to a solution of the wave equation. The functionals for electric field for the variational analysis and weighted residual method may be represented respectively as [25, 71]

$$\begin{aligned} F_v(\boldsymbol{E}) &= \frac{1}{2} \iiint_V \left[\frac{1}{\mu_r} (\nabla \times \boldsymbol{E}) \cdot (\nabla \times \boldsymbol{E}) - k_0^2 \epsilon_r \boldsymbol{E} \cdot \boldsymbol{E} \right] dv \\ &+ \frac{1}{2} \iint_S [\boldsymbol{E} \cdot (\hat{n} \times \nabla \times \boldsymbol{E})]\, da + \iiint_V \boldsymbol{E} \cdot \left[jk_0 Z_0 \boldsymbol{J}_s + \nabla \times \frac{\boldsymbol{M}_s}{\mu_r} \right] dv\,, \end{aligned} \tag{2.15}$$

and

$$\begin{aligned} F_w(\boldsymbol{E}) &= \frac{1}{2} \iiint_V \left[\frac{1}{\mu_r} (\nabla \times \boldsymbol{E}) \cdot (\nabla \times \boldsymbol{W}) - k_0^2 \epsilon_r \boldsymbol{E} \cdot \boldsymbol{W} \right] dv \\ &+ \frac{1}{2} \iint_S [\boldsymbol{W} \cdot (\hat{n} \times \nabla \times \boldsymbol{E})]\, da + \iiint_V \boldsymbol{W} \cdot \left[jk_0 Z_0 \boldsymbol{J}_s + \nabla \times \frac{\boldsymbol{M}_s}{\mu_r} \right] dv\,, \end{aligned} \tag{2.16}$$

where V is the volume containing the sources, S represents the boundary surface of the volume, $\boldsymbol{J}_s$ and $\boldsymbol{M}_s$ are equivalent current sources, and $\boldsymbol{W}$ is a weighting function. The functional for weighted residuals (2.16) is known as *weak form* because the governing equations are fulfilled in integral sense but not in a point by point manner.

The core idea of FEM is to replace some unknown function on a domain by a set of elements, with known shape but unknown amplitude. Courant in 1943 [25,65,84] for the first time found approximate solutions to the variational

---

[4] CST in fact uses Finite Integration Technique (FIT) solver, which is basically FDTD with integration instead of differentiation.

problems by using piecewise linear approximations on triangular elements. Unlike FDTD, the FEM permits very general geometrical elements. The most widely used elements are lines in 1D, triangles/rectangles in 2D, and tetrahedral/bricks in 3D. This results in a system of linear equations which can be solved to obtain the unknown quantity localized at each discrete element.

As with FDTD, FEM does not include the radiation condition [65]. Therefore for open solution domains, a mathematical boundary condition or a fictitious absorbing material layer or a surface integral equation must be incorporated. Examples include absorbing boundary condition [55], perfectly matched layer [53, 83], and hybridization of FEM with surface integral equation formulations [55, 85, 86].

Traditionally, the FEM has been formulated in the frequency domain, although time domain formulations have also been used for specialized applications. FEM produces *sparse* matrix and is attractive for modeling complex geometries, material inhomogeneities, as well as dispersive materials (i.e. having frequency dependent properties e.g. waveguides, real dielectric and magnetic materials). However, FEM becomes inefficient for highly conducting radiators/scatterers. That is why FEM is a preferable tool for microwave device simulations and eigenvalue problem analysis.

Ansoft's HFSS, ANSYS' Multiphysics software and COMSOL's FEMLAB are a few to mention the commercial software for FEM based solutions of scattering and radiation problems of electromagnetics.

2.2.4 Method of Moments Solution of Integral Equation Formulations

The integral equation formulations are based on integral operators which relate the unknown equivalent currents to the scattered fields. Radiating or scattering objects composed of conducting or homogeneous dielectric materials may be replaced by Huygens' equivalent surface currents radiating in free space, whereas for inhomogeneous dielectric bodies volumetric currents can be used. However, solution of volumetric formulations is computationally very expensive. An advantage of IE formulations is that they automatically incorporate the radiation condition and therefore contrary to the FEM and FDTD, IEs do not require absorbing boundary conditions. Discretization and solution of integral equation formulations by the method of moments was introduced to the electromagnetics community by Harrington [87, 88].

The Huygens' equivalent surface currents $\boldsymbol{J}_s$ and $\boldsymbol{M}_s$ are the tangential components of the magnetic and electric fields respectively determined on a close surface S surrounding the scatterer/radiator. These equivalent currents generate the scattered fields $\boldsymbol{E}^{sca}$ and $\boldsymbol{H}^{sca}$ outside of surface S_o and can be computed using radiation integrals [65, 89]

$$\boldsymbol{E}^{sca}(\boldsymbol{r}) = -\oint\!\!\!\oint_{S_o} \left[\boldsymbol{M}_s(\boldsymbol{r}') \cdot \nabla \times \bar{\boldsymbol{G}}(\boldsymbol{r}, \boldsymbol{r}') + jk_0 Z_0 \boldsymbol{J}_s(\boldsymbol{r}') \cdot \bar{\boldsymbol{G}}(\boldsymbol{r}, \boldsymbol{r}')\right] ds' \,, \tag{2.17}$$

$$\boldsymbol{H}^{sca}(\boldsymbol{r}) = \oint\!\!\!\oint_{S_o} \left[\boldsymbol{J}_s(\boldsymbol{r}') \cdot \nabla \times \bar{\boldsymbol{G}}(\boldsymbol{r}, \boldsymbol{r}') - j\frac{k_0}{Z_0} \boldsymbol{M}_s(\boldsymbol{r}') \cdot \bar{\boldsymbol{G}}(\boldsymbol{r}, \boldsymbol{r}')\right] ds' \,, \tag{2.18}$$

where

$$\bar{\boldsymbol{G}}(\boldsymbol{r}, \boldsymbol{r}') = \left(\bar{\boldsymbol{I}} + \frac{\nabla\nabla}{k_0^2}\right) \frac{e^{-jk_0|\boldsymbol{r}-\boldsymbol{r}'|}}{4\pi\,|\boldsymbol{r}-\boldsymbol{r}'|} \,, \tag{2.19}$$

is the free space dyadic Green's function. $\boldsymbol{r}$ represents a field point and $\boldsymbol{r}'$ denotes a source point. Z_0 is the free space intrinsic impedance and k_0 is the free space wave number. Combining the integral representations (2.17) and (2.18) with the boundary conditions [56]

$$\hat{n} \times \left(\boldsymbol{E}^{inc} + \boldsymbol{E}^{sca}\right) = 0 \,, \tag{2.20}$$

$$\hat{n} \times \left(\boldsymbol{H}^{inc} + \boldsymbol{H}^{sca}\right) = \boldsymbol{J}_s \,, \tag{2.21}$$

leads to integral equation formulations. Here $\hat{n}$ is a outward directed unit surface normal. Electric field integral equation (EFIE) is obtained if (2.20) is taken into consideration whereas (2.21) gives birth to a magnetic field integral equation (MFIE) .

However, if EFIE and MFIE are used independently for a closed surface S_o, both can support singular frequencies (nonphysical interior resonances) and therefore can corrupt the numerical solutions [25, 55]. The combined field integral equation (CFIE) formulation linearly combines both EFIE and MFIE formulations in order to reduce the spurious solutions. Also Shore [90, 91] advocates dual surface MFIE and EFIE to eliminate the resonant problems still associated with some formulations of the CFIE.

The surface integral equation formulations are capable of efficient treatment of conducting as well as homogeneous dielectric bodies because only boundary surface of the radiator/scattered need to be discretized. However, treatment of inhomogeneous penetrable materials require fictitious equivalent volumetric currents which make the formulation computationally very expensive compared to FEM or FDTD [65]. For the thin dielectric coatings, a so-called impedance boundary condition (IBC) may further be imposed on the surface integral equations to get efficient but approximate solutions for conducting bodies with thin dielectric coatings [25, 92, 93].

Numerical Electromagnetic Code (NEC-2, NEC-4, SuperNEC), FEKO, CST Microwave Studio, Ensemble, IE3D, GMACS are some of the public domain or commercially available tools which offer surface integral equation formulations for general-purpose modeling of radiation or scattering problems.

2.2.5 Hybrid Finite-Element Boundary-Integral Method

The most frequently encountered ABC and PML approaches for domain truncation in FEM suffer from a common disadvantage that they are approximate, i.e. they are not reflectionless for oblique incidence. A truly perfect boundary condition may be obtained if surface integral equation formulations are used to terminate the open region of FEM, however, at the cost of an increased computational burden because of fully populated matrix resulting from integral equation formulations [25, 55, 84–86].

The Finite-Element Boundary-Integral (FEBI) method employs an arbitrary boundary enclosing the object under consideration. Interior to this boundary FEM is applied whereas, surface integral equation formulations are used to represent the field in the region exterior to the boundary. Field continuity conditions are employed at the boundary to couple the fields in the interior and exterior regions [25, 55]. Hybridization of FEM and MoM solution of IEs results in so-called FEBI method and has proven very powerful in accurate and efficient solutions of complicated electromagnetic problems involving electromagnetically penetrable media together with highly conducting bodies.

It is worthwhile to mention, that a FEBI code copyright of Prof. Eibert [86] is very flexible and efficient tool to handle radiation and scattering problems of arbitrary nature.

2.2.6 Multilevel Fast Multipole Method

The matrix vector product involving the fully populated coupling matrix arising from the MoM solution of surface integral equations requires $O(N^2)$ operations for its direct computation, where N denotes the total number of unknowns. The operation count can be reduced to $O(N^{1.5})$ if the matrix vector product is computed using the fast multipole method introduced by Rokhlin [94–96]. This computational complexity can further be reduced to $O(N \log N)$ by implementing multilevel fast multipole method [5–7, 97–99]. It is to be noted that the matrix-vector product may be equivalently represented as the mutual interaction between the basis and testing functions; i.e. the fields radiated by the basis functions and then received by the testing functions.

In order to carry out FMM based matrix-vector product in the MoM solution of IEs, the common approach is to subdivide the entire computational domain (usually the object under consideration) into boxes (also known as groups or cells or cubes) with moderate number of elements in each box. The optimum number of elements in each box has been reported [63,65] to be equal to $\sqrt{N}$, or equivalently $\sqrt{N}$ FMM boxes, N being the total number of elements. In the MLFMM however, the entire domain is first enclosed in a large box, which is split up into eight small boxes. Each subbox is further recursively subdivided into smaller boxes until the side length of the lowest level box is around one-quarter wavelength[5]. For testing and basis function spatially residing in the same finest level box or in its direct neighborhood, their interaction is known as *near-interaction* and is computed in a direct manner through evaluating the double surface integral equations (see Chapter 3). FMM does not affect these contributions. However, when basis and testing vectors reside in different non-neighboring boxes their interaction is known as *far-interaction* and may be computed by FMM.

FMM based computation of matrix-vector product has foundations on the truncated form of series representation of free space Green's function obtained using Gegenbauer's addition theorem [96, 100] together with plane wave decomposition to achieve diagonalization [25,67,101,102], and may be expressed as

$$\frac{e^{-jk_0|\boldsymbol{r}-\boldsymbol{r}'|}}{4\pi|\boldsymbol{r}-\boldsymbol{r}'|} = \frac{e^{-jk_0|\boldsymbol{D}+\boldsymbol{d}|}}{4\pi|\boldsymbol{D}+\boldsymbol{d}|} \approx \frac{1}{4\pi} \oiint_S e^{-j\boldsymbol{k}\cdot\boldsymbol{d}} T_L(\hat{k}\cdot\hat{D}) d^2\hat{k}\,, \tag{2.22}$$

with

$$T_L(\hat{k}\cdot\hat{D}) = -\frac{jk_0}{4\pi}\sum_{l=0}^{L}(-j)^l(2l+1)h_l^{(2)}(k_0D)P_l(\hat{k}\cdot\hat{D})\,, \tag{2.23}$$

where $h_l^{(2)}(x)$ is a spherical Hankel function of the second kind, $P_l(x)$ is a Legendre polynomial. $\boldsymbol{D}$ and $\boldsymbol{d}$ are the spatial vectors (see Fig. (2.1)) such that $D > d$. Integral in (2.22) is evaluated over the unit sphere S in k-space (i.e. so-called Ewald sphere) and $\boldsymbol{k} = k_0\hat{k}$ is the wave propagation vector.

---

[5] Often a good choice is to use the finest level box dimension equal to twice the maximum length of an element.

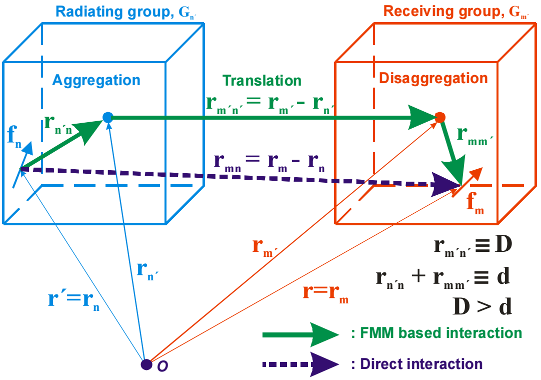

Fig. 2.1. Direct interaction path $\boldsymbol{r}_{mn}$ is split up into three FMM based interaction branches $\boldsymbol{r}_{n'n}$, $\boldsymbol{r}_{m'n'}$ and $\boldsymbol{r}_{mm'}$ respectively regarded as *aggregation*, *translation*, and *disaggregation*.

The truncated multipole expansion T_L is the diagonal matrix operator which translates the radiated plane waves from the center of the radiating group (synonymously known as source group) to the received plane waves at the center of the receiving group (or equivalently testing group). To achieve a relative error of the order of 10^{-d_a} in the solution, an empirical formula for the number of multipoles needed in (2.23) is given by [5]

$$L \approx kd + 1.8 d_a^{2/3} (kd)^{1/3} \, . \tag{2.24}$$

Additionally the required number of plane waves (i.e. integration points over the Ewald sphere) scales as $2(L+1)^2$ [36]. The efficient evaluation of the matrix-vector product with FMM is carried out in three major steps namely *aggregation*, *translation*, and *disaggregation* and may be visualized in Fig. (2.1).

The efficiency of the FMM algorithm is based on precomputing and storing the far-field pattern samples of the basis functions and the translation operator prior to the start of the actual matrix-vector product [11]. Additionally interpolation/anterpolation techniques must be incorporated for the efficient evaluation of the radiation/receiving patterns in $\hat{k}$-directions at higher/lower levels of the source/testing groups during aggregation/disaggregation processes respectively [67].

In chapter 3 MoM solution of surface integral equation formulation for the scattering and radiation problems of electromangetics will be discussed. As is known that the near-interactions involve the direct evaluation of the double surface integrals which become singular for neighboring source and testing domains, their accurate evaluation needs special treatment. Adaptive singularity cancellation treatment has been proposed and will therefore be presented in chapter 4. Choice of basis functions has significant role in the accurate and efficient solution of integral equation formulations. For this we have implemented hierarchical higher-order basis functions upto full first order in curl space of the basis functions and this will be discussed in chapter 5. Having developed the efficient and accurate formulation for the MoM solution of general purpose scattering and radiation problems, the aim of the present work is to synthesize arbitrary antenna structures for customized radiation patterns. For this purpose, inverse equivalent current method has been used for surface current synthesis from the knowledge of predefined customized radiation patterns. This is discussed in chapters 6 and 7.

3 Method of Moments Solution of Surface Integral Equation Formulations in Electromagnetics

Surface integral equation formulations have widespread applications in the solutions of field problems for arbitrarily shaped 3D objects. The domain of the governing integral equations is generally the boundary between the regions of the problem with unequal electromagnetic characteristic parameters. The unknown quantities, typically electric and/or magnetic surface equivalent current densities encountered in the IEs are discretized on the boundary surface and solution may be obtained through the numerical techniques such as MoM.

In the following, the calculation of fields using surface integral equation formulation will be reviewed.

3.1 Integral Equations in Electromagnetics

Consider a general 3D arbitrarily shaped scatterer. In order to have a complete system for the solution of fields, it is first necessary to enclose the scatterer within a fictitious surface to separate the interior region from the exterior region where the boundary integral equation may be applied. In most cases, the boundary surface of the object under consideration may be chosen for such a purpose, but for some scatterers other choices may be more efficient. A general rule is to choose a fictitious surface that has the least surface area. The fields inside the surface may then be formulated using FE method, whereas those exterior to the surface may be expressed in terms of surface integrals.

For a general problem of electromagnetic fields $\boldsymbol{E}$ and $\boldsymbol{H}$ produced by an electric current source density $\boldsymbol{J}$ in the presence of an arbitrarily shaped object in free space, the governing equations for $\boldsymbol{E}$ and $\boldsymbol{H}$ are

$$\nabla \times \nabla \times \boldsymbol{E} - k_0^2 \boldsymbol{E} = -j\omega\mu_0 \boldsymbol{J} \,, \tag{3.1}$$

$$\nabla \times \nabla \times \boldsymbol{H} - k_0^2 \boldsymbol{H} = \nabla \times \boldsymbol{J} \,, \tag{3.2}$$

or equivalently

$$\nabla^2 \boldsymbol{E} + k_0^2 \boldsymbol{E} = j\omega\mu_0 \boldsymbol{J} + \frac{j}{\epsilon\omega} \nabla \left(\nabla \cdot \boldsymbol{J} \right) \,, \tag{3.3}$$

$$\nabla^2 \boldsymbol{H} + k_0^2 \boldsymbol{H} = -\nabla \times \boldsymbol{J} . \tag{3.4}$$

The three dimensional Green's function $G_0(\boldsymbol{r}, \boldsymbol{r}')$ can be introduced for the solution of this problem. Here $G_0(\boldsymbol{r}, \boldsymbol{r}')$ satisfies the Helmholtz equation

$$\nabla^2 G_0\left(\boldsymbol{r}, \boldsymbol{r}'\right) + k_0^2 G_0\left(\boldsymbol{r}, \boldsymbol{r}'\right) = -\delta\left(\boldsymbol{r} - \boldsymbol{r}'\right) , \tag{3.5}$$

and the usual radiation condition. Solution of (3.5) under the radiation condition results in free space scalar Green's function

$$G_0\left(\boldsymbol{r}, \boldsymbol{r}'\right) = \frac{e^{-jk|\boldsymbol{r}-\boldsymbol{r}'|}}{4\pi\left|\boldsymbol{r}-\boldsymbol{r}'\right|} . \tag{3.6}$$

Next the scalar-vector Green's theorem is considered for the development of surface integral equation. Let b and $\boldsymbol{a}$ represent respectively scalar and vector functions integrable in an arbitrary volume V and on its boundary surface S. The scalar-vector Green's theorem is given by [103]

$$\begin{aligned}&\iiint\limits_V \left[b\left(\nabla \times \nabla \times \boldsymbol{a}\right) + \boldsymbol{a}\nabla^2 b + \left(\nabla \cdot \boldsymbol{a}\right)\nabla b \right] dv \\ &\quad = \oiint\limits_S \left[\left(\hat{n} \cdot \boldsymbol{a}\right)\left(\nabla b\right) + \left(\hat{n} \times \boldsymbol{a}\right) \times \nabla b + \left(\hat{n} \times \nabla \times \boldsymbol{a}\right) b \right] ds .\end{aligned} \tag{3.7}$$

Now letting $\boldsymbol{a} = \boldsymbol{E}$ and $b = G_0(\boldsymbol{r}, \boldsymbol{r}') = G_0$, we get

$$\begin{aligned}&\iiint\limits_V \left[G_0\left(\nabla \times \nabla \times \boldsymbol{E}\right) + \boldsymbol{E}\nabla^2 G_0 + \left(\nabla \cdot \boldsymbol{E}\right)\nabla G_0 \right] dv \\ &\quad = \oiint\limits_S \left[\left(\hat{n} \cdot \boldsymbol{E}\right)\left(\nabla G_0\right) + \left(\hat{n} \times \boldsymbol{E}\right) \times \nabla G_0 + \left(\hat{n} \times \nabla \times \boldsymbol{E}\right) G_0 \right] ds .\end{aligned} \tag{3.8}$$

Substituting equations (3.1) and (3.5) on the LHS of (3.8) we get

$$\begin{aligned}&\iiint\limits_V \left[G_0\left(k_0^2 \boldsymbol{E} - j\omega\mu_0 \boldsymbol{J}\right) + \boldsymbol{E}\left(-k_0^2 G_0 - \delta\left(\boldsymbol{r} - \boldsymbol{r}'\right)\right) + \left(\nabla \cdot \boldsymbol{E}\right)\nabla G_0 \right] dv \\ &\quad = \oiint\limits_S \left[\left(\hat{n} \cdot \boldsymbol{E}\right)\left(\nabla G_0\right) + \left(\hat{n} \times \boldsymbol{E}\right) \times \nabla G_0 + \left(\hat{n} \times \nabla \times \boldsymbol{E}\right) G_0 \right] ds ,\end{aligned}$$

or

$$\begin{aligned}&\iiint\limits_V \left[G_0\left(-j\omega\mu_0\boldsymbol{J}\right)+\boldsymbol{E}\left(-\delta\left(\boldsymbol{r}-\boldsymbol{r}'\right)\right)+\left(\nabla\cdot\boldsymbol{E}\right)\nabla G_0\right]dv\\&\qquad=\oiint\limits_S\left[\left(\hat{n}\cdot\boldsymbol{E}\right)\left(\nabla G_0\right)+\left(\hat{n}\times\boldsymbol{E}\right)\times\nabla G_0+\left(\hat{n}\times\nabla\times\boldsymbol{E}\right)G_0\right]ds\,.\end{aligned}\tag{3.9}$$

Also substituting

$$\nabla\cdot\boldsymbol{E}=\frac{\rho}{\epsilon_0}=\frac{-1}{j\epsilon_0\omega}\nabla\cdot\boldsymbol{J}=\frac{j}{\epsilon_0\omega}\nabla\cdot\boldsymbol{J}\,,$$

and

$$\nabla\times\boldsymbol{E}=-j\omega\boldsymbol{B}=-j\omega\mu_0\boldsymbol{H},$$

(where time convention $e^{j\omega t}$ is utilized) in (3.9) we have

$$\begin{aligned}&\iiint\limits_V\left[\left(-j\omega\mu_0\boldsymbol{J}G_0+\frac{j}{\epsilon_0\omega}\left(\nabla\cdot\boldsymbol{J}\right)\nabla G_0\right)-\boldsymbol{E}\delta\left(\boldsymbol{r}-\boldsymbol{r}'\right)\right]dv\\&\qquad=\oiint\limits_S\left[\left(\hat{n}\cdot\boldsymbol{E}\right)\nabla G_0+\left(\hat{n}\times\boldsymbol{E}\right)\times\nabla G_0-j\omega\mu_0\left(\hat{n}\times\boldsymbol{H}\right)G_0\right]ds\,.\end{aligned}\tag{3.10}$$

Interchanging prime and unprimed coordinates, i.e.

$$\begin{aligned}&\boldsymbol{J}\left(\boldsymbol{r}\right)\to\boldsymbol{J}\left(\boldsymbol{r}'\right)\ ,\ G_0\left(\boldsymbol{r},\boldsymbol{r}'\right)\to G_0\left(\boldsymbol{r},\boldsymbol{r}'\right)\ ,\ \hat{n}\to\hat{n}'\,,\\&\boldsymbol{E}\left(\boldsymbol{r}\right)\to\boldsymbol{E}\left(\boldsymbol{r}'\right)\ ,\ \boldsymbol{H}\left(\boldsymbol{r}\right)\to\boldsymbol{H}\left(\boldsymbol{r}'\right)\ ,\ \nabla\to\nabla'\ ,\ ds\to ds'\,,\end{aligned}$$

and using $\nabla' G_0=-\nabla G_0$ and $k_0^2=\omega^2\epsilon_0\mu_0$ in (3.10) we get

$$\begin{aligned}&\iiint\limits_V\left[-j\omega\mu_0\left(\boldsymbol{J}G_0+\frac{1}{k_0^2}\left(\nabla'\cdot\boldsymbol{J}\right)\nabla G_0\right)-\boldsymbol{E}\left(\boldsymbol{r}'\right)\ \delta\left(\boldsymbol{r}-\boldsymbol{r}'\right)\right]dv'\\&\qquad=-\oiint\limits_S\left[\left(\hat{n}'\cdot\boldsymbol{E}\left(\boldsymbol{r}'\right)\right)\nabla G_0+\left(\hat{n}'\times\boldsymbol{E}\left(\boldsymbol{r}'\right)\right)\times\nabla G_0\right.\\&\qquad\left.+\,j\omega\mu_0\left(\hat{n}'\times\boldsymbol{H}\left(\boldsymbol{r}'\right)\right)G_0\right]ds'\,.\end{aligned}\tag{3.11}$$

The evaluation of the volume integral of the last term on the left hand side of (3.11) may be split into two regions such that either $\boldsymbol{r}$ is inside of volume V (i.e. $\boldsymbol{r} \in V$) or outside (i.e. $\boldsymbol{r} \notin V$), and is given by [103]

$$\iiint\limits_{V} \boldsymbol{E}\left(\boldsymbol{r}'\right)\ \delta\left(\boldsymbol{r}-\boldsymbol{r}'\right) dv' = \begin{cases} \boldsymbol{E}\left(\boldsymbol{r}\right), & \boldsymbol{r} \in V\,, \\ 0, & \boldsymbol{r} \notin V\,. \end{cases} \tag{3.12}$$

It is worthwhile to mention that the radiated field $\boldsymbol{E}\left(\boldsymbol{r}\right)$ exists at a set of points $\boldsymbol{r} \in V$ and therefore the integral (3.12) vanishes when it is evaluated in the space outside of domain V.

Now (3.11) will be evaluated separately in the region occupied by the impressed sources and in the source-free region.

3.1.1 Fields over the Region Occupied by Impressed Sources

First we compute (3.11) over the region occupied by impressed sources i.e. volume V_J, and its boundary S_J as shown in Fig. 3.1. In this region the integration domain V_J does not contain $\boldsymbol{r}$ and hence, from (3.12)

$$\iiint\limits_{V_J} \boldsymbol{E}\left(\boldsymbol{r}'\right)\ \delta\left(\boldsymbol{r}-\boldsymbol{r}'\right) dv' = 0\,. \tag{3.13}$$

Further we define

$$-j\omega\mu_0 \iiint\limits_{V_J} \left[\boldsymbol{J}G_0 + \frac{1}{k_0^2}\left(\nabla'\cdot\boldsymbol{J}\right)\nabla G_0\right] dv' \equiv \boldsymbol{E}^{inc}\left(\boldsymbol{r}\right)\,, \tag{3.14}$$

which represents the electric field produced by $\boldsymbol{J}$ in free space without the presence of any scattering object.

Substituting (3.13) and (3.14) in (3.11) we get an integral representation for field quantities within the region occupied by the impressed sources, i.e.

$$\begin{aligned} \boldsymbol{E}^{inc}\left(\boldsymbol{r}\right) = -\oiint\limits_{S_J} \Big[&\left(\hat{n}'\cdot\boldsymbol{E}\left(\boldsymbol{r}'\right)\right)\nabla G_0 + \left(\hat{n}'\times\boldsymbol{E}\left(\boldsymbol{r}'\right)\right)\times\nabla G_0 \\ &+ j\omega\mu_0\left(\hat{n}'\times\boldsymbol{H}\left(\boldsymbol{r}'\right)\right)G_0\Big] ds'\,. \end{aligned} \tag{3.15}$$

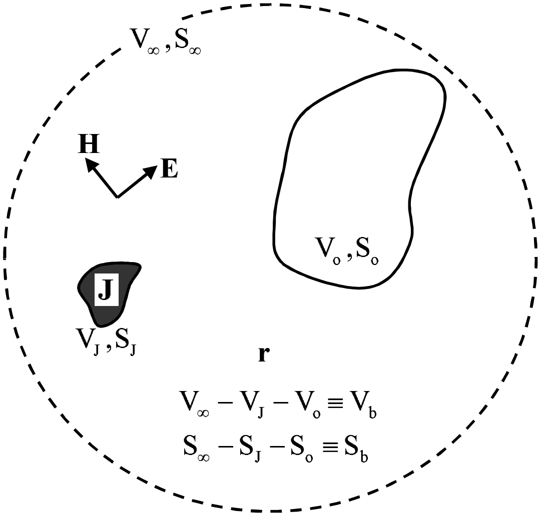

Fig. 3.1. Source and scattering volumes placed in free space.

3.1.2 Fields over the Exterior Region

Now the integral representation (3.11) is computed over the region exterior to all sources and any scattering bodies i.e. volume $V_\infty - V_J - V_o \equiv V_b$, and its boundary $S_\infty - S_J - S_o \equiv S_b$ as shown in Fig. 3.1. In this region $\boldsymbol{r}$ is contained in the integration domain V_b and therefore, from (3.12)

$$\iiint\limits_{V_b} \boldsymbol{E}\left(\boldsymbol{r}'\right)\ \delta\left(\boldsymbol{r}-\boldsymbol{r}'\right) dv' = \boldsymbol{E}\left(\boldsymbol{r}\right) ,$$

and since no impressed sources in this region, therefore

$$-j\omega\mu_0 \iiint\limits_{V_b} \left[\boldsymbol{J}G_0 + \frac{1}{k_0^2}\left(\nabla'\cdot\boldsymbol{J}\right)\nabla G_0\right] dv' = 0 .$$

Further, the integral evaluated over V_∞ vanishes if:

- the sources of the field are confined within a finite distance from the origin,

- field satisfies the Sommerfeld radiation condition, and
- Green's function G_0 is chosen to satisfy the radiation condition as well.

Thus, it can be shown [103] that

$$\begin{aligned}\oint\!\!\!\oint_{S_\infty} \Big[\left(\hat{n}' \cdot \boldsymbol{E}\left(\boldsymbol{r}'\right)\right) \nabla G_0 + \left(\hat{n}' \times \boldsymbol{E}\left(\boldsymbol{r}'\right)\right) \times \nabla G_0 \\ + j\omega\mu_0 \left(\hat{n}' \times \boldsymbol{H}\left(\boldsymbol{r}'\right)\right) G_0 \Big] ds' = 0\,. \end{aligned} \tag{3.16}$$

Hence, integral representation (3.11) becomes

$$\begin{aligned} -\boldsymbol{E}(\boldsymbol{r}) &= -\oint\!\!\!\oint_{S_b} \Big[\left(\hat{n}' \cdot \boldsymbol{E}\left(\boldsymbol{r}'\right)\right) \nabla G_0 + \left(\hat{n}' \times \boldsymbol{E}\left(\boldsymbol{r}'\right)\right) \times \nabla G_0 \\ &\qquad + j\omega\mu_0 \left(\hat{n}' \times \boldsymbol{H}\left(\boldsymbol{r}'\right)\right) G_0 \Big] ds' \\ \Rightarrow\ \boldsymbol{E}(\boldsymbol{r}) &= \oint\!\!\!\oint_{S_\infty} \Big[\dots \Big] ds' - \oint\!\!\!\oint_{S_J} \Big[\dots \Big] ds' - \oint\!\!\!\oint_{S_o} \Big[\dots \Big] ds'\,. \end{aligned} \tag{3.17}$$

Using (3.15) and (3.16) in (3.17) we get

$$\begin{aligned} \boldsymbol{E}^{inc}(\boldsymbol{r}) - \oint\!\!\!\oint_{S_o} \Big[\left(\hat{n}' \cdot \boldsymbol{E}\left(\boldsymbol{r}'\right)\right) \nabla G_0 + \left(\hat{n}' \times \boldsymbol{E}\left(\boldsymbol{r}'\right)\right) \times \nabla G_0 \\ + j\omega\mu_0 \left(\hat{n}' \times \boldsymbol{H}\left(\boldsymbol{r}'\right)\right) G_0 \Big] ds' = \boldsymbol{E}(\boldsymbol{r})\ . \end{aligned} \tag{3.18}$$

Integral equation (3.18) is valid for $\boldsymbol{r} \in V_b$. However, as can be seen from (3.12), the field $\boldsymbol{E}(\boldsymbol{r})$ will vanish for $\boldsymbol{r} \in V_o$ and hence we get

$$\begin{aligned} \boldsymbol{E}^{inc}(\boldsymbol{r}) - \oint\!\!\!\oint_{S_o} \Big[\left(\hat{n}' \cdot \boldsymbol{E}\left(\boldsymbol{r}'\right)\right) \nabla G_0 + \left(\hat{n}' \times \boldsymbol{E}\left(\boldsymbol{r}'\right)\right) \times \nabla G_0 \\ + j\omega\mu_0 \left(\hat{n}' \times \boldsymbol{H}\left(\boldsymbol{r}'\right)\right) G_0 \Big] ds' = \begin{cases} \boldsymbol{E}(\boldsymbol{r})\,, & \boldsymbol{r} \in V_b\,, \\ 0, & \boldsymbol{r} \in V_o\,, \end{cases} \end{aligned} \tag{3.19}$$

where V_b represents the region exterior to the source and scattering bodies and is often referred to as solution domain. Equation (3.19) represents a form of integral representation for electric field.

Similarly, if we substitute $\boldsymbol{a} = \boldsymbol{H}$ and $b = G_0(\boldsymbol{r}, \boldsymbol{r}') = G_0$ in (3.7) we get an integral representation for magnetic field

$$\begin{aligned}\boldsymbol{H}^{inc}(\boldsymbol{r}) - \oiint_{S_o} \Big[\left(\hat{n}' \cdot \boldsymbol{H}\left(\boldsymbol{r}'\right)\right) \nabla G_0 + \left(\hat{n}' \times \boldsymbol{H}\left(\boldsymbol{r}'\right)\right) \times \nabla G_0 \\ - j\omega\epsilon_0 \left(\hat{n}' \times \boldsymbol{E}\left(\boldsymbol{r}'\right)\right) G_0 \Big] ds' = \begin{cases} \boldsymbol{H}(\boldsymbol{r}), & \boldsymbol{r} \in V_b\,. \\ 0, & \boldsymbol{r} \in V_o\,. \end{cases}\end{aligned} \tag{3.20}$$

Here $\boldsymbol{E}^{inc}(\boldsymbol{r})$ and $\boldsymbol{H}^{inc}(\boldsymbol{r})$ represent respectively the electric and magnetic fields produced by the impressed current sources $\boldsymbol{J}$ in free space without any scattering object. In the region interior to the scattering bodies, above equations are also valid because the fields vanish.

Introduction of Huygens' equivalent surface currents on the surface S_o of the scatterer yields

$$\boldsymbol{J}_s = \hat{n} \times \boldsymbol{H} \qquad \text{and} \qquad \boldsymbol{M}_s = -\hat{n} \times \boldsymbol{E} \qquad \text{defined over } S_o\,. \tag{3.21}$$

From rearrangements of the Ampère law and the Faraday's law applied on the boundary S_o with no impressed sources present (or alternatively, using the normal boundary conditions), we can get [25, 104]

$$\hat{n} \cdot \boldsymbol{E} = \frac{\rho_s}{\epsilon_0} = \frac{j}{\omega\epsilon_0} \nabla \cdot \boldsymbol{J_s}\,, \tag{3.22}$$

and

$$\hat{n} \cdot \boldsymbol{H} = \frac{\rho_s^m}{\epsilon_0} = \frac{j}{\omega\mu_0} \nabla \cdot \boldsymbol{M_s}\,, \tag{3.23}$$

where ρ_s represents surface electric charge density and ρ_s^m is (fictitious) surface magnetic charge density. Using equations (3.21) - (3.23) in (3.19) and (3.20) we get

$$\begin{aligned}\boldsymbol{E}(\boldsymbol{r}) + jk_0 Z_0 \left[\frac{1}{k_0^2} \nabla \oiint_{S_o} G_0\, \nabla' \cdot \boldsymbol{J}_s\, ds' + \oiint_{S_o} \boldsymbol{J}_s G_0\, ds' \right] \\ + \oiint_{S_o} \nabla G_0 \times \boldsymbol{M}_s\, ds' = \boldsymbol{E}^{inc}(\boldsymbol{r})\ ,\end{aligned} \tag{3.24}$$

and

$$\begin{aligned} &\boldsymbol{H}(\boldsymbol{r}) + \frac{jk_0}{Z_0}\left[\frac{1}{k_0^2}\nabla \oiint_{S_o} G_0\,\nabla'\cdot\boldsymbol{M}_s\,ds' + \oiint_{S_o} \boldsymbol{M}_s G_0\,ds'\right] \\ &\qquad - \oiint_{S_o} \nabla G_0 \times \boldsymbol{J}_s\,ds' = \boldsymbol{H}^{inc}(\boldsymbol{r})\ , \end{aligned} \tag{3.25}$$

where $k_0 = \omega\sqrt{\epsilon_0\mu_0}$ and $Z_0 = \sqrt{\mu_0/\epsilon_0}$ are respectively wavenumber and intrinsic impedance of free space. $\boldsymbol{E}^{inc}(\boldsymbol{r})$ and $\boldsymbol{H}^{inc}(\boldsymbol{r})$ represent the fields produced by electric and magnetic current sources $\boldsymbol{J}$ and $\boldsymbol{M}$ without the presence of scatterer. Equations (3.24) and (3.25) define the fields $\boldsymbol{E}(\boldsymbol{r})$ and $\boldsymbol{H}(\boldsymbol{r})$ produced by the current sources in the presence of the scatterers and hold throughout the exterior region and provide the foundation to derive the integral representations for current sources $\boldsymbol{J}_s$ and $\boldsymbol{M}_s$.

3.1.3 Electric Field Integral Equation

Computing (3.24) for its tangential component on the boundary surface S_o and extracting the contribution of singular point $\boldsymbol{r} = \boldsymbol{r}'$ from the surface integrals, we get [25, 104]

$$\boxed{\begin{aligned} &-\frac{1}{2}\boldsymbol{M}_s(\boldsymbol{r}) + jk_0 Z_0\,\hat{n}\times\left[\frac{1}{k_0^2}\nabla \oiint_{S_o} G_0\,\nabla'\cdot\boldsymbol{J}_s\,ds' + \oiint_{S_o} \boldsymbol{J}_s G_0\,ds'\right] \\ &\qquad + \hat{n}\times \oiint_{S_o} \nabla G_0 \times \boldsymbol{M}_s\,ds' = \hat{n}\times\boldsymbol{E}^{inc}(\boldsymbol{r})\ , \end{aligned}} \tag{3.26}$$

where singular contribution has been extracted from all integrals. Equation (3.26) is known as electric field integral equation and can be used for both open and closed bodies. However, this equation provides erroneous solution at resonant frequencies of the cavity formed by covering the surface S_o with PEC and filling the interior with the exterior medium. This problem is known as interior resonance. One way to get rid of this problem is to use finite element formulation in conjunction with the complexification of the wavenumber. Another approach is to combine different integral equations to eliminate the interior resonance completely [25]. The CFIE discussed below is free from this drawback.

3.1.4 Magnetic Field Integral Equation

Computing (3.25) for its tangential part on the boundary surface S_o and extracting the singular point contribution yields another integral equation

$$\boxed{\begin{aligned}\frac{1}{2}\boldsymbol{J}_s\left(\boldsymbol{r}\right) + \frac{jk_0}{Z_0}\,\hat{n}\times\left[\frac{1}{k_0^2}\nabla\oiint\limits_{S_o} G_0\,\nabla'\cdot\boldsymbol{M}_s\,ds' + \oiint\limits_{S_o}\boldsymbol{M}_s G_0\,ds'\right]\\ -\,\hat{n}\times\oiint\limits_{S_o}\nabla G_0\times\boldsymbol{J}_s\,ds' = \hat{n}\times\boldsymbol{H}^{inc}\left(\boldsymbol{r}\right)\,,\end{aligned}} \tag{3.27}$$

which is known as magnetic field integral equation. It converges fastly but can only be used for closed bodies. Unfortunately, this equation also suffers from the problem of interior resonance.

3.1.5 Combined Field Integral Equation

EFIE can be used for both open and closed bodies, however, it suffers from the interior resonance problem. Additionally, the iterative solver converges slowly in the MoM solution of EFIE. The iterative solver for MFIE converges fastly but it can only be used for closed bodies and also suffers from the problem of interior resonance. A linear combination of EFIE and MFIE, known as CFIE, is free from interior resonance problem and converges fastly. However it is useful only for closed bodies. The CFIE is written as follows [105, 106]:

$$\alpha\,\text{EFIE} + (1-\alpha)\,Z_0\,\hat{n}\times\,\text{MFIE}\,, \tag{3.28}$$

where $\alpha \in [0, 1]$ is the CFIE combination coefficient. The combination (3.28) results in an integral equation corresponding to that for a cavity with a resistive wall whose resonant frequencies are complex and hence no singular real frequencies in CFIE. Also, CFIE provides fast iterative solver convergence.

3.2 Impedance Boundary Condition

When the problem under consideration involves only the PEC objects, the magnetic current densities $\boldsymbol{M}_s$ in the above IEs (3.26)-(3.28) vanish and only the electric current densities $\boldsymbol{J}_s$ remain as the unknown quantities. However, in general, when scattered or radiated fields from a surface impedance body are required, both electric and magnetic current densities are unknown quantities. The under-determined system of equations, with unknown $\boldsymbol{J}_s$ and $\boldsymbol{M}_s$, reduces to a determined system with the enforcement of an appropriate boundary condition.

The simplest and most widely used approximate boundary condition, e.g. for modeling the dielectrically coated conducting objects, is the impedance boundary condition introduced by Leontovich [107] and defined on the boundary between the exterior of the coating and free space and may be expressed as [25]

$$\boldsymbol{M}_s = Z_S \left(\boldsymbol{J}_s \times \hat{n}\right) , \tag{3.29}$$

where Z_S is termed as the characteristic surface impedance. For PEC bodies with thin dielectric coatings, Z_S may be approximated as

$$Z_S = jZ_0 \sqrt{\frac{\mu_r}{\epsilon_r}} \tan\left(k_0 d \sqrt{\epsilon_r \mu_r}\right) , \tag{3.30}$$

d being the thickness of the coating and ϵ_r and μ_r are respectively the relative permittivity and relative permeability of the dielectric coating.

3.3 Solution by Method of Moments

Method of moments is a general procedure for the solution of any differential or integral equation. The basic principle of method of moments is to convert the governing equations for a boundary value problem, through numerical approximations, into a matrix equation that can be solved by numerical techniques. The basic steps of MoM solution of an electromagnetic boundary value problem (BVP) are as follow:

1. Formulation of the problem into an integral (or differential) equation.
2. Expansion of the unknown quantity using a set of basis functions e.g RWG basis functions.
3. Inner product of the discretized integral equation with another set of testing functions. This will result in a matrix equation.
4. Solution of matrix equation with appropriate numerical method and calculate the desired quantities.

While solving either of the integral equations (3.26)-(3.28) by the MoM, the unknown surface current densities $\boldsymbol{J}_s$ and $\boldsymbol{M}_s$ are expanded using a set of basis functions

$$\boldsymbol{J}_s = \sum_{n=1}^{N_I} I_n \boldsymbol{f}_n , \qquad \boldsymbol{M}_s = \sum_{n=1}^{N_M} V_n \boldsymbol{f}_n , \tag{3.31}$$

where I_n and V_n are the unknown expansion coefficients. $N = N_I + N_M$ is the total number of unknowns. $\boldsymbol{f}_n$ represent a set of vector basis functions. As an example, the most popular LO triangular current basis functions similar to those introduced in [34] are $\boldsymbol{f}_n(\boldsymbol{r}') = \frac{\boldsymbol{r}'-\boldsymbol{r}_c}{2A}$, where A is the area of the triangle and $\boldsymbol{r}_c$ are its three vertices. The degree of the polynomials defining $\boldsymbol{f}_n$ is a representative for the order of the basis functions.

Let $\boldsymbol{g}_m$ be a testing function. Different choices of testing functions in MoM solution of integral equations are found. First kind of testing is known as *point collocation* or *point matching* and is expressed as

$$\boldsymbol{g}_m(\boldsymbol{r}) = \delta(\boldsymbol{r} - \boldsymbol{r}_m) \,,$$

where $\boldsymbol{r}_m$ denotes a set of points in the solution domain.
Second kind of testing is known as *subdomain collocation*

$$\boldsymbol{g}_m(\boldsymbol{r}) = \begin{cases} 1\,, & \boldsymbol{r} \in \Omega_m\,, \\ 0\,, & \text{elsewhere}\,, \end{cases}$$

where Ω_m denotes the mth subdomain.

A third kind of testing is to use the basis functions as the testing functions and is known as *Galerkin's formulation* i.e.

$$\boldsymbol{g}_m(\boldsymbol{r}) = \boldsymbol{f}_m(\boldsymbol{r}) \,.$$

In *Galerkin's formulation* the system matrix becomes symmetric when the integral operator is symmetric. These testing functions are widely used in the MoM solutions of IEs.

Recent researches also indicate that solution accuracy depends primarily on the choice of basis functions and much less on the choice of testing functions [66]. In [108] it has been investigated that if RWG functions are taken as both basis and test functions for the solution of CFIE, it leads to a very unstable solution. Only electric surface current is well tested in this case. Similarly, if $\hat{n} \times$ RWG functions are used as testing functions, only the magnetic current is well tested and the solution is again inaccurate. The authors of [108] suggest to test CFIE by both RWG and $\hat{n} \times$ RWG functions.

Applying Galerkin's method for testing (3.26)-(3.28) and (3.29), we can get the respective systems of linear equations

$$\begin{aligned}\text{EFIE:}\quad &\sum_{n=1}^{N_M}\left[\frac{1}{2}A_{mn}+D_{mn}\right]V_n\\ &+jZ_0k_0\sum_{n=1}^{N_I}\left[B_{mn}+\frac{C_{mn}}{k_0^2}\right]I_n=G_m^E\,,\ m=1,...,N_I\,,\end{aligned}\tag{3.32}$$

$$\begin{aligned}\text{MFIE:}\quad &\sum_{n=1}^{N_I}\left[-\frac{1}{2}A'_{mn}-D'_{mn}\right]I_n\\ &+j\frac{k_0}{Z_0}\sum_{n=1}^{N_M}\left[B'_{mn}+\frac{C'_{mn}}{k_0^2}\right]V_n=G_m^H\,,\ m=1,...,N_I\,,\end{aligned}\tag{3.33}$$

$$\begin{aligned}\text{IBC:}\quad &\sum_{n=1}^{N_M}\left[A'_{mn}\right]V_n\\ &+Z_S\sum_{n=1}^{N_I}\left[A_{mn}\right]I_n=0\,,\ m=1,...,N_M.\end{aligned}\tag{3.34}$$

A similar system of linear equations for CFIE can be obtained by substituting (3.32) and (3.33) in (3.28). The matrix elements involved in (3.32), (3.33) and (3.34) are

$$A_{mn}=\iint\limits_{S_m}\boldsymbol{g}_m(\boldsymbol{r})\cdot\hat{n}\times\boldsymbol{f}_n(\boldsymbol{r})ds\,,\tag{3.35}$$

$$B_{mn}=\iint\limits_{S_m}\boldsymbol{g}_m(\boldsymbol{r})\cdot\iint\limits_{S_n}G_0(\boldsymbol{r},\boldsymbol{r}')\boldsymbol{f}_n(\boldsymbol{r}')ds'ds\,,\tag{3.36}$$

$$\begin{aligned}C_{mn}&=\iint\limits_{S_m}\boldsymbol{g}_m(\boldsymbol{r})\cdot\nabla\iint\limits_{S_n}G_0(\boldsymbol{r},\boldsymbol{r}')\nabla'_s\cdot\boldsymbol{f}_n(\boldsymbol{r}')ds'ds\,,&&(3.37)\\ &=C_{mn}^M-C_{mn}^E\,,&&(3.37')\end{aligned}$$

$$C_{mn}^E=\iint\limits_{S_m}\nabla_s\cdot\boldsymbol{g}_m(\boldsymbol{r})\iint\limits_{S_n}G_0(\boldsymbol{r},\boldsymbol{r}')\nabla'_s\cdot\boldsymbol{f}_n(\boldsymbol{r}')ds'ds\,,\tag{3.38}$$

$$C_{mn}^{M} = \oint\limits_{C_m} \boldsymbol{g}_m(\boldsymbol{r}) \cdot \hat{u}_m \iint\limits_{S_n} G_0(\boldsymbol{r},\boldsymbol{r}')\nabla_s' \cdot \boldsymbol{f}_n(\boldsymbol{r}')ds'dl\,, \tag{3.39}$$

$$D_{mn} = \iint\limits_{S_m} \boldsymbol{g}_m(\boldsymbol{r}) \cdot \iint\limits_{S_n} \nabla G_0(\boldsymbol{r},\boldsymbol{r}') \times \boldsymbol{f}_n(\boldsymbol{r}')ds'ds\,, \tag{3.40}$$

$$G_{m}^{E} = \iint\limits_{S_m} \boldsymbol{f}_m(\boldsymbol{r}) \cdot \boldsymbol{E}^{inc} ds\,, \text{ and} \tag{3.41}$$

$$G_{m}^{H} = \iint\limits_{S_m} \hat{n} \times \boldsymbol{f}_m(\boldsymbol{r}) \cdot \boldsymbol{H}^{inc} ds\,, \tag{3.42}$$

where $\boldsymbol{g}_m = \boldsymbol{f}_m(\boldsymbol{r})$ for the unprimed versions of the matrix elements (i.e. A_{mn}, ..., D_{mn}) and $\boldsymbol{g}_m = \hat{n} \times \boldsymbol{f}_m(\boldsymbol{r})$ for the primed matrix elements (i.e. A'_{mn}, ..., D'_{mn}) used in (3.32), (3.33) and (3.34). Equation (3.37) has been rewritten in (3.37′) through the use of Gauss's divergence theorem [34, 109] to transfer the del (∇) operator from G_0 to $\boldsymbol{g}_m$. Note, while testing with low-order RWG-functions, C_{mn}^{M} vanishes for EFIE, and C_{mn}^{E} vanishes for MFIE. However, generally speaking for HO basis functions, both terms (3.38) and (3.39) are required. S_m and S_n are respectively the test and source domains under consideration. C_m is the boundary curve of the test domain and $\hat{u}_m$ is the unit vector in the tangent plane and perpendicular to the C_m.

Integrals (3.35), (3.41), and (3.42) can easily be evaluated numerically. However, direct numerical quadrature is not applicable for the integrals (3.36), (3.37), and (3.40), especially for self-coupling and near-coupling terms, and special numerical treatment of such integrals is necessary. In such cases, various techniques are available in the literature and will be reviewed briefly in chapter 4. In our implementation, the adaptive singularity cancellation approach [22–24] has been used for the efficient computation of these integrals. The fully numerical evaluation of the singular integrals and applicability to arbitrary order of the basis functions are among the motives of this choice. Further, its adaption to the HO formulation is straightforward. Thus, adaptive *Arcsinh* transformation has been used to compute (3.36) and (3.37) while Radial Angular-R^2 transformation has been applied for the evaluation of (3.40).

4 Singularity Treatment in Near Couplings

The accuracy of method of moments solutions of integral equations depends significantly on the calculation of the coupling integrals which involve singular kernels. Direct numerical quadrature is not applicable, especially for neighboring source and test domains, and special numerical treatment of such integrals is necessary. In this chapter adaptive singularity cancellation technique is discussed in detail for the accurate and efficient evaluation of coupling integrals.

4.1 Treatment of Singular Integrals - A Review

In literature, various techniques are available for the computation of singular coupling integrals encountered in the MoM solutions of surface integral equations. The Duffy method [12], the singularity subtraction approach [13–17], regularization techniques [18, 19] and the singularity cancellation approaches [20–22] are among the popular techniques.

The considered singular integrals encountered in MoM solution of the surface integral equation formulations of radiation and scattering problems have the following general forms:

$$\boldsymbol{B} = \iint_{S_o} \boldsymbol{f}(\boldsymbol{r'}) \frac{e^{-jk_0 R}}{R} ds' , \tag{4.1}$$

$$\boldsymbol{D} = \iint_{S_o} \boldsymbol{f}(\boldsymbol{r'}) \times \nabla \frac{e^{-jk_0 R}}{R} ds' , \tag{4.2}$$

where $R = |\boldsymbol{r} - \boldsymbol{r'}|$, $\boldsymbol{f}$ is the vector basis function and S_o represents the source or integration domain. Integrals (4.1) and (4.2) possess $\frac{1}{R}-$ and $\frac{\boldsymbol{R}}{R^3}-$type singularities respectively.

Before we review these techniques it is to be noted that various conflicting nomenclature can be found in the literature with regard to the location of singular point as well as the order of singularity. However, we will restrict ourself to following definitions throughout the entire discussion.

1. An observation point will be referred to as *singular*, if it is located within the source domain (Fig. 4.1a).

2. If the observation point is located away from the source domain but resides on the same plane as that of the source domain, we refer it to as *near-singular* (Fig. 4.1b).
3. When observation point is above/below the source plane however, projection of observation point lies within the source domain, it is termed as *hyper-singular*[1] (Fig. 4.1c).
4. In case when the observation point is located out of the source plane and its projection also lies away from the source domain, it is referred to as *near hyper-singular* (Fig. 4.1d).

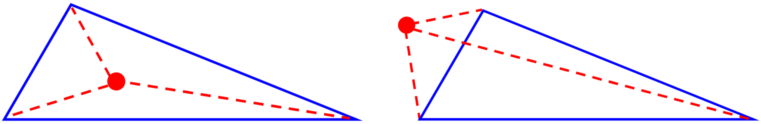

(a) Singular (b) Near-singular

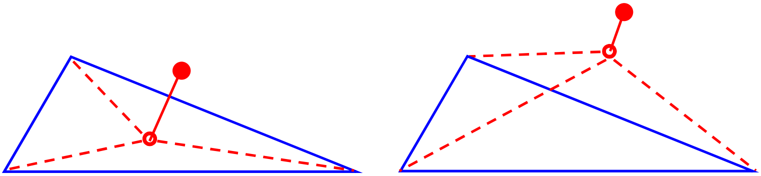

(c) Hyper-singular (d) Near hyper-singular

● : Observation point ○ : Projection of observation point on source plane

Fig. 4.1. Nomenclature for singularities w.r.t. relative position of the singular observation point

Further, in MoM solution of IEs, the $\frac{1}{R}-$type singular kernels have contributions usually for all above-mentioned four types of observation points, whereas $\frac{\boldsymbol{R}}{R^3}-$type hyper-singular[2] kernels don't contribute for singular and near-singular observation points.

4.1.1 Duffy Transformation Method

Duffy transformation [12] is based on decomposing the original source domain into triangles that share the singular point as a common vertex. A transforma-

---

[1] Some authors e.g. [19] call such type of singularity as near-singular.

[2] Usually hyper-singular means a singularity of higher order and it is also known as strongly singular kernel in physics and mechanical engineering literature.

tion that maps the triangle into a degenerate quadrilateral is performed such that the singularity of the integrand will be canceled by the Jacobian of the transformation. As an example the singular integral

$$\int_0^1 \int_0^{x'} \frac{f(x', y')}{\sqrt{(x')^2 + (y')^2}} dy' dx' \,, \tag{4.3}$$

which has triangular integration domain may be reduced to non-singular integral with rectangular integration domain

$$\int_0^1 \int_0^1 \frac{f(x', x'u)}{\sqrt{1 + u^2}} du dx', \tag{4.4}$$

by using the transformation $y' = x'u$. The Duffy transformation usually reduces the singularity by one order.

Some of the drawbacks of the Duffy method are [20]:

1. It produces an angular variation about the singular point in the resulting integrand.
2. It appears not to work well when applied to hyper-singularities.

4.1.2 Singularity Subtraction Approach

The key step in this approach is to extract from the desired singular integrand a term that has known closed form and can be evaluated analytically, such that a well-behaved non-singular remainder that can easily be evaluated numerically is left behind. As an example, the surface integral involving free space Green's function may be expressed as

$$\oiint_{S_o} \frac{e^{-jk_0|\boldsymbol{r}-\boldsymbol{r}'|}}{|\boldsymbol{r}-\boldsymbol{r}'|} ds' = \oiint_{S_o} \frac{e^{-jk_0|\boldsymbol{r}-\boldsymbol{r}'|} - 1}{|\boldsymbol{r}-\boldsymbol{r}'|} ds' + \oiint_{S_o} \frac{1}{|\boldsymbol{r}-\boldsymbol{r}'|} ds' \,, \tag{4.5}$$

where the first term on the right hand side is non-singular and may be computed numerically. Analytical expressions can be found (e.g. [15, 16]) for the evaluation of second term.

The singularity subtraction approach relies on the existence of analytically evaluated potential integrals. Many of these have been worked out for constant and linear source distributions [13–17] and even for higher order polynomial source variations as well as higher order geometries [110–112]. Polynomial basis functions of any order may be integrated over planar triangles using recurrence relationships [14], and extended for curved elements [112] by introducing tangent plane elements whose basis vectors at the contact point are same as those of the curved element.

Some of the disadvantages of singularity subtraction methods are as below:

1. The difference integrand cannot be well approximated by a polynomial in the vicinity of the singularity, thus limiting the achievable accuracy of quadrature rules.
2. The process of Taylor series representation of the subtracted singular term sometimes increase complications for higher order basis, curvilinear elements, or complicated Green's functions.

4.1.3 Regularization Techniques

In the regularization techniques, the singular integral is transformed to a regular integral by a coordinate transformation (e.g. [18, 113, 114]) or integration by parts (e.g. [115]). Strong singularities can be regularized by addition and subtraction of successive terms of a Taylor expansion of a singular kernel in order to isolate strongly singular integrands from the numerically calculated integrands. However, rigorous manipulations are involved in this regularization method [19].

In a method proposed in [18], weakly singular kernels are considered for quadrilateral domains which is divided into subdomains with the singular point, say (x'_1, y'_1) as a common vertex. The $O(1/R)$ type singular integral may be regularized by polar coordinate transformation such as [18]

$$\int_{-1}^{1}\int_{-1}^{1} f(x', y')dx'dy' = \int_{\varphi'_1}^{\varphi'_2}\int_{0}^{\rho'(\varphi')} f(x'_1+\rho'\cos\varphi', y'_1+\rho'\sin\varphi')\rho' d\varphi' d\rho' . \quad (4.6)$$

Additionally, the polar Gaussian quadrature is used to evaluate the integral which shows significantly fewer number of quadrature points required for a given accuracy as compared to the standard Gauss-Legendre quadrature.

For the treatment of $\frac{\boldsymbol{R}}{R^3}$−type hyper singularities, [19] provides one order reduction of singularity by using the regularization technique of [18] followed by a Taylor series expansion of the term $|\boldsymbol{r} - \boldsymbol{r}'|$ expressed in polar coordinates.

The treatment presented in [19] considers the situation when the observation point or its projection resides within or along the bounds of the source domain. In situations when observation point or its projection resides close to but outside the source domain (e.g. Fig. (4.1b) and (4.1d)), the method may require significantly large number of quadrature points for good accuracies.

4.1.4 Singularity Cancellation Technique

Most recently, singularity cancellation technique has come up for the treatment of singular integrals. In this technique fully numerical evaluation of singular integrals has been proposed. For $\frac{1}{R}-$type singular kernels the Jacobian of *Arcsinh*[3] transformation [20] exactly cancels out the singularity. Further, for the special cases when observation point is located on the plane of the source domain, the transformed domain is rectangular which enables the integration over the source domain with few sample points. For $\frac{\boldsymbol{R}}{R^3}-$type kernels, the Radial Angular-R^2 (RA-R^2) transformation [21, 116] cancels out the singularity. However, the transformed domain is not rectangular and, depending upon the observed geometry of the source domain, often large numbers of Gauss-Legendre sample points are required for integration over the source domain.

Now for near-singularities and near-hyper-singularities the observation point or its projection lies outside the source domain. The singularity cancellation transformation appear less efficient for such couplings. Therefore for the case of triangular domains at least one of the sub triangles lies completely outside the source triangle and the remaining sub triangles are also partially outside. Thus, most of the sample points lie outside the required integration domain. It is noteworthy that the contribution of outer sample points is finally subtracted from the overall result. This makes the scheme less efficient for the near- and near-hyper-singularities. As a remedy an adaptive singularity cancellation technique [22, 24] was proposed and is discussed in detail in upcoming sections.

4.1.5 Adaptive Singularity Cancellation Technique

Adaptive singularity cancellation technique [22, 24], keeps the benefits of the aforementioned singularity cancellation technique but avoids the time consuming repeated integrations over unnecessary sample points which reside out of the original source domain. Another important feature for the improvement

---

[3] In the present text *Arcsinh* refers to the inverse of *sinus hyperbolicus* which is commonly used, even though it is a misnomer notation. The inverses of the hyperbolic functions are the area hyperbolic functions and therefore the correct abbreviation is *Arsinh*. Heartiest thanks go to Prof. W. Rucker, Universität Stuttgart for the detailed clarification.

of efficiency is the appropriate choice of an adequate number of sample points according to the instantaneous shape of the transformed integration domain encountered during the analysis of a particular pair of source and test domains. Different numbers of sample points are chosen for different radial and angular dimensions of the transformed integration domain. For this, a criterion for optimum sample point distribution is presented.

In the following sections, treatment of singular integrals encountered in the MoM solution of surface integral equations while making use of singularity cancellation technique and its adaptive version will be discussed in detail.

4.2 Choice of Singularity Technique

As reviewed in section 4.1, various treatments can be found in the literature for the accurate computation of singular integrals encountered in the surface integral equation formulations. For the solution of EFIE with only electric current densities as unknown, only $\frac{1}{R}-$type singular integral of the form (4.1) comes into action. The MFIE for electric current density as unknown involves gradient of the Green's function which is responsible for the $\frac{\boldsymbol{R}}{R^3}-$type singularity of the form (4.2). We intend to develop a solver suitable for the solution of radiation and scattering problems of arbitrarily shaped open as well as closed surfaces composed of metallic and dielectric materials. Furthermore, unknown current densities are aimed to be modeled with higher-order polynomial expansion functions to achieve higher accuracies. Therefore, we searched for suitable singularity cancellation technique which can handle both $\frac{1}{R}-$ and $\frac{\boldsymbol{R}}{R^3}-$type singularities and at the same time must be straight forward for adaption to the higher-order polynomials.

Whereas singularity subtraction approaches discussed in section 4.1.2 provide better treatment of singularities, the separate handling for analytical and numerical terms involve rigorous programming. Furthermore, if the choice of basis functions is altered, the implemented code will not be directly applicable. The regularization techniques reviewed in section 4.1.3 produce regularized integrals even for higher-order basis functions. However, the available scheme (e.g. as reported in [19]) are applicable directly to quadrilateral domains. On the other hand, the singularity cancellation technique (see section 4.1.4) is a purely numerical treatment and applied directly to triangular domains. Therefore, we have opted this technique as a tool for the treatment of singular integrals in the MoM solutions of surface integral equation formulations.

4.3 Treatment of Singularities with Singularity Cancellation Technique

The singularity cancellation techniques proposed by Wilton and his co-workers [20, 21] for the treatment of $\frac{1}{R}-$ and $\frac{\boldsymbol{R}}{R^3}-$type singularities are discussed in this section.

4.3.1 *Arcsinh* Transformation

For $\frac{1}{R}-$type singular integral (4.1), the *Arcsinh* transformation is [20]

$$u = \text{Arcsinh}\left(\frac{x'}{\sqrt{\left(y'\right)^2 + z^2}}\right) \quad , \quad v = y' \, , \tag{4.7}$$

where the integration domain is assumed to lie in the $x'y'$-plane with origin at the projection of the observation point onto the plane (Fig. 4.2). The

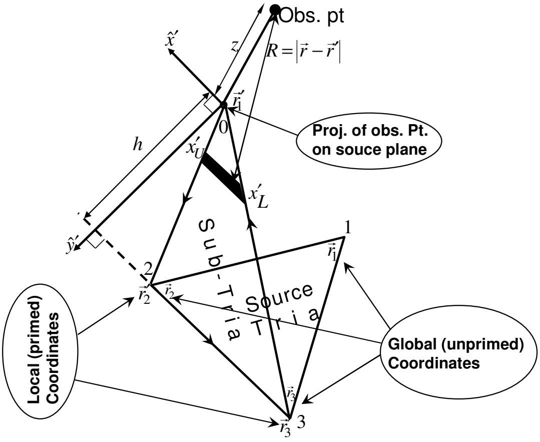

Fig. 4.2. Subtriangle geometry and coordinate system for near singularities under *Arcsinh* Transformation. For the figure, one subtriangle is completely outside the original source domain Δ123.

Jacobean of this transformation

$$J\left(u,v\right) \;=\; \begin{vmatrix} \frac{\partial x'}{\partial u} & \frac{\partial x'}{\partial v} \\ & \\ \frac{\partial y'}{\partial u} & \frac{\partial y'}{\partial v} \end{vmatrix} \;=\; R\,, \tag{4.8}$$

cancels out the singularity. After this transformation, the integral (4.1) looks like

$$\boldsymbol{B} \;=\; \int\limits_{v_L}^{v_U}\int\limits_{u_L}^{u_U} \boldsymbol{\beta}(\boldsymbol{r}')\; e^{-jkR} du dv\,, \tag{4.9}$$

where $v_{L,U}$ and $u_{L,U}$ are the lower and upper limits of integration in the transformed domain. These limits are determined according to the geometry of the subtriangle under consideration and can be computed as follow:

$$u_{L,U} = \text{Arcsinh}\left(\frac{x_{L,U}}{\sqrt{y^2+z^2}}\right)\;,\; v_{L,U} = y_{L,U}\;, \tag{4.10}$$

where for original scheme [20]

$$y_{L,U} = 0, h\,, \tag{4.11}$$

and h represents the height of projected observation point from the opposite edge of the subtriangle under consideration.

The integrand in (4.9) is now analytic in u and v and can therefore be integrated accurately using an appropriate quadrature rule (e.g. Gauss-Legendre quadrature rule). It is also interesting to note that for singularities with $z = 0$, the transformed $uv-$domain is rectangular. In such cases the integral (4.9) can be computed with very few sample points. For other situations, the domain is non-rectangular and sometimes large number of sample points are necessary. Excellent convergence results are however observed in this transformation.

4.3.2 Radial Angular-R^2 Transformation

For the treatment of $\frac{\boldsymbol{R}}{R^3}-$ type singular integrals (4.2), the Radial Angular-R^2 transformation

$$u = \phi = \text{Arctan}\left(\frac{y'}{x'}\right) \quad , \quad v = |z|\ln R\,, \tag{4.12}$$

is considered [21]. The geometry and coordinate system for RA-R^2 transformation applied to triangular domains are shown in Fig. 4.3. The Jacobean of

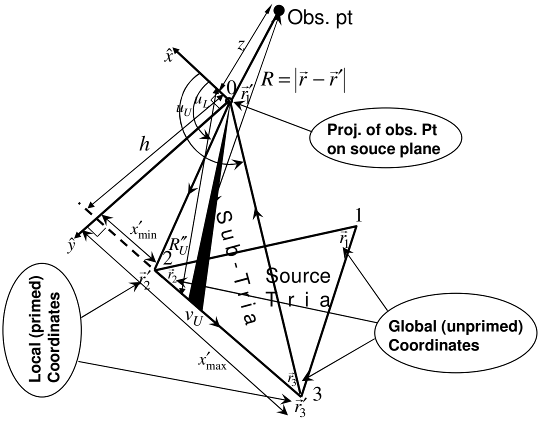

Fig. 4.3. Subtriangle geometry and coordinate system for near singularities under RA-R^2 transformation. For the figure, one subtriangle is completely outside the original source domain Δ123.

this transformation is $-\frac{R^2}{|z|}$, which cancels out the singularity. The limits of integration in the RA-R^2 transformation are given by

$$u_{L,U} = \phi_{L,U} \ , \ v_{L,U} = \frac{|z|}{2} \ln \left[z^2 + \left(R''_{L,U}(u) \right)^2 \right] , \tag{4.13}$$

where for original scheme [116]

$$R''_{L,U}(u) = 0, \frac{h}{\sin(u)} \, . \tag{4.14}$$

The transformed integration domain in RA-R^2 transformation is not rectangular and is deformed as the observation point moves closer to the source or integration domain. Therefore, often very large numbers of sample points are necessary for sufficiently good accuracies.

4.3.3 Drawbacks of Originally Proposed Singularity Cancellation Transformations

The originally proposed singularity cancellation transformations reviewed above provide a purely numerical method for exact cancellation of $\frac{1}{R}-$ and $\frac{\boldsymbol{R}}{R^3}-$type singularities encountered in surface integral equation formulation of electromagnetics. However, they appeared less efficient for near-singular and near-hypersingular couplings. The reason is that the observation point or its projection lies outside the source domain. In case of triangular domains at least one of the subtriangles lies completely outside the source triangle and the remaining subtriangles are also partially outside. Thus, most of the sample points lie outside the required integration domain. The contribution of outer sample points is finally subtracted from the overall result. In order to avoid the time-consuming integration over such sample points, we propose in section 4.4, an adaptive singularity cancellation technique, which locates all sample points within the desired integration domain and hence significant improvement in the computational efficiency of the coupling matrices is achieved.

Furthermore, the convergence behavior of the original singularity cancellation transformations is very sensitive to the height $|z|$ of observation point above the plane of source domain. Often very large number of sample points are needed for original schemes which badly degrades the computational efficiency. In [21], two different transformations were proposed to handle this problem. RA-R^2 was employed for higher values of $|z|$ and RA-R^3 was suggested for lower values of $|z|$. In fact this is not a preferable solution in relevance to object-oriented programming. The adaptive scheme inherently removes this problem and converges fastly independent of the so-called$|z|-$variations.

4.4 Treatment of Singularities with Adaptive Singularity Cancellation Technique

The singularity cancellation technique works well for singular and hyper-singular integrals. However, as discussed in section 4.3.3, some improvements in the treatment of near-singular as well as near-hyper-singular kernels are sought. Therefore, an adaptive version of singularity cancellation technique is presented to remove the drawbacks of the original approach.

4.4.1 Geometrical Configuration for Near Singular Integrals

Dependent on the location of the projection of the observation point, two different geometrical configurations for near-singularities are possible, as shown in Figs. 4.4 and 4.5. The original singularity cancellation scheme divides the original triangle into three sub triangles and integration over all sub triangles starts from the local origin (i.e. observation point or its projection). As such, one sub triangle is completely outside the source domain for the geometry of Fig. 4.4, and two sub triangles are completely outside the source domain in the case of Fig. 4.5. The remaining sub triangles are also partially outside the source domain.

In our proposed scheme, only two sub triangles are taken into account, which constitute the original source domain. The two sub triangles, SubTria-1 and SubTria-2, are shown shaded in Figs. 4.4 and 4.5. To achieve this, the adaptive formulation modifies the limits of integration as compared to the originally proposed singularity cancellation techniques.

4.4.2 Adaptive Limits of Integration for *Arcsinh* Transformation

For $\frac{1}{R}$-type singularities, the lower and upper limits x_L and x_U in the *Arcsinh* transformation are constrained by the boundaries of the sub triangle under consideration. These limits can be determined from the intersection of lines. For the geometry of Fig. 4.4, the integration limits are given by

$$\begin{aligned} y_{L,U} &= m_2\left(\frac{y_1 - m_1 x_1}{m_2 - m_1}\right),\ h\,, && (4.15)\\ x_{L,U}(y) &= \frac{y}{m_2},\ \frac{y - y_1 + m_1 x_1}{m_1}\,. && (4.16) \end{aligned}$$

Similarly, for the geometry of Fig. 4.5, the integration limits are given by

$$\begin{aligned} y_{L,U} &= h,\ m_2\left(\frac{y_1 - m_1 x_1}{m_2 - m_1}\right)\,, && (4.17)\\ x_{L,U}(y) &= \frac{y - y_1 + m_1 x_1}{m_1},\ \frac{y}{m_2}\,, && (4.18) \end{aligned}$$

where

$$m_1 = \frac{y_2 - y_1}{x_2 - x_1}\,, \qquad \text{and} \qquad m_2 = \frac{y_3}{x_3}\,, \tag{4.19}$$

are the slopes of the two sides of the source triangle.

4.4.3 Adaptive Limits of Integration for Radial Angular-R^2 Transformation

For RA-R^2 transformation, the angular limits $u_{L,U}$ of integration are those of the original scheme (see (4.13)). However, the modified limits of integration in the radial direction $v_{L,U}$ given in (4.13) are modified such that

$$R''_{L,U}(u) = \begin{cases} \frac{h_3}{\sin(\delta)},\ \frac{h}{\sin(u)} & \text{for Fig. 4.4}\,,\\ \frac{h}{\sin(u)},\ \frac{h_3}{\sin(\delta)} & \text{for Fig. 4.5}\,, \end{cases} \tag{4.20}$$

instead of (4.14). Equation (4.20) represents the respective instantaneous radial distances. Here, h represents the perpendicular distance of projection of the observation point from the opposite edge ($|23|$ or $|31|$) in the sub triangle under consideration, h_3 is the perpendicular distance from the edge $|12|$ and δ is the angle of instantaneous radius vector $R^{''}$ as measured with edge $|12|$ (Figs. 4.4 and 4.5).

4.4.4 Adaptive Criterion for Distribution of Sample Points

The selection of the number of sample points in the transformed non rectangular domain is of critical nature. The deformation in the transformed domain becomes more and more pronounced as the projected observation point moves closer to the boundary of the original source domain and a larger number of sample points is needed to achieve accurate results. Also, it is observed that the integrands exhibit larger variations when the size of the integration domain relative to its distance from the projection of the observation point becomes larger. Therefore, a real-time selection of distribution of sample points for the particular geometry encountered is employed in order to account for the particular deformations and integrand variations, and to enhance the efficiency of the solver to a great extent. As in the original schemes, the Gaussian quadrature rule is applied however, the number of sample points is selected proportional to the observed relative angular and radial dimensions (with respect to the observation point or its projection) of the instantaneous slice of the sub triangle under consideration. The instantaneous check on the ratio of the length of the slice to its radial proximity from the projection of the observation point enables the use of optimum numbers of sample points.

The parameters $\alpha_\phi = \left|\frac{\phi_U - \phi_L}{\pi}\right|$ and $\alpha_R = \left|\frac{R^{''}_U - R^{''}_L}{R^{''}_U}\right|$ are proposed for the adaptive selection criterion in the angular and radial directions, respectively. For smaller angular dimensions, described by smaller values of α_ϕ, as few as two sample points are sufficient (assuming linear vector basis functions), whereas for larger angular dimensions, described by larger values of α_ϕ, more sample points are required for good accuracies. Similarly, more sample points are required for larger values of α_R. Although the number of sample points in a particular radial or angular segment are proportional to $\alpha_{R,\phi}$, yet, the exact numbers depend on the desired accuracy and can be determined from the numerical experiments. For our requirements, we have subdivided the complete range of $\alpha_{R,\phi} \in [0, 1]$ into four segments and used different numbers of samples for different segments.

In order to demonstrate the adaptive selection of the number of sample points

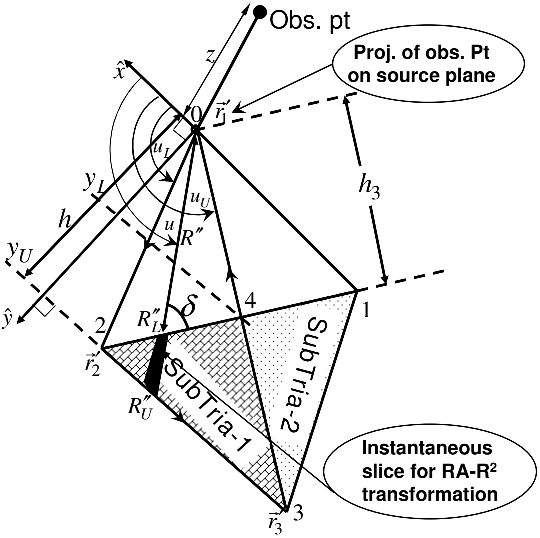

Fig. 4.4. Geometry and coordinate system of sub triangles in source domain when one sub triangle is completely outside the original source domain $\Delta 123$.

in radial and angular directions, in Fig. 4.6 a fixed source domain is shown for two different observation points. In Fig. 4.6(a), as seen from the observation point, the angular domain of the right-sided sub triangle is larger than that of the left-sided sub triangle. Therefore, the adaptive scheme chooses 8 samples in angular direction for the right-sided sub triangle and 2 angular samples for the left-sided sub triangle. Moreover, because the instantaneous slices are not very broad in the radial direction, only two sample points in radial direction are chosen. However, in Fig. 4.6(b) the angular domain as observed from the observation point is very small and, therefore, only two angular samples are chosen. Since each instantaneous radial slice is of significantly different size, the adaptive scheme chooses more samples (i.e. 8) for the larger slice and less sample points (i.e. 2) for the smaller slice.

4.5 Numerical Results

A comparison of distribution of Gauss-Legendre sample points in the original and adaptive RA-R^2 singularity cancellation transformations is shown in Fig.

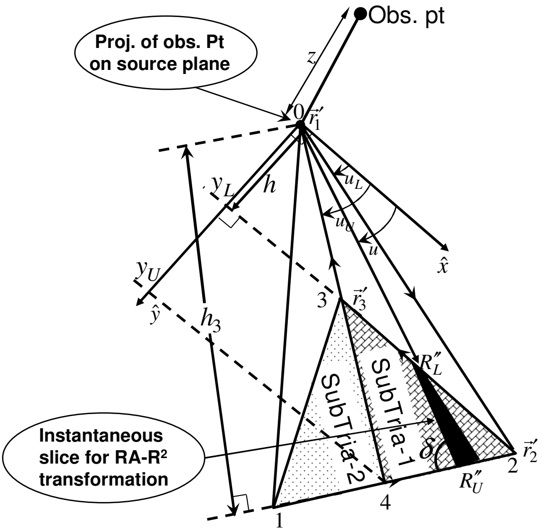

Fig. 4.5. Geometry and coordinate system of sub triangles in source domain when two sub triangles are completely outside the original source domain $\Delta 123$.

4.7. It can be observed that for 4×4 distribution of sample points per sub triangle, the original scheme uses a total of $4 \times 4 \times 3 = 48$ points in the source triangle, out of which only a few are located within the desired source domain. However, the proposed scheme utilizes $4 \times 4 \times 2 = 32$ points, all of which are located completely inside the source domain. This enables the computation of accurate results with fewer sample points.

In the subsequent results, the real part of the potential integral (4.1) with scalar basis function for *Arcsinh* and real part of the normal component of (4.1) with Rao-Wilton-Glission vector basis functions for RA-R^2 were computed at 10 m wavelength.

4.5.1 Convergence Tests for RA-R^2 Transformation

In Fig. 4.8, the convergence of the original and adaptive schemes is presented for the calculation of potential gradient integral (4.2). The proposed scheme converges for a total of $2 \times 2 \times 2 = 8$ sample points, whereas the original scheme is approximately converged with $5 \times 5 \times 3 = 75$ sample points. In Fig. 4.9, we

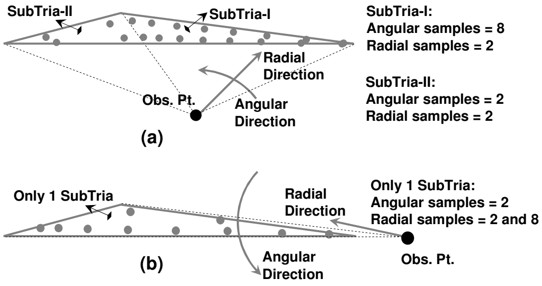

Fig. 4.6. Adaptive distribution of sample points for a fixed source domain and two different observation point.

consider a special case in which the source domain is highly deformed. The integral (4.2) was computed using the original and adaptive RA-R^2 schemes. The adaptive scheme is remarkably faster than the original one.

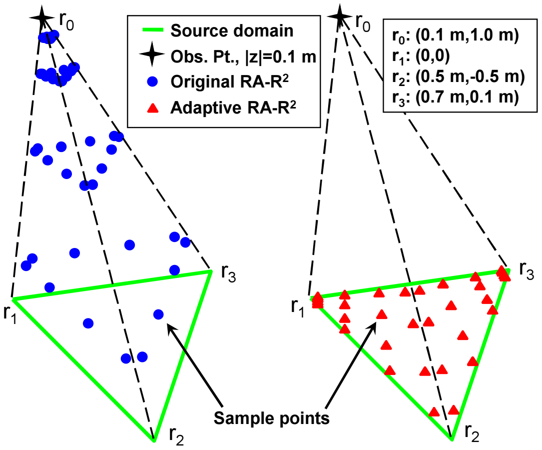

Fig. 4.7. Comparison of distribution of Gauss-Legendre sample points for a near-singularity in the original and adaptive RA-R^2 transformations.

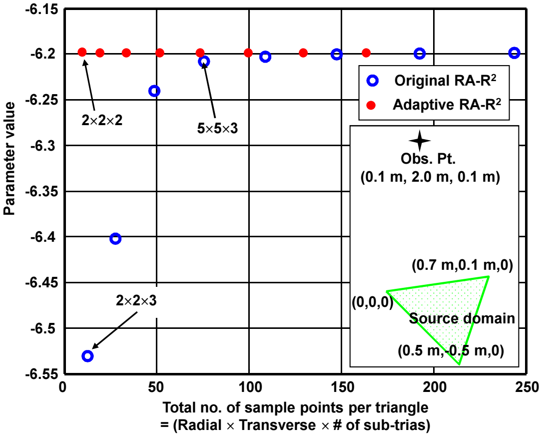

Fig. 4.8. Convergence results of a near-singularity in the original and adaptive RA-R^2 transformations for the computation of (4.2) over the source domain shown in the lower legend.

4.5.2 Convergence Tests for *Arcsinh* Transformation

In another example, we consider a right triangular source domain with vertices (0, 0, 0), (1 m, 0, 0) and (0, 1 m, 0). The observation point is taken at (-0.1 m, 0.1 m, 0.01 m). A comparison of convergence behavior in original and adaptive *Arcsinh* transformations is presented in Fig. 4.10. The highly efficient converging behavior of the adaptive *Arcsinh* transformation is self evident. Similar to RA-R^2, the adaptive *Arcsinh* scheme converges fastly even for highly deformed geometries.

4.5.3 Convergence Tests for Various $|z|$-values of Observation Point

Another interesting benefit of the adaptive scheme over the original scheme is that it converges rapidly independent of height of observation point above the plane of source domain. For this purpose, the geometry being used has the vertices (0, 0, 0), (0.5 m, -0.5 m, 0) and (0.7 m, 0.1 m, 0). The near-singular observation point is located at (0.1 m, 2.0 m, $|z|$). A comparison of convergence behaviors of original and adaptive RA-R^2 schemes for two different heights $|z| = 0.1$ m, 0.0001 m, is presented in Fig. 4.11. This shows that the convergence behavior of original RA-R^2 transformations is highly

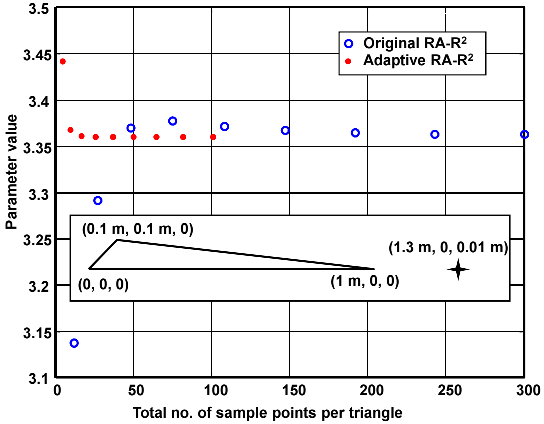

Fig. 4.9. Convergence results of the original and adaptive RA-R^2 transformations for the computation of (4.2) over a degenerate source domain shown in the lower legend.

sensitive to the height $|z|$ of the observation point above the source plane. The sensitivity to $|z|$-variations of the original RA-R^2 scheme is due to the fact that as the height of observation point above the source plane is decreased, the quadrature points start clustering more closer to the observation point. Since for near-singularities, the observation point resides outside the actual source domain, the number of samples which are inside the original source domain are reduced and hence the accuracy of the computation becomes worse. However, this is not the case for the proposed adaptive transformations. Because all of the quadrature points already reside completely inside the original source domain, therefore the adaptive version of the transformation converges with fewer sample points regardless of the height of the observation point over source plane. Similarly the convergence of adaptive *Arcsinh* scheme has been found independent of $|z|$-variations in the observation point.

4.5.4 Mean Error Versus Quadrature Samples

The mean error in the numerical integrations of original and adaptive schemes for RA-R^2 transformations is compared in Fig. 4.12 for the above geometry given in the legend. For given accuracies, the original scheme requires a large number of samples as compared to the adaptive one. The mean error curve for the adaptive scheme has a much sharper inclination than the original one.

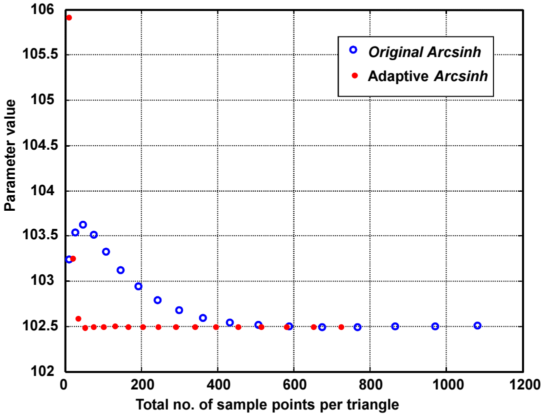

Fig. 4.10. Convergence results of a near-singularity in the original and adaptive *Arcsinh* transformations for the computation of (4.1).

Thus for higher accuracies, the adaptive scheme converges remarkably faster. Similarly, the mean error in the numerical integrations of the original and adaptive *Arcsinh* transformations is compared in Fig. 4.13. Evidently, the adaptive scheme requires a much smaller number of samples as compared to the original one for a desired accuracy.

4.5.5 Computational Cost

A comparison of the computational efficiencies of the original and adaptive schemes was carried out under the same memory and speed environments for the computation of the near field matrix for a problem with 135 876 unknowns. For a comparable accuracy of the order of 2 significant digits, the original scheme took 2 926 seconds whereas the adaptive scheme took 606 seconds. This explains the effectiveness of the adaptive scheme over the original scheme in terms of numerical computational cost. Finally, a fully metallic car body with 4 monopole antennas on its top was analysed with a code based on the adaptive scheme. The MoM model consisted of 3.1 million Rao-Wilton-Glisson unknowns and the computation time for about 376 million near-coupling contributions required in the Multilevel Fast Multipole accelerated code was 7 076.6 sec on an AMD Opteron 2.8 GHz processor.

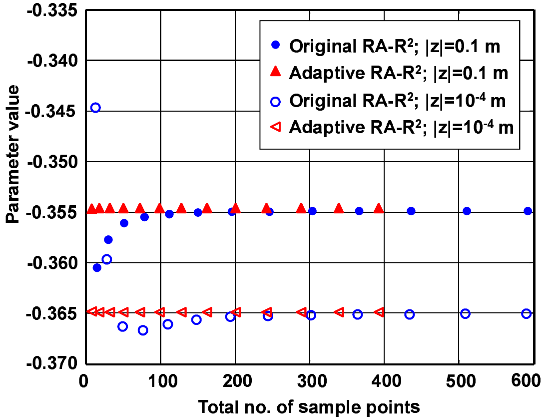

Fig. 4.11. Comparison of convergence behavior of original and adaptive RA-R^2 transformations for different heights $|z|$ of observation point over the source domain for the computation of potential gradient integral (4.2).

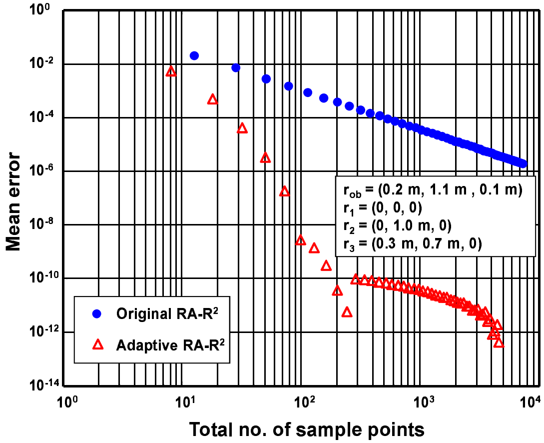

Fig. 4.12. Mean error in the numerical integrations in the original and adaptive RA-R^2 transformations.

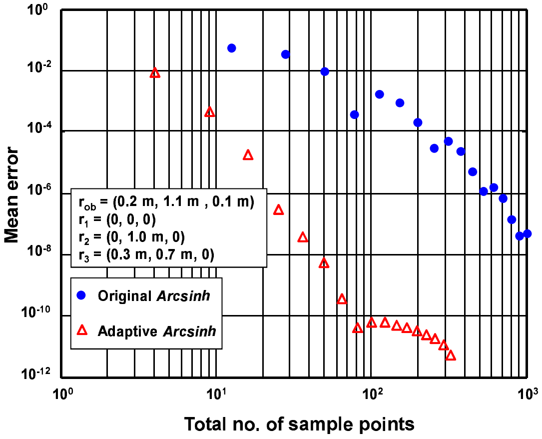

Fig. 4.13. Mean error in the numerical integrations in the original and adaptive *Arcsinh* transformations.

5 Surface Current Modeling with Hierarchical Basis Functions

Higher-order basis functions interpolate the field intensities and current densities over sufficiently smooth surfaces more accurately than their lower-order counterparts. However, near edges and corners lower-order interpolations are often even more efficient. Hierarchical basis functions are formed by adding new higher-order basis functions to lower-order ones. A set of hierarchical higher-order basis functions which makes the formulation complete to full first order with respect to the divergence of the basis functions has been implemented in the MoM solution of surface integral equations under full utilization of the developed adaptive singularity cancellation method and is described in the following sections.

5.1 Introduction

In the method of moments solution of surface integral equation formulations for the boundary value problems in electromagnetics, the low-order vector basis functions are widely used for the modeling of electromagnetic field intensities and corresponding current densities. However, these basis functions have the fundamental shortcoming that often dense geometrical discretization is necessary for sufficiently good accuracies. In other words, the average size of the surface and/or volumetric geometrical elements is on the order of $\frac{\lambda}{10}$ in each dimension, λ being the wavelength in the medium. This results in a very large number of unknown current/field expansion coefficients [25–31]. Furthermore, the accuracy of the solution while using the LO bases is improved slowly with increasing the number of unknowns.

Great reduction of the number of unknowns for a given problem and desired accuracy is achievable through the use of higher-order basis functions [25–33]. Motivated with the benefits of HO basis functions over the LO counterparts, HO modeling of surface current densities in the MoM solution of surface IEs is implemented [117, 118] and hence discussed below.

5.2 Complete Versus Mixed-Order Basis Functions

Using Helmholtz's decomposition, a vector field $\boldsymbol{F}$ may be resolved into curl-free (alternate names are gradient or irrotational) component and divergence-free (also known as rotational or solenoidal) component vector fields [29, 104]

$$\boldsymbol{F} = \nabla\phi + \nabla \times \boldsymbol{A}, \quad \nabla \cdot \boldsymbol{A} = 0\,, \tag{5.1}$$

where ϕ and $\boldsymbol{A}$ are respectively known as scalar and vector potentials of the vector field $\boldsymbol{F}$. The first term $\nabla\phi$ in (5.1) represents curl-free component and second term $\nabla \times \boldsymbol{A}$ is the divergence-free component.

The electromagnetic formulation for the field solutions consists of two terms, one related to the curl of the field and other to the field itself. The curl of a field (say electric field) is the time rate of change of its counterpart field (magnetic field). Similarly, the integral equations for the modeling of surface current densities involve the current density as well as its divergence. The divergence of the current density corresponds to the time rate of change of charge density. The hierarchical basis functions (e.g. [29, 30, 33]) try to provide separate representation of curl-free and divergence-free components of the vector fields. The idea of mixed-order[1] vector elements is to remove terms from the polynomial approximation of the field or current which do not contribute to its curl or divergence respectively [33, 119]. That is, the curl-free field component or divergence-free current components of the highest order of basis functions may be removed from the field or current modeling respectively without the loss of accuracy. If both the curl-free and divergence-free components of the highest order basis functions are incorporated in the modeling of fields/currents, the formulation is known as full-order or complete space with respect to basis functions.

Davidson [119] and Webb [33] have demonstrated that the problems where the electric and magnetic fields are of more or less equal importance, the use of mixed-order vector elements is beneficial to obtain maximum accuracy for a given number of unknowns. A sharp edge, for example, will result in a singularity in both the electric and the magnetic fields. However, in problems where either electric or magnetic field is dominated, the mixed-order formulation is not preferable. For example, for certain field and discontinuity orientations, such as partially blocked parallel plate waveguide excited by the electric field, the singularity is in the electric field alone which is strongly gradient in nature. In such situations, the curl of the electric field, that is the magnetic field, is

---

[1] In case of field modeling, mixed-order vector elements are also known as reduced-gradient elements.

relatively less important and hence the mixed-order formulation becomes less efficient than the complete representation.

In our implementation [117, 118], the curl-free components of first-order and curl space of the second-order were added to the existing low order RWG [34] bases, which makes the formulation complete to full first order with respect to the curl or divergence of the basis functions.

5.3 Choice of Basis Functions

Higher-order current and field modeling in electromagnetics can be achieved using interpolatory or hierarchical vector basis functions, in both divergence and curl-conforming arrangements. The interpolatory basis functions are defined on a set of points on an element, such that each basis function is of the same order and typically vanishes at all the points except for one. These basis functions possess good linear independence and thus the matrix system is well conditioned. Unfortunately, the interpolatory basis functions of a given order are completely different from those of the lower order. Thus basis functions of different orders cannot easily be used together. On the other hand, the basis functions are said to be hierarchical, if the LO basis functions form a subspace of the HO basis functions. The use of basis functions of different orders in a problem is therefore possible with the hierarchical basis functions.

In contrast to the interpolatory basis functions, the hierarchical basis functions suffer from a weakness that as the order increases, the system matrix becomes ill-conditioned, which worsens the convergence rate of the iterative solver. However, if the basis vectors are made orthogonal, a better conditioned system matrix may be obtained. Nearly-orthogonal set of field basis functions [29, 30] for flat triangles is our choice for possibly better conditioned system matrix. Another class of near-orthogonal basis functions for curvilinear quadrilaterals is presented in [28].

In the context of finite element modeling, the tangential continuity of the field intensities is guaranteed through the use of tangentially continuous set of basis vectors. Similarly, the set of basis functions most suitable for the modeling of current densities in the MoM solution of integral equations must guarantee the normal continuity. The work presented here benefits from the use of tangentially continuous field basis functions $\boldsymbol{\alpha}_n$ [29, 30], which are transformed into normally continuous current counterparts $\boldsymbol{f}_n$ using [25, 26]

$$\boldsymbol{f}_n = \hat{n} \times \boldsymbol{\alpha}_n \,, \tag{5.2}$$

where $\hat{n}$ is the outward directed unit surface normal.

The selected basis functions complete to full first order for the curl or divergence of the basis functions, along with their characteristics necessary for the MoM system matrix setup are given in Table 5.1 and presented graphically in Fig. 5.1.

For the higher order modeling of current densities, the matrix elements namely (3.35)-(3.42), of the governing surface integral equations have to be computed to include the additional interactions between LO and HO basis functions.

As can be seen from the Table 5.1, a general form of vector basis functions for the present implementation is

$$\boldsymbol{f}_n = \frac{u(\lambda_1, \lambda_2)\, \boldsymbol{t}_{12} + v(\lambda_1, \lambda_2)\, \boldsymbol{t}_{23} + w(\lambda_1, \lambda_2)\, \boldsymbol{t}_{13}}{2A}, \tag{5.3}$$

where $\boldsymbol{t}_{ij}$ are the edge vectors of the element under consideration as shown in Fig. 5.2, A is the surface area of the element, and u, v and w are polynomial functions of the normalized barycentric (simplex) coordinates λ_1, λ_2. It is to be noted that the edge vectors are constant vectors for a pair of testing and source elements.

Now basis-by-basis evaluation of the coupling integrals (3.35)-(3.42) enables the quicker adaption of lower order existing formulation to HO counterpart. As pointed out in [34], the integral evaluation can be made efficient by rewriting the expressions such that the terms involving constant edge vectors $\boldsymbol{t}_{ij}$ are taken out of the integrand and the necessary scalar integrals containing barycentric polynomials u, v, w and the scalar Green's function G_0 are evaluated once. An exemplary problem is computed with basis-by-basis evaluation procedure as well as with scalar barycentric integral approach and is reported in the section 5.6 to compare computational costs.

5.4 Iterative Solver Matrix-Vector Product

The MoM solution of IEs results in a system of linear equation

$$[Z]\,\{x\} = \{b\}\ , \tag{5.4}$$

where $[Z]$ is the fully populated coupling matrix, $\{b\}$ is the excitation vector and $\{x\}$ represents the expansion coefficients of the discretized unknown surface current density. For large problems, it is mandatory to solve the equation system by an iterative method [120], where especially the generalized minimal residual algorithm (GMRES) is attractive. These equation solvers require the repeated evaluation of matrix-vector products $[Z]\,\{x\}$. To speed-up the computation of matrix-vector products, the MLFMM algorithm is used. In many situations, the convergence of a simple iterative algorithm is not satisfactory and

TABLE 5.1
HIGHER-ORDER BASIS FUNCTIONS AND THEIR PROPERTIES (WITHIN THE TRIANGLES).

		MoM vector basis functions		$\nabla \cdot \boldsymbol{f}_n$	$\nabla \times \boldsymbol{f}_n$ $= -\left[\nabla \cdot (\hat{n} \times \boldsymbol{f}_n)\right] \hat{n}$
R^1	$\boldsymbol{f}_0$	$\hat{n} \times (\lambda_1 \nabla\lambda_2 - \lambda_2 \nabla\lambda_1)$	$\dfrac{\lambda_1 \boldsymbol{t}_{13} + \lambda_2 \boldsymbol{t}_{23}}{2A}$	$-\dfrac{1}{A}$	0
	$\boldsymbol{f}_1$	$\hat{n} \times (\lambda_1 \nabla\lambda_3 - \lambda_3 \nabla\lambda_1)$	$\dfrac{-\lambda_1 \boldsymbol{t}_{12} + \lambda_3 \boldsymbol{t}_{23}}{2A}$	$\dfrac{1}{A}$	0
	$\boldsymbol{f}_2$	$\hat{n} \times (\lambda_2 \nabla\lambda_3 - \lambda_3 \nabla\lambda_2)$	$\dfrac{-\lambda_2 \boldsymbol{t}_{12} - \lambda_3 \boldsymbol{t}_{13}}{2A}$	$-\dfrac{1}{A}$	0
G^1	$\boldsymbol{f}_3$	$\hat{n} \times (\lambda_1 \nabla\lambda_2 + \lambda_2 \nabla\lambda_1)$	$\dfrac{\lambda_1 \boldsymbol{t}_{13} - \lambda_2 \boldsymbol{t}_{23}}{2A}$	0	$2\,(\nabla\lambda_1 \cdot \nabla\lambda_2)\,\hat{n}$
	$\boldsymbol{f}_4$	$\hat{n} \times (\lambda_1 \nabla\lambda_3 + \lambda_3 \nabla\lambda_1)$	$\dfrac{-\lambda_1 \boldsymbol{t}_{12} - \lambda_3 \boldsymbol{t}_{23}}{2A}$	0	$2\,(\nabla\lambda_1 \cdot \nabla\lambda_3)\,\hat{n}$
	$\boldsymbol{f}_5$	$\hat{n} \times (\lambda_2 \nabla\lambda_3 + \lambda_3 \nabla\lambda_2)$	$\dfrac{-\lambda_2 \boldsymbol{t}_{12} + \lambda_3 \boldsymbol{t}_{13}}{2A}$	0	$2\,(\nabla\lambda_2 \cdot \nabla\lambda_3)\,\hat{n}$
R^2	$\boldsymbol{f}_6$	$\hat{n} \times (\lambda_1 \lambda_2 \nabla\lambda_3 + \lambda_3 \lambda_2 \nabla\lambda_1$ $-2\lambda_3 \lambda_1 \nabla\lambda_2)$	$\dfrac{-\lambda_1 \lambda_2 \boldsymbol{t}_{12} - \lambda_3 \lambda_2 \boldsymbol{t}_{23} - 2\lambda_3 \lambda_1 \boldsymbol{t}_{13}}{2A}$	$\dfrac{3\,(-\lambda_1 + \lambda_3)}{2A}$	$(-\lambda_1 \nabla\lambda_2 \cdot \nabla\lambda_3$ $+2\lambda_2 \nabla\lambda_3 \cdot \nabla\lambda_1$ $-\lambda_3 \nabla\lambda_1 \cdot \nabla\lambda_2)\,\hat{n}$
	$\boldsymbol{f}_7$	$\hat{n} \times (\lambda_1 \lambda_2 \nabla\lambda_3 - \lambda_3 \lambda_2 \nabla\lambda_1)$	$\dfrac{-\lambda_1 \lambda_2 \boldsymbol{t}_{12} + \lambda_3 \lambda_2 \boldsymbol{t}_{23}}{2A}$	$\dfrac{-\lambda_1 + 2\lambda_2 - \lambda_3}{2A}$	$(-\lambda_1 \nabla\lambda_2 \cdot \nabla\lambda_3$ $-\lambda_3 \nabla\lambda_1 \cdot \nabla\lambda_2)\,\hat{n}$

Note: $\boldsymbol{t}_{ij}$ are the edge vectors of the element 123 (Fig. 5.2) and are directed from the i-th node to the j-th node. A is the surface area of the element under consideration.

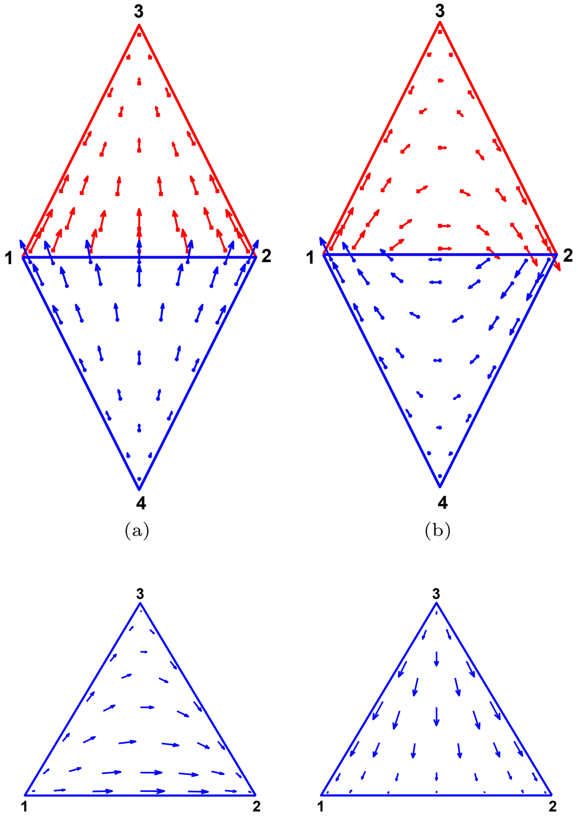

(a) (b)

(c)

Fig. 5.1. Graphical representation of the basis functions $\boldsymbol{f}_n = \hat{n} \times \boldsymbol{\alpha}_n$: (a) 1^{st} order, edge associated, rotational space, (b) 1^{st} order, edge associated, gradient space and (c) 2^{nd} order, face associated, rotational space. The terms rotational and gradient spaces are with respect to the $\boldsymbol{\alpha}_n$. Basis functions (a) and (b) are associated with the common edge 12 of the two contiguous triangles. The 2^{nd} order basis functions (c) are associated with the face 123. Addition of the bases (b) and (c) to those of (a) will build a set of basis functions complete to full first order with respect to the curl or divergence of the basis functions. For the modeling of an unknown quantity (e.g. either electric or magnetic current density) inside an element, one basis function of each type (a) and (b) is associated with each edge, and two basis functions of type (c) are associated with each face of the element.

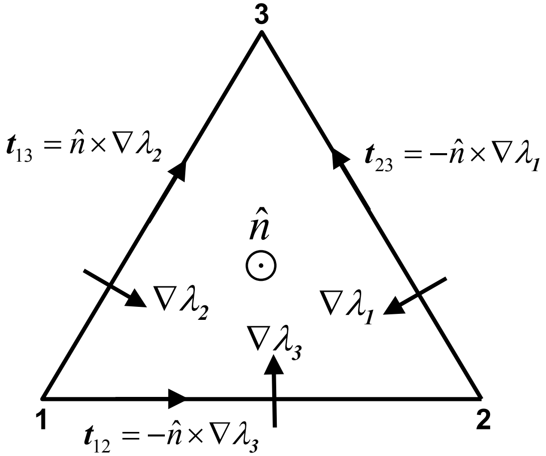

Fig. 5.2. Vectorial representation on a triangular element under the local coordinate system for the illustration of vector basis functions.

improved convergence behavior is sought to be obtained by preconditioning the equation system according to (e.g. left-hand side preconditioner) [120, 121]

$$\left[\tilde{Z}\right]^{-1}\left([Z]\{x\} = \{b\}\right), \tag{5.5}$$

where $\left[\tilde{Z}\right]$ is an approximation of $[Z]$ that is relatively cheaper to invert, but can also be chosen identical to the original matrices [121]. $\left[\tilde{Z}\right]^{-1}$ is iteratively computed as suggested in [122] and illustrated in Fig. 5.3. When the iterative preconditioner is applied, the iteration loop is broken after each matrix-vector product and another iteration loop is started to compute $\left[\tilde{Z}\right]^{-1}\{y\}$, where $\{y\}$ is the result of the matrix-vector product in the main iteration loop. In contrast to the main iteration loop, the preconditioner iteration loop is not necessarily iterated until convergence is achieved. To obtain a cheap preconditioner, it is terminated as early as possible. However, convergence must be good enough to have a useful preconditioner and to obtain a stable overall iteration process. To improve the convergence of the preconditioner iteration, the concept in [122] has been extended in [121] and further preconditioning levels were introduced. The preconditioner iteration loop is broken again and another iteration loop is started to precondition the preconditioner. The second preconditioner is generated with the matrix $\left[\tilde{\tilde{Z}}\right]$ which is an approximation

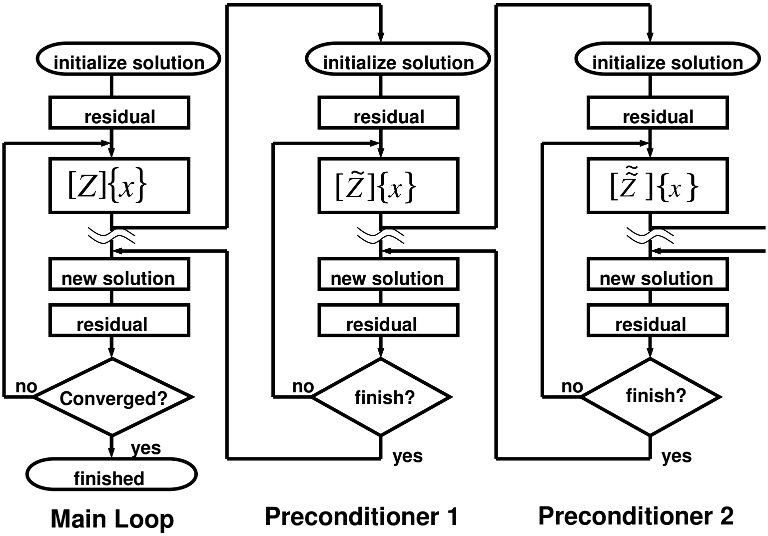

Fig. 5.3. Recursive iterative solution of linear equation system.

of $\left[\tilde{Z}\right]$. It has been reported in [121] that two preconditioner levels are sufficiently advantageous. The matrix-vector product computations are speeded up by this method. This recursive iterative solver is known as the flexible generalized minimal residual algorithm (F-GMRES) and will be applied for the solutions of numerical examples presented in section 5.6.

5.5 Multilevel Fast Multipole Method

In the standard FMM and MLFMM approaches [3, 5, 35, 36], based on edge-to-edge interactions, the minimum FMM group size and the number of FMM levels are limited by the size of the largest elements in the geometrical modeling of the object, as long as the group sizes are larger than that dictated by the so-called low-frequency breakdown of FMM [5]. Now because of the larger element size with the HO basis functions, the FMM group size is larger than that with LO basis functions. Equivalently, fewer number of FMM levels are permissible which in turn restricts full utilization of the MLFMM memory and computational efficiencies for high-frequency applications, where the basis function density is kept as low as possible. Further, with the increasing order of the basis functions, the average number of unknowns per element is also increased resulting in a denser FMM group in terms of unknowns with HO bases than with the LO bases. Consequently, associated with each HO basis function, more near couplings must be evaluated and stored which makes the traditional MLFMM relatively inefficient. A point-based multilevel fast multipole algorithm (MLFMA) [37], as an example, has tackled this problem by implementing MLFMM based upon the point-to-point interactions permitting two more FMM levels compared to the traditional basis-based MLFMM. In point-based MLFMA, the memory requirement for the storage of radiation and receiving patterns for each basis has been reported to be reduced by a factor of about 4 but that associated with the near field interactions is unchanged in comparison with the basis-based MLFMM. However, the SE-MLFMM [6] is inherently more efficient in terms of memory and computational cost even with edge-to-edge interactions due to the efficient storage of the k-space representations of the individual basis functions. SE-MLFMM has therefore been utilized in the current implementation to accelerate the HO bases based MoM solution of IEs.

The memory savings in SE-MLFMM have been achieved using the spherical harmonics expansion of the k-space representations of the basis/testing functions. The k-space representation of the basis functions $\boldsymbol{f}_n(\boldsymbol{r})$ belonging to an FMM group with its center index n', is given by [5, 6]

$$\widetilde{\boldsymbol{f}}_n(\hat{k}) = \oiint\limits_{S_o} \boldsymbol{f}_n(\boldsymbol{r}) \mathrm{e}^{j\boldsymbol{k}\cdot(\boldsymbol{r}-\boldsymbol{r}_{n'})}\, ds' \,. \tag{5.6}$$

For the memory efficient representation of $\widetilde{\boldsymbol{f}}_n$, the orthonormalized spherical harmonics Y_{pq} [36, 123]

$$\mathrm{Y}_{pq}(\theta,\phi) = \sqrt{\frac{(p-q)!}{(p+q)!}\frac{(2p+1)}{4\pi}} P_p^q\,(\cos\theta)\, e^{jq\phi} \,, \tag{5.7}$$

with P_p^q being the associated Legendre polynomials of degree p and order q are used for its expansion according to

$$\widetilde{\boldsymbol{f}}_n(\theta,\phi) = \sum_{p=0}^{P} \sum_{q=-p}^{p} \boldsymbol{f}_{pq}^{n} \mathrm{Y}_{pq}(\theta,\phi) \,, \tag{5.8}$$

where $\boldsymbol{f}_{pq}^{n}$ represent the SE coefficients and P is the SE degree. For further details on the formulation of SE-MLFMM interested readers may refer to [6].

It is known from [36] that the spherical harmonics (5.8) at the finest level in the expansion of basis functions decay rapidly for $P > \frac{L}{2}$, L being the number of multipoles (2.23) at the finest level in the expansion of translation operator. According to [6], this choice of degree P of spherical harmonics is valid when only the tangential components (i.e. spherical vector components) of the basis/testing functions are considered in the FMM formulations. This makes it sufficient to store $\hat{k}$-space representations for these two vector components. However, as reported in [6] the spectral contents of Cartesian vector components is smaller than that of vector components tangential to the Ewald sphere. Thus, the $\hat{k}$-space representations of three Cartesian vector components has been reported to be more memory efficient than that of two vector tangential components. Therefore for SE-MLFMM, where the Cartesian vector components have been formulated, $P = L/2 - 1$ may be opted [6]. Whereas in [6] the choice $P = 2$ is recommended, this value works well for LO basis functions. However, for HO basis functions, as can be revealed from (5.6), higher P-values are needed for comparable accuracies. The choice $P = \frac{L}{2}$ for even L and $P = \frac{L+1}{2}$ for odd L is a suggestion for sufficiently good accuracies. However, in cases when $L > 10$, the values $P > 5$ did not show significant improvements in the solution accuracies and hence for the present HO formulation $P \leq 5$ is recommended.

5.6 Numerical Results

In order to demonstrate the accuracy and efficiency of our implementation, several candidate problems are being presented in this section. Root mean square (RMS) error was used as a measuring tool for the comparison of accuracies of the solutions and is defined as

$$RMS = \sqrt{\frac{1}{N_r}\sum_{i=1}^{N_r} \left|\phi_R - \phi_F\right|^2}\,, \tag{5.9}$$

where N_r is the total number of result values in a problem under consideration, ϕ_R represents the reference value obtained either from some available exact solution or otherwise computed with our code with sufficiently fine discretization of the object surface. ϕ_F is the result calculated with our code. The normalized residual error of the iterative solver was fixed to 10^{-4} for all examples, unless stated otherwise. Flexible generalized minimal residual solver was used for the iterative solution of the MoM matrix. All computations, unless otherwise mentioned, were carried out on an AMD Opteron(tm) Processor 854 with 2.8 GHz central processing unit and total available memory of 32 GB.

5.6.1 PEC Sphere

In the first example, we carried out computations of the bistatic radar cross section (Bi-RCS) of a perfectly electrically conducting sphere of diameter 1 m at various frequencies for an x-polarized, z-directed incident plane wave. CFIE was used for these calculations. In a first attempt, the sphere was discretized with 53 822 triangular elements giving rise to 269 110 HO electric current unknowns. The Bi-RCS was computed at 11.8 GHz using six FMM levels. Near coupling matrix elements were computed using adaptive singularity cancellation technique. The spherical harmonics based expansion of the $\hat{k}$-space representation of the basis functions (see eq. (5.8)) was truncated at $P = 5$ during the initialization step of MLFMM. The matrix setup time with basis-by-basis evaluation of the coupling integrals (3.35)-(3.42) was 1 838.2 sec and with scalar barycentric integral approach was 769.5 sec both computed on an AMD Athlon(tm) XP 2500+ 1.84 GHz and 2 GB of RAM, which demonstrates at least twice faster evaluation of the later over the former approach. Future examples are solved with the scalar barycentric integral approach. The RMS error computed with reference to the exact solution using Mie series was found to be 0.10 dB. The detailed memory and processor time requirements, computed on 2.8 GHz AMD Opteron, are summarized in Table 5.2 (see soln. no. 1) and the Bi-RCS in E-plane is plotted in Fig. 5.4.

Next the memory requirements of HO implementation based on SE-MLFMM are compared with those of point-based MLFMA. The interpolatory HO basis functions proposed by [32] are used in [37, 124]. On average there are 1.5, 5, and 10.5 unknowns per triangle for zeroth-, first-, and second-order basis functions respectively. Therefore, in terms of accuracy of the solution for a given number of unknowns, our HO formulation should be comparable to the first-order basis functions solution of [37, 124]. As reported in [124, Table III], the computation of Bi-RCS of a PEC cube having side length of 15λ requires 750 MB memory for 73 200 1st order basis functions. Whereas, the SE-MLFMM based HO implementation requires 374.3 MB memory using four FMM levels with 74 400 HO unknowns (Table 5.3, soln. no. 17).

In another example, a 73.4λ diameter PEC sphere was modeled with 201 232 and 772 598 triangular elements to get 1 006 160 HO and 1 158 897 LO basis functions respectively. The Bi-RCS was computed with seven-levels of SE-MLFMM in both cases and required computational resources are summarized in Table 5.2 (soln. nos. 10 and 11). Memory requirements for LO and HO are almost comparable. The difference in the matrix setup time for LO and HO is due to larger number of LO triangles in each FMM group. However, the iterative solver for HO becomes slowly converging, as expected. The RMS

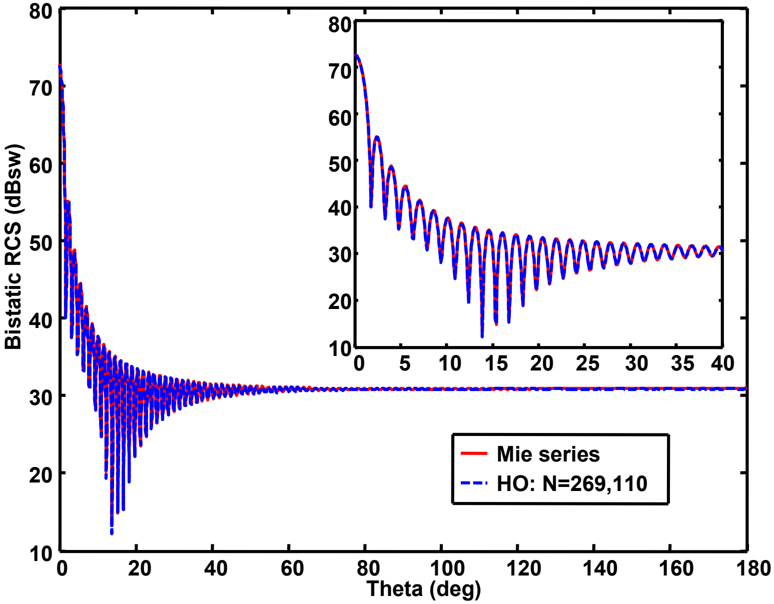

Fig. 5.4. Bistatic RCS of a 39.4λ diameter conducting sphere with an incident plane wave at f=11.8 GHz. A zoomed copy for 40° span is also placed at top right corner.

error was found to be 0.09 dB for HO solution and 0.43 dB for LO solution. Similarly, the RMS error for the Bi-RCS of 76.7λ was 0.09 dB and 0.46 dB for HO and LO solutions, respectively (Table 5.2, soln. nos. 12 and 13). Referring to soln. no. 5 of Table 5.2, computation of Bi-RCS of 76.7λ PEC sphere with 1 006 160 HO unknowns and seven-levels SE-MLFMM took about 3.26 GB memory.

The largest problem which we computed with SE-MLFMM based HO code was a sphere with 772 598 triangular elements and resulting 3 862 990 HO basis functions. Using this discretization the Bi-RCS was computed for 150λ, 166.8λ, 183.5λ, and 200λ diameter spheres with 54.6, 44.2, 36.5, and 30.7 number of HO basis functions per square wavelength. The RMS errors in dB with reference to the Mie series solution were found to be 0.11, 0.16, 0.23, and 0.42, respectively (Table 5.2, soln. nos. 6-9).

Table 5.2
Computation Time and Memory Requirements for the Calculations of Bi-RCS of a PEC Sphere for Plane Wave Incidence, Using CFIE with LO/HO Basis Functions.

Soln. no.	Ord.	Dia/λ	N	FMM levels	L	P	Near field memory (MB)	Matrix setup time (sec)	Solv. memory (MB)	Solv. time (sec)	Tot. time (sec)	RMS error (dB)
1	HO	39.4	269110	6	9	5	480.16	549.9	1000.13	3357.0	4247.8	0.10
2	HO	40	269110	5	12	6	998.88	528.1	1546.00	3535.0	4384.2	0.16
3	HO	50	269110	6	10	5	480.16	562.3	1089.58	4628.7	5687.3	0.26
4	HO	73.4	1006160	6	10	5	4214.66	2801.9	5852.62	13466.8	18150.1	0.09
5	HO	76.7	1006160	7	7	4	1676.54	2055.9	3262.71	13935.3	16964.7	0.11
6	HO	150	3862990	7	10	5	15519.98	10715.7	22473.29	64140.8	84103.9	0.11
7	HO	166.8	3862990	7	11	5	15519.98	10879.7	22917.82	71829.0	93810.2	0.16
8	HO	183.5	3862990	7	12	5	15519.98	10986.1	23526.42	86096.6	111462.3	0.23
9	HO	200	3862990	7	13	5	15519.98	11092.7	24125.82	94556.4	122719.4	0.42
10	HO	73.4	1006160	7	8	4	1676.54	2042.5	3305.46	18514.3	21760.3	0.09
11	LO	73.4	1158897	7	8	4	2251.36	7418.1	3885.74	7715.8	16652.7	0.43
12	HO	76.7	1006160	6	9	5	2791.44	2390.7	4489.20	14078.4	17816.9	0.09
13	LO	76.7	1158897	6	9	5	3716.02	9854.5	5452.51	8722.7	20345.8	0.46

TABLE 5.3
COMPUTATION TIME AND MEMORY REQUIREMENTS FOR VARIOUS PROBLEMS.

Problem	Soln. no.	Ord.	N	FMM levels	L	P	Near field memory (MB)	Matrix setup time (sec)	Solv. memory (MB)	Solv. time (sec)	Tot. time (sec)	RMS error (dB)	
												$\phi = 0°$ plane	$\phi = 90°$ plane
15λ Plate[a]	1	LO	172866	6	5	2	232.65	166.9	260.82	2287.2	2491.7	Ref	
	2	LO	67263	6	5	2	62.42	26.8	77.27	305.2	338.3	0.42	0.08
	3	LO	47703	5	6	3	44.27	48.3	55.38	256.1	325.1	0.77	0.09
	4	HO	11444	3	17	7	33.81	9.0	39.89	310.2	353.7	1.80	0.09
	5	HO	12260	5	10	5	7.78	5.8	21.88	686.7	705.6	1.11	0.08
	6	HO	12260	3	13	6	34.74	9.2	39.43	201.8	232.2	1.39	0.08
	7	HO	56130	5	10	5	112.14	32.6	129.91	839.6	925.9	0.25	0.06
Horn[a]	8	LO	18859	4	5	3	41.74	29.9	44.43	91.3	127.0	-	
	9	HO	6008	3	8	4	20.89	6.6	23.45	865.2	876.2	-	
Reflector[a]	10	LO	304478	8	4	2	233.49	345.1	318.15	3547.2	3991.2	-	
	11	HO	109014	6	8	4	291.12	92.2	365.49	7862.2	8056.9	-	
Box-plate[a]	12	LO	51626	5	5	2	72.10	72.5	81.67	444.7	531.6	Ref.	
	13	LO	11895	4	7	2	19.86	20.4	22.88	101.4	129.1	0.16	0.53
	14	HO	11830	4	6	3	11.23	7.9	16.57	432.3	445.9	0.06	0.19
	15	HO	11830	4	6	3	11.23	7.9	18.76	276.6	290.2	0.06	0.19
	16	HO	4410	3	9	3	5.50	3.7	8.39	100.4	108.6	0.27	0.50
15λ Cube[b]	17	HO	74400	4	12	6	244.65	156.7	374.27	330.3	654.8	-	

[a] Computed using EFIE. [b] Computed using CFIE.

5.6.2 Box-Plate Scatterer

An example of perfectly electrically conducting box-plate scatterer [125] was also solved with SE-MLFMM based HO implementation. The scatterer consists of a 2 m × 1 m × 0.3 m box and on it is a vertically oriented 1 m × 1 m plate. The Bi-RCS is computed for a z-directed x-polarized incident plane wave. Computational requirements are summarized in Table 5.3 (soln. nos. 12-16) and Bi-RCS is also plotted in Fig. 5.5. The Bi-RCS was obtained through the use of EFIE and normalized residual error of 10^{-3} using various numbers of the LO and HO basis functions for the entire domain. Using 11 830 HO unknowns and four FMM levels, the overall memory requirement was 16.57 MB which is comparable to the one reported in [125, Table I] for 1.5 order of basis functions. Using 3-level recursive preconditioner [122, 126] with 3, 5, and 8 search vectors respectively in the outer, inner and inner-most loops, the F-GMRES solver was converged to the desired accuracy in 37 restarts of the outer loop consuming 445.9 seconds for the complete solution. The experiment when performed on an AMD Athlon(tm) XP 2500+ 1.84 GHz and 2 GB of RAM, the total solution time was observed to be 1 014.3 seconds. However, as reported in [125], the restarted version of GMRES(30) algorithm took 9 201 iteration steps and 9 773 seconds for 11 614 unknowns of 1.5 order on a Pentium 4 with 2.9 GHz CPU and 1 GB of RAM. From the comparison of RMS errors in soln. nos. 13 and 14, it can again be reviewed that higher solution accuracies are achievable with HO basis functions than with equal number of LO basis functions except the drawback of slower convergence of the iterative solver. One possible solution for slower convergence is the use of more search vectors in the multilevel iterative solver. From Table 5.3 it can be seen from the soln. no. 15 which is just a replica of soln. no. 14 except that strong solver parameters (i.e. search vectors 8, 12, and 15 respectively in the outer, inner and inner-most loops) were incorporated and the complete solution time was reduced to 290.2 seconds but at the cost of slightly larger solution memory. The soln. no. 14 and 15 converged to the desired accuracy in 37 and 4 restarts, respectively.

5.6.3 PEC Plate

Another experiment was carried out for the computation of Bi-RCS of a PEC 15λ plate for grazing incidence of the incident plane wave. Memory and computational requirements are summarized in soln. nos. 1-7 of Table 5.3. Existence of the deep nulls in $\phi = 0^\circ$ plane, results in higher values of the RMS errors in this plane. From the soln. nos. 3 and 6 of Table 5.3, it can also be observed that about 55 HO basis functions per square wavelength produce accuracies

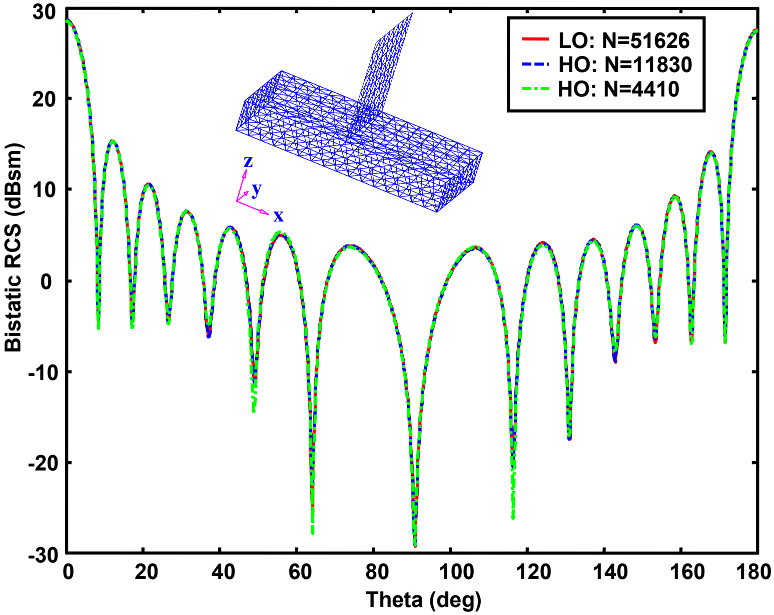

Fig. 5.5. Bistatic RCS of a box-plate scatterer at 1 GHz in $\phi = 0°$ plane.

comparable to that of 211 LO basis functions per square wavelength. Benefit in terms of the requirements of memory and computational time is also observable.

5.6.4 Thin Dielectric Coatings on a PEC Sphere

In order to elaborate the efficient treatment of material coating on metallic surfaces using IBC, the Bi-RCS of a PEC sphere of 1 m diameter coated with 0.25 cm thick dielectric ($\epsilon_r = 2.5 - \jmath 0.5$) was computed due to a 3 GHz linearly polarized incident plane wave. The computations were carried out with LO and HO basis representation and results are compared with the Mie series solution in Fig. 5.6. Reasonably accurate solution was obtained with much fewer HO unknowns than with LO unknowns. It can be seen that 38 660 HO unknowns produce results of similar accuracy as that with 176 472 LO unknowns. Further, if we compare the results of 40 530 LO and 38 660 HO unknowns in Fig. 5.6, the higher accuracy achieved with the HO unknowns than with almost similar number of LO unknowns is however, to some extent, evident. The HO solution with 38 660 unknowns was done in 272 s with 232 MB solver memory using three-level SE-MLFMM. On the other hand, 40 530 LO unknowns problem was solved in 485.7 s requiring 250.2 MB using three-level SE-MLFMM. In all cases 3, 4, and 4 search vectors were respectively used in the outer, inner and inner-most loops. The LO solution of 176 472 unknowns was obtained in 1 084.7 s, 630.8 MB while making use of 5-level SE-MLFMM. Efficient and relatively accurate MoM solution of surface integral equations with HO modeling of current densities, subject to IBC, is thus obvious.

5.6.5 Paraboloidal Reflector Antenna

Finally, an offset parabolic reflector antenna having diameter 21.89λ, offset height 4.13λ and focal length 20.65λ illuminated with a pyramidal feed horn operating at 6.175 GHz was modeled with LO and HO basis functions for the evaluation of far-field radiation pattern. The current distribution on the surfaces of horn and reflector antenna along with the radiation patterns are shown in Fig. 5.7. The computational data is summarized in soln. nos. 8-11 of Table 5.3.

5.6.6 Computational Performance with Diagonal and Symmetric Diagonal Preconditioner

As can be seen in above presented results for the comparison of LO and HO basis functions, although better accuracies have been obtained with HO as compared to LO, the solution times are often much larger for HO case. This makes the choice of HO relatively less favorable. A symmetric- (or square-root-) diagonal preconditioner has therefore been applied to enhance the computational efficiencies with HO discretizations. In this case, square-root of the diagonal preconditioner is used as both left- and right-preconditioner. Better performance has been observed with HO basis vectors.

The reflector model of section (5.6.5) has been chosen for this experiment. Computations were carried out on an Intel 2.83 GHz CPU, 16 GB RAM, with MS Windows XP-Pro x64 edition. The minimum size of FMM box was chosen twice the maximum edge length in both LO and HO modeling. During the iterative solution, 8, 10, and 18 search vectors respectively in the outer, inner, and inner-most preconditioner loops were used for all experiments. The degrees of multipole expansion on the finest level for LO and HO were 6 and 14. Based on this, the maximum number of spherical harmonics expansion terms in the series representation of the basis functions in an FMM group have been

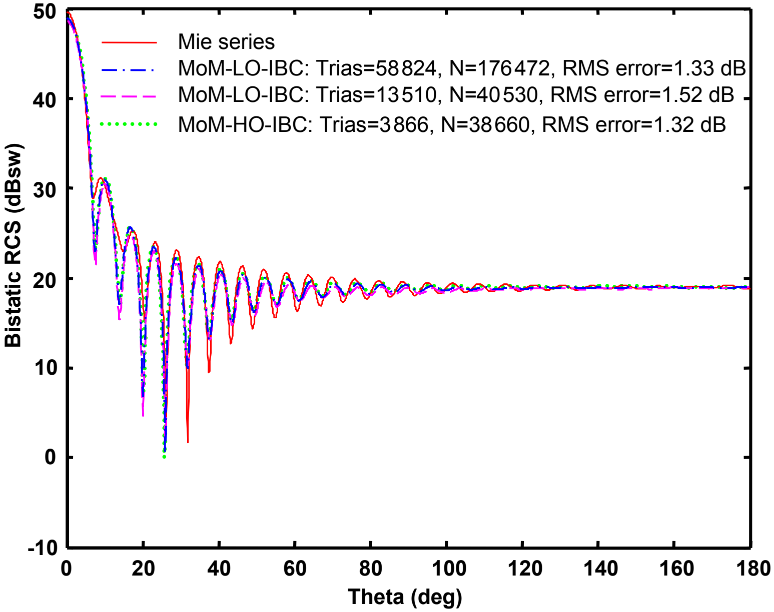

Fig. 5.6. Bistatic RCS in $\phi = 0^\circ$ plane of a dielectrically coated PEC sphere having 1 m diameter. Computations were carried out using LO and HO basis functions for an incident plane wave of 3 GHz and results are compared with Mie series solution.

chosen to be 3 and 5 respectively for LO and HO. The computation time and memory requirements are reported in Table 5.4. Obviously, the symmetric-diagonal preconditioner used for HO solutions gives about 30% improvement for HO and about 15% improvement for LO in the computation time for the flexible GMRES solver applied to the problem underconsideration. Unfortunately, the solution time for HO is still higher than the LO for approximately similar solution accuracies. This issue has to be addressed in future studies for further improvements in solution of integral equations with HO modeling of current densities.

5.6.7 Computational Performance with Mixed- and Complete-Order Basis Functions

As discussed in section 5.2, set of basis functions used in the MoM modeling of surface current densities for the solution of integral equations, may be mixed-order or complete-order bases. Here we compare the performance of these two types of basis formulations for the analysis of the reflector antenna of section (5.6.5). The complete-order basis formulation consists of LO (i.e. R^1 vectors of Table 5.1) plus the divergence-free functions (i.e. G^1 vectors of Table 5.1). With reference to Table 5.1, we call our basis formulation as LO, complete-order, and mixed-order if the set of functions R^1, $R^1 + G^1$, and $R^1 + G^1 + R^2$ are opted as the basis functions. A point to be noted is that the complete-order and mixed-order here means complete or mixed with respect to the basis space and not with respect to the curl or divergence of the basis space. A comparison of results with these three types of modeling options is summarized in Table 5.5. The computations are carried out with symmetric-diagonal preconditioner. Other parameters are similar to those reported in section 5.6.6. The far field radiation pattern in $\phi = 0°$ plane computed for the above mentioned three choice of basis functions is plotted in Fig. 5.7(b). From these results, it can be concluded that addition of divergence-free terms to the low order RWG makes the formulation more favorable (at least for the problem under-consideration) for a given accuracy of the solution.

TABLE 5.4
COMPARISON OF MOM BASED SOLUTIONS OF EFIE FOR REFLECTOR ANTENNA WITH DIAGONAL AND SYMMETRIC-DIAGONAL PRECONDITIONER.

Ord.	N	Base length	Precond.	FMM levels	Mem. (MB)	Time (sec)
LO	304478	$\lambda/14$	Diag.	6	1124	2703
LO	304478	$\lambda/14$	Sym. Diag.	6	1124	2293
HO	109014	$\lambda/5$	Diag.	5	982	5666
HO	109014	$\lambda/5$	Sym. Diag.	5	982	3919

TABLE 5.5
COMPARISON OF MOM BASED SOLUTIONS OF EFIE FOR REFLECTOR ANTENNA WITH LO, COMPLETE-ORDER AND MIXED-ORDER BASIS FUNCTIONS.

Type of bases	N	FMM levels	Mem. (MB)	Time (sec)	Res. error
LO: R^1	304478	6	1124	2293	1.70×10^{-5}
Complete: $R^1 + G^1$	65252	5	392	1135	1.06×10^{-6}
Mixed: $R^1 + G^1 + R^2$	109014	5	982	3919	3.50×10^{-5}

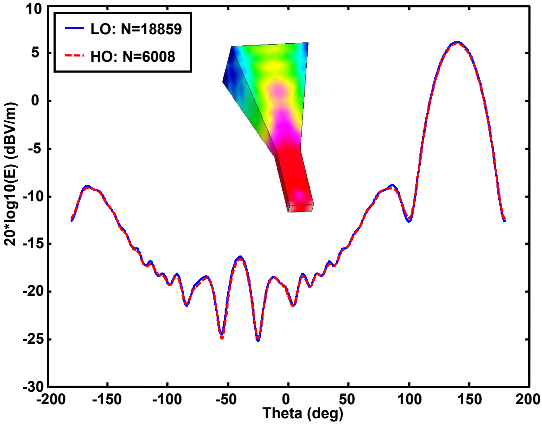

(a)

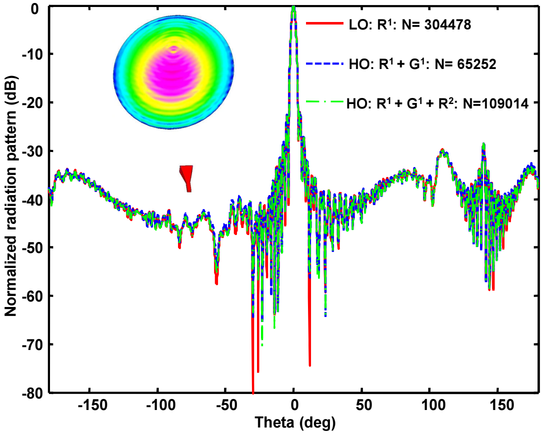

(b)

Fig. 5.7. Far field radiation patterns and electric current distribution on the surface of (a) pyramidal feed horn and (b) horn-fed parabolic reflector.

6 Inverse Equivalent Current Method

Radiation characteristics of an object under investigation are often desired from the knowledge of its near-field distribution. Inverse equivalent current method has been employed because of its versatile applicability to deal with arbitrary working domains and robust solution strategy where fast solvers are viable to gain memory and computation efficiencies. This treatment is based on an integral equation which relates the field intensities to their sources, usually the surface current densities. The Huygens equivalent surface currents have been investigated to account for the known near field characteristics of an object. Method of moments like solution may be sought for the governing integral equation. High efficiency has been achieved through the application of multilevel fast multipole method and better accuracy was possible with higher order modeling of current densities. This is presented in the sections to follow.

6.1 Integral Equation in Inverse ECM Formulation

In various applications of practical interest, for example antenna pattern measurements, tailor-made antenna synthesis etc., the investigation of the radiated fields or the equivalent electric/magnetic surface currents on the object surface from the knowledge of electric/magnetic near-field intensities defined on an arbitrary grid around the object under test is often desired. The aim of this task is to determine surface current sources such that their radiated fields best fit with the field strengths given at certain grid of sample points. Out of various techniques available in the literature, the inverse equivalent current methods e.g. [40, 41] etc. are most attractive because of their diverse applicability and robustness in the solution accuracies.

According to Huygens' principle, an arbitrarily shaped radiating or scattering object may be characterized by equivalent electric and magnetic current densities defined on a closed surface S_o around/on the object. In the inverse ECM, aim is to synthesize the equivalent current sources on such arbitrary Huygens surface from the knowledge of field strength. In order to investigate such problem, the radiated or scattered electric and magnetic fields $\boldsymbol{E}(\boldsymbol{r})$, $\boldsymbol{H}(\boldsymbol{r})$ defined on arbitrary observation point $\boldsymbol{r}$ may be related to the equivalent electric and magnetic surface current densities $\boldsymbol{J}_s(\boldsymbol{r}')$, $\boldsymbol{M}_s(\boldsymbol{r}')$ defined at $\boldsymbol{r}' \in S_o$, through the integral equations [40,41]

$$\boldsymbol{E}(\boldsymbol{r}) = \iint\limits_{S_o} \Big[\bar{\boldsymbol{G}}_J^E(\boldsymbol{r},\boldsymbol{r'}) \cdot \boldsymbol{J}_A(\boldsymbol{r'}) + \bar{\boldsymbol{G}}_M^E(\boldsymbol{r},\boldsymbol{r'}) \cdot \boldsymbol{M}_A(\boldsymbol{r'})\Big]\, ds' + \boldsymbol{E}^{inc}(\boldsymbol{r})\,, \quad (6.1)$$

$$\boldsymbol{H}(\boldsymbol{r}) = \iint\limits_{S_o} \Big[\bar{\boldsymbol{G}}_J^H(\boldsymbol{r},\boldsymbol{r'}) \cdot \boldsymbol{J}_A(\boldsymbol{r'}) + \bar{\boldsymbol{G}}_M^H(\boldsymbol{r},\boldsymbol{r'}) \cdot \boldsymbol{M}_A(\boldsymbol{r'})\Big]\, ds' + \boldsymbol{H}^{inc}(\boldsymbol{r})\,, \quad (6.2)$$

where $\bar{\boldsymbol{G}}_J^E$ and $\bar{\boldsymbol{G}}_M^E$ are the electric type dyadic Green's functions for the electric and magnetic currents respectively and similarly $\bar{\boldsymbol{G}}_J^H$ and $\bar{\boldsymbol{G}}_M^H$ represent the magnetic type dyadic Green's functions associated with the electric and magnetic currents. $\boldsymbol{E}^{inc}(\boldsymbol{r})$ and $\boldsymbol{H}^{inc}(\boldsymbol{r})$ are respectively the incident electric and magnetic fields. Integral equation (6.1) may be solved if electric field samples are available, whereas (6.2) can be considered if one is interested in magnetic field samples. The minimum number of field samples sufficient for good accuracy are dependent on the electrical size of the Huygens surface opted as the domain of current sources and may be computed by the criterion presented in [39]. The ECM formulation presented here assumes that the electric field samples are known and hence only (6.1) will be considered in the following sections.

6.2 MoM-Like Solution Strategy

Method of moments like procedure may be adapted in the solution of the integral equation (6.1), in which case the unknown inverse equivalent currents may be expanded using a set of expansion functions as

$$\boldsymbol{J}_s = \sum_{n=1}^{N_I} J_n \boldsymbol{f}_n\,, \qquad \boldsymbol{M}_s = \sum_{n=1}^{N_M} M_n \boldsymbol{f}_n\,, \quad (6.3)$$

where J_n and M_n are the unknown expansion coefficients. $N = N_I + N_M$ is the total number of unknowns. $\boldsymbol{f}_n$ represents a set of basis functions which may be low-order or higher-order.

In solving (6.1), recently low-order Rao-Wilton-Glisson functions have been employed for triangular domains in the discretization of unknown surface current densities [40]. Efficient solutions of surface integral equations in radiation and/or scattering problems of electromagnetics are possible with higher-order expansion functions as discussed in Chapter 5. With this motivation, hierarchical nearly-orthogonal higher-order expansion functions (see Chapter 5) have been utilized for the discretization of inverse equivalent currents on the planar triangular domains [127].

The discretized version of the integral equation (6.1) may be transformed to a system of linear equations when tested at each field sample resulting in matrix equation

$$[Z]\{I\} = \{E\} \ . \tag{6.4}$$

As described in [40], the present formulation is implemented in such a way that each angular component, i.e. E_θ and E_ϕ, of the field intensity gives one constraint equation. Hence, the total number (say M) of constraint equations in a problem is twice the number of field observation points. Contrary to the usual MoM solution of integral equations, the impedance matrix $[Z]$ encountered in ECM is non-square (i.e. $N \neq M$) in addition to being ill-conditioned. Consequently M linear equations have to be solved for N current unknowns. Therefore, the matrix system is solved in a least mean square (LMS) sense

$$[Z]^{\mathrm{adj}}\left([Z]\{I\} = \{E\}\right) \ , \tag{6.5}$$

where $[Z]^{\mathrm{adj}}$ is the adjoint matrix corresponding to the impedance matrix $[Z]$. Spherical harmonics based MLFMM [6,128] has been utilized to speed-up the overall computation of the ECM. In the present treatment of ECM formulation, observation points are chosen sufficiently apart from the source domain such that field contributions are always computed according to the SE-MLFMM. The generalized minimal residual solver has been utilized for the solution of normal equation (6.5). In the present work, the iterative solver is stopped at

$$\left|[Z]^{\mathrm{adj}}\left([Z]\{I\} - \{E\}\right)\right| \leq 10^{-d_a} \ , \tag{6.6}$$

where d_a represents the number of digits of accuracy and in the present course of study our choice is $d_a = 4$. The near-field residual error [40]

$$\epsilon_{\mathrm{NF}} = \frac{\left([Z]\{I\} - \{E\}\right)^{\mathrm{adj}}\left([Z]\{I\} - \{E\}\right)}{\{E\}^{\mathrm{adj}}\{E\}} \tag{6.7}$$

have been considered which is a representative of the mapping between the near-field samples $\boldsymbol{E}$ and ECM currents $\boldsymbol{J}_s$ as governed by (6.1). The smaller the ϵ_{NF}, the better the solution.

6.3 Numerical Results

A comparison of inverse ECM with LO and HO current modeling is presented through various numerical experiments. Number of field samples in all examples is chosen according to the criterion laid down in [39]. In order to demonstrate the relatively higher accuracies in the solutions of HO based ECM than with those of LO, the radiation patterns in the principle planes due to the ECM currents as well as NF errors (6.7) have been compared. All experiments have been carried out on an Intel 2.83 GHz CPU, 16 GB RAM, with MS Windows XP-Pro x64 edition.

In first experiment, electric field samples on a sphere with radius 2.7 m have been computed at 12 GHz with MoM due to a small dipole (1 cm × 4 cm) excited with a δ-gap voltage source at its center. From these field samples, inverse currents are computed at the same frequency with LO and HO based ECM on the surface of the dipole. The surface of the antenna is considered as the Huygens surface. In order to investigate the solution accuracies with LO and HO basis functions, in this example a surface triangular model with about 1.8 subdivisions per wavelength is considered for the ECM solution. From the inverse ECM currents obtained with both LO and HO basis functions, the relative radiation patterns in horizontal plane ($\phi = 0^\circ$) are computed and compared in Fig. 6.1. The HO based ECM currents produced radiation patterns which show good agreement with the reference MoM results. However, as can be seen, LO based ECM results vary significantly from the reference MoM results. Furthermore, the relative NF errors due to LO and HO basis functions were found to be 0.306 and 0.0876 respectively. This explains better accuracies obtained in ECM solutions with HO than with LO basis functions.

In second example, inverse ECM currents on a 20λ PEC plate are investigated. The surface of the PEC plate is considered as the Huygens surface. Firstly, the scattered electric fields on a spherical grid of 11 536 samples due to a plane wave incident on the plate at grazing angle have been computed employing MoM solution of integral equations with sufficiently finer triangular discretization of the plate. From the field samples, the inverse ECM currents are computed on the plate with LO and HO basis functions using about 1.4 subdivisions per wavelength. Identical FMM parameters (e.g. size of FMM box at finest level, number of multipoles and integration samples) and the solver parameters (e.g. search vectors, residual error) in accordance with well-known criterion have been used in both LO and HO based ECM solution. For the solution of 2 727 LO unknowns and 9 170 HO unknowns, the ECM solver converged to less than 10^{-4} residual error in 6 748 sec and 1 180 sec, respectively, for LO and HO basis functions. The memory requirements for LO and HO were 265 MB and 272 MB, respectively. The Bistatic RCS in horizontal and vertical planes have been computed from the inverse currents and are plotted in Fig. 6.2. HO results show better agreement than those of LO when compared with the reference MoM solution. Furthermore, the relative NF errors due to LO and HO basis functions have been found to be 0.319 and 0.024 respectively.

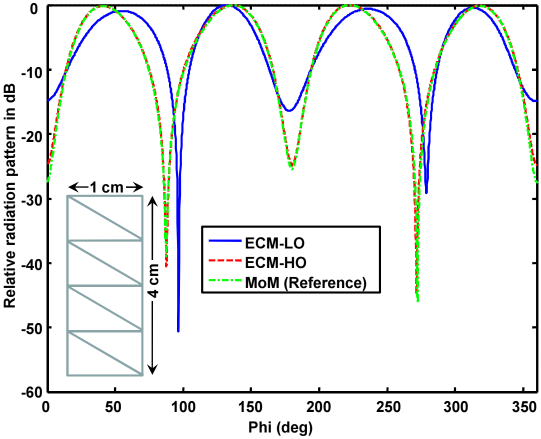

Fig. 6.1. Normalized radiation pattern of a dipole in $\phi = 0°$ plane at 12 GHz from LO and HO ECM currents using 4 186 field samples on a sphere with radius 2.7 m. A triangular surface mesh with about 1.8 subdivisions per wavelength has been used in the ECM model.

In another example, various Huygens surfaces are considered in ECM solutions with LO and HO surface current modeling. Firstly, MoM based computations of the near field samples are carried out due to a horn antenna at 6.175 GHz on a sphere around the horn and having radius of 2 m (far field distance ≈ 3 m) and 2° steps in ϕ and θ directions. From these near field samples, ECM currents have been computed over three different Huygens surfaces, namely the horn itself, a sphere and a box both circumscribing the original horn. In each case, suitable discretization of the Huygens surface is used such that the resulting NF errors ϵ_{NF} for LO and HO are of comparable magnitude. Furthermore, in the ECM solution, the side length of FMM group at the finest level was chosen equal to twice the maximum edge length of the triangular domains in both LO and HO cases. In Table 6.1 comparison of LO and HO computational performance is presented for three Huygens surfaces. As can be seen, the overall computation time for HO, in most cases, is significantly less than that of LO. The corresponding far field plots in horizontal plane are shown in Fig. 6.3. From the results presented in Table 6.1, it can be observed that for HO current modeling fewer number of large sized triangles are sufficient to obtain a solution comparable to LO modeling. Depending on the actual setup, the Huygens surface, the solver parameters etc. HO modeling is able to reduce the computation time for ECM solutions.

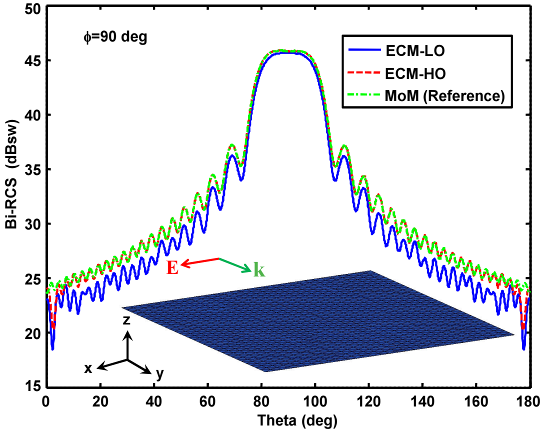

Fig. 6.2. Bistatic RCS in vertical plane ($\phi = 90°$) of a PEC plate with side length 20λ due to LO and HO inverse currents on the surface of plate computed with a plane wave at grazing incidence using 11 536 field samples on a sphere with radius 20 m. ECM model for both LO and HO basis functions works with triangular surface mesh having 1.4 subdivisions per wavelength.

TABLE 6.1
COMPARISON OF ECM-LO AND ECM-HO FOR DIFFERENT HUYGENS SURFACES.

	Mean edge length	No. of Triangles	Solution Time (Sec)	NF error ϵ_{NF}
Horn LO	$\lambda/16$	12 619	1 416	0.0044
Horn HO	$\lambda/10$	4 540	563	0.0064
Sphere LO	$\lambda/14$	60 850	6 332	0.0015
Sphere HO	$\lambda/7$	17 334	2 585	0.0013
Box LO	$\lambda/15$	26 656	810	0.0062
Box HO	$\lambda/8$	6 696	793	0.0061

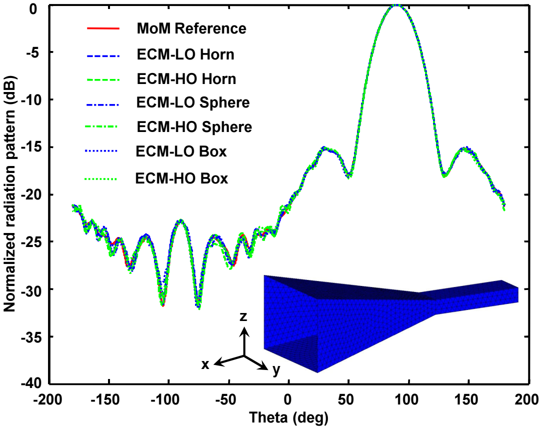

Fig. 6.3. Normalized radiation pattern of a horn antenna in horizontal plane ($\phi = 0°$) using LO and HO based ECM considering different Huygens surfaces.

7 Analysis of Space-Borne Reflector Antennas

For spacecraft applications the computation of radiation pattern of antennas is of significant importance. It is often desired to predict accurate radiation patterns not only in the main beam region but also in outer regions to avoid interference with other neighboring communication networks. Having developed efficient and accurate techniques for the analysis of electromagnetic problems, a few exemplary satellite antennas with and without the presence of satellite assembly are hereby considered for the prediction of their radiation performance.

7.1 Isolated Reflector Antennas

In this section it is assumed that the antennas under investigation are working in free space without any consideration of its surrounding objects. The method of moments based surface integral equation solver incorporating adaptive singularity cancellation technique [22–24, 104] and higher-order surface current modeling [117, 118] accelerated with spherical harmonics expansion based MLFMM [6] has been utilized for the analysis of two exemplary satellite antennas. Additionally the field computations are also carried out with a Jacobi-Bessel series expansion of physical optics radiation integral formulation [42, 129, 130] for comparison purposes.

In the first example a 1.06 m offset parabolic reflector with focal length 1 m and offset height 0.2 m operating at 6.175 GHz illuminated with a 11.2 cm × 8 cm aperture pyramidal feed horn is analyzed. In a Jacobi-Bessel series expansion of physical optics radiation integral formulation [42, 129, 130], the C and D matrices have been precomputed and stored in the memory and are used for the computation of radiation pattern in any (θ, ϕ) directions. In SE-MLFMM accelerated MoM-IE formulation, 65 252 complete-order $(R^1 + G^1)$ current basis functions have been solved making use of 5 FMM levels. The solution of the linear system of matrix equation has converged in about 1 135 s for a residual error of 1.06×10^{-6} while working on an Intel 2.83 GHz CPU, 16 GB RAM, with MS Windows XP-Pro x64 edition. Radiated fields are then determined from the knowledge of current distribution and making use of radiation inte-

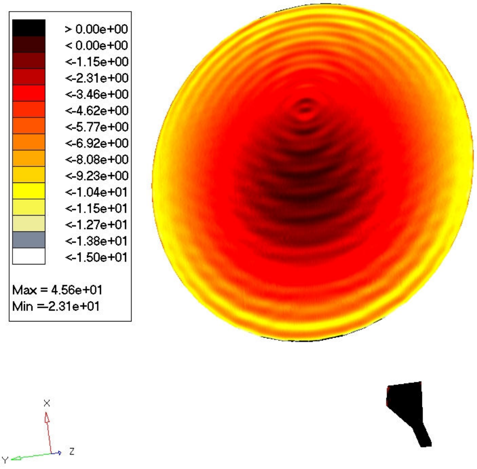

Fig. 7.1. Relative power distribution in dB on the surface of the 1.06 m offset reflector.

gral in negligible time.

The current distribution on the reflector surface is shown in Fig. 7.1, where the design parameter -10 dB edge illumination is visible. The far-field radiation pattern obtained with series-PO and MLFMM-MoM in H- and E-planes are compared in Fig. 7.2. It can be observed that PO and MoM patterns in both planes are very identical for main lobe and first few sidelobes. However, in far lobes PO results deviate from those of MoM. In E-plane away from ±20°, deviation of PO results from those of MoM are very pronounced.

In PO formulation, approximation of surface current density and edge discontinuities in currents on reflector are thought to be the reasons for such deviations. Also feed coupling effects have not been included in PO formulation reported in [129]. Although good agreement is observed between MLFMM-MoM and PO formulations in main lobe and first few side lobes, yet the fields in the region far from the main direction suffer from significant deviation. MLFMM accelerated MoM based solution of IEs is therefore recommended for better accuracies.

Furthermore, a full 3D radiation pattern for the 1.06 m reflector has been computed from the currents obtained with MLFMM-MoM solver. The pattern in the main and back directions is plotted in Fig. 7.3(a) and 7.3(b). In 7.3(c),

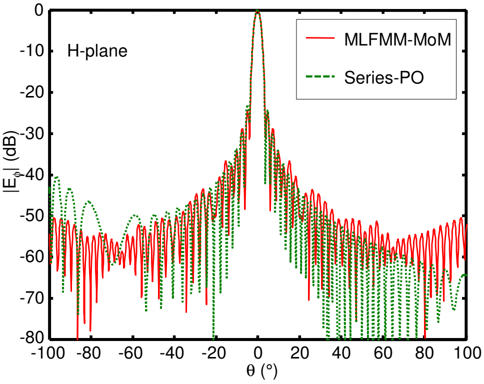

(a)

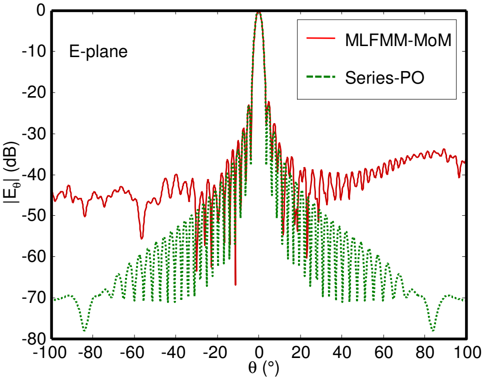

(b)

Fig. 7.2. Comparison of (a) H-plane and (b) E-plane radiation pattern plot for 1.06 m reflector.

main lobe and first few side lobes are again plotted for better visualization. The amplitudes and phases of the electric fields computed at the focal plane aperture of the reflector have also been plotted in Fig. 7.4.

In another problem an offset reflector with diameter of 1.5 m, focal length 1 m and offset height 0.2 m operating at 3.95 GHz, which is illuminated by a combined 3-sectoral feed horns each 14 cm × 2.9 cm aperture is analyzed with

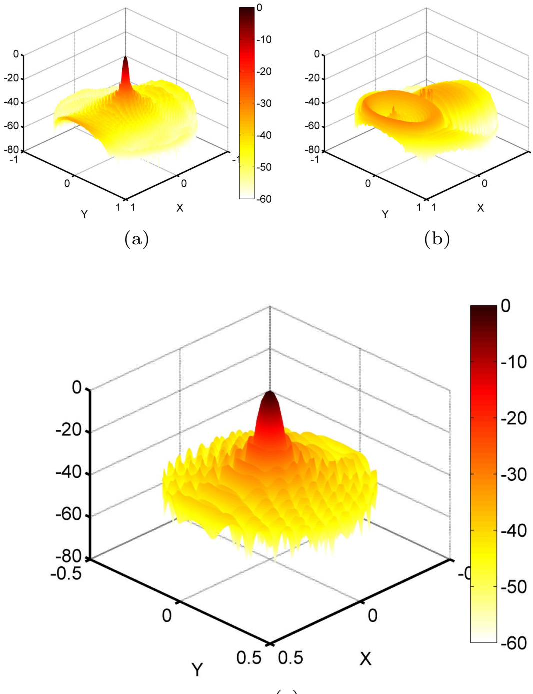

(a)

(b)

(c)

Fig. 7.3. Normalized 3D radiation pattern in dB for 1.06 m offset reflector in (a) forward direction, (b) backward direction and (c) surroundings of main lobe.

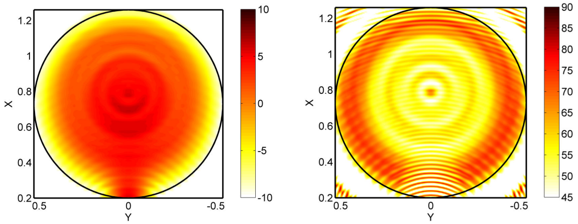

(a)

(b)

Fig. 7.4. Field distribution on the focal plane aperture of 1.06 m offset reflector: (a) Amplitude in dB and (b) phase in degrees of the electric field.

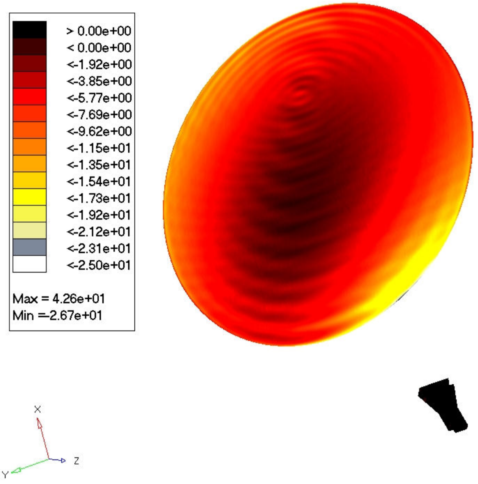

Fig. 7.5. Relative power distribution in dB on the surface of the 1.5 m 3-feed offset parabolic reflector.

MLFMM-MoM and series-PO. MLFMM-MoM formulation involved 165 302 LO unknowns. The system of matrix equation has been solved with 7 FMM levels obtaining a residual error of the order of 8.5×10^{-5}. It has been noted that because of the complex geometry of the three feed structure, the convergence was slower than the simple case of one feed horn. Also it is because the only option for open metallic objects is EFIE which suffers from poor convergence. The convergence can however, be made faster for residual error of the order of 10^{-3}, which produces acceptably good accuracies at least in the computations of radiated fields. The current distribution on the reflector surface is shown in Fig. 7.5. The resulting radiation patterns of PO and MoM are compared in Fig. 7.6. Although good agreement is observed in main lobe and first few side lobes, yet the fields in the region far from the main direction suffer from significant deviation. MLFMM accelerated MoM based solution of IEs is to be opted for better accuracies.

7.2 Reflector Antennas in Complex Environment

It is of importance to predict the antenna pattern distortions due to its surrounding satellite structure environment, which might lead to undesired radiation pattern resulting in a potential outage in the communication link. The

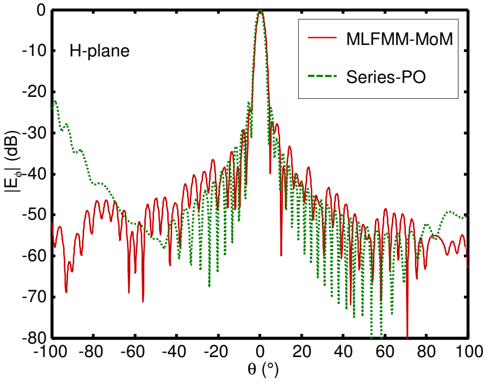

(a)

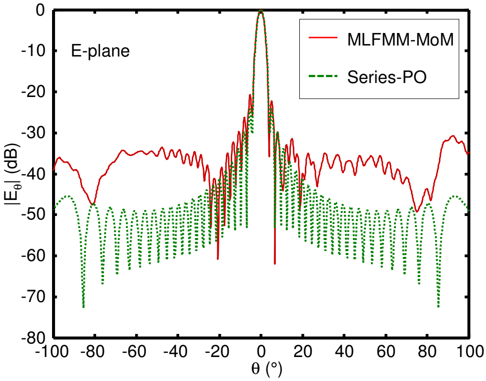

(b)

Fig. 7.6. Comparison of (a) H-plane and (b) E-plane radiation pattern plot for 1.5 m reflector excited with triple-feed horn assembly.

pattern distortions are dependent on several factors, mainly the location of the antenna with respect to the satellite platform, the shape of the satellite platform itself, the presence of obstacles and the influence of other antennas on the satellite.

In order to study the influence of complex structures in the neighborhood of an antenna under test, antenna radiation analysis has been carried out together

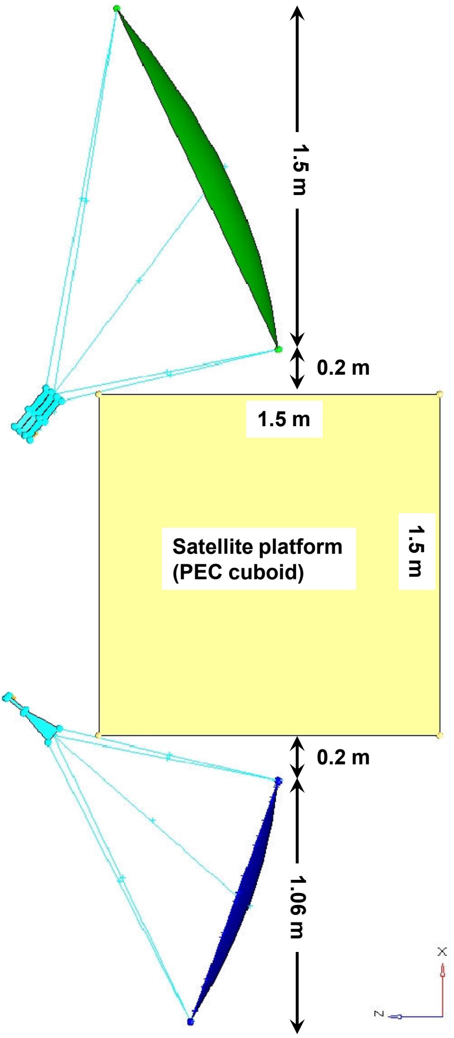

Fig. 7.7. Geometry of satellite assembly comprising of two reflector antennas mounted on a satellite platform. Supporting rods for reflector and feed horns are not considered.

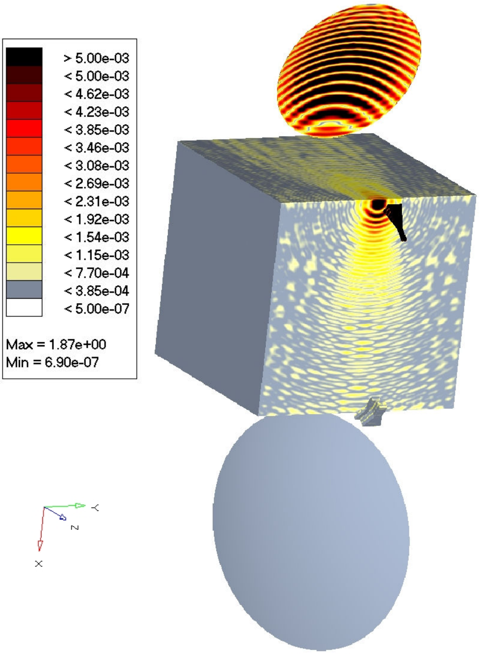

Fig. 7.8. Surface current distribution on linear scale due to excitation of 1.06 m reflector in the presence of a second reflector and satellite assembly.

with an exemplary satellite platform. As can be seen in Fig. 7.7, the structure under consideration is composed of a satellite platform of 1.5 m side length cuboid on which are the two reflectors mounted on opposite faces. Direction of main beam for each reflector is towards z-axis of the global coordinate system. In the present analysis, no supporting structure for the mounting of feeds or reflectors is taken into consideration. Each reflector-feed geometry is placed on the satellite platform such that visible zone of the reflector as viewed from the feed horn is unobstructed due to satellite platform edges and corners.

Now 1.06 m reflector is operating at 6.175 GHz and 1.5 m reflector at 3.95 GHz. At a time only one reflector is in operational mode for the radiation analysis with MLFMM-MoM solver. Firstly the 1.06 m reflector is excited and surface current distribution on the whole structure is computed as shown in Fig.

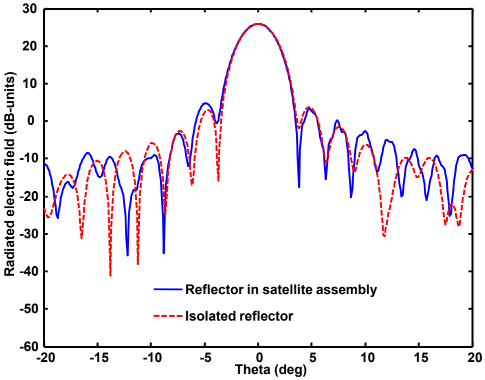

(a)

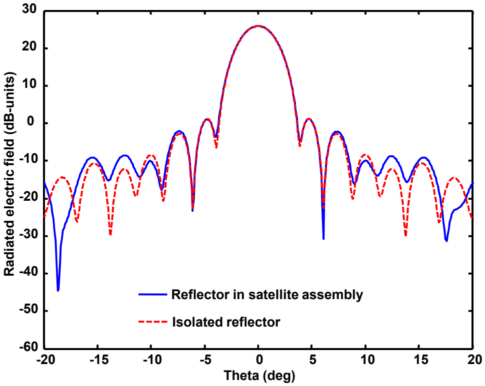

(b)

Fig. 7.9. Analysis of 1.06 m reflector in the presence of a 1.5 m reflector and satellite body: (a) radiated fields in $\phi = 0$ deg and (b) radiated fields in $\phi = 90$ deg.

7.8. Here real part of the complex surface current density is presented. The radiated field has been computed and compared in two principle planes with the isolated reflector as shown in Fig. 7.9. Similarly, in the next simulation 1.5 m reflector has been activated at it operating frequency of 3.95 GHz and the resulting surface currents and radiated fields are presented in Fig. 7.10 and Fig. 7.11. In the following paragraphs the importance of the analysis of reflector antennas in complex environment is discussed.

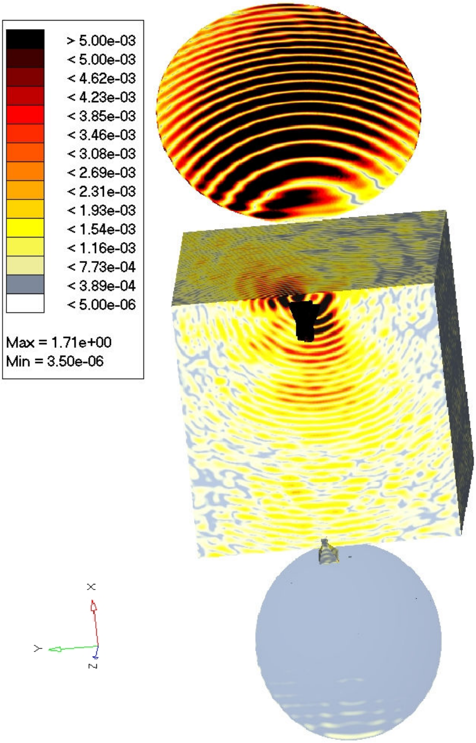

Fig. 7.10. Surface current distribution on linear scale due to excitation of 1.5 m reflector in the presence of a second reflector and satellite assembly.

Discussion:

From the results of analysis of satellite reflector antennas with and without

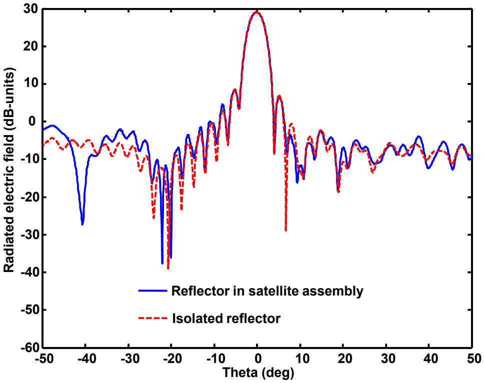

(a)

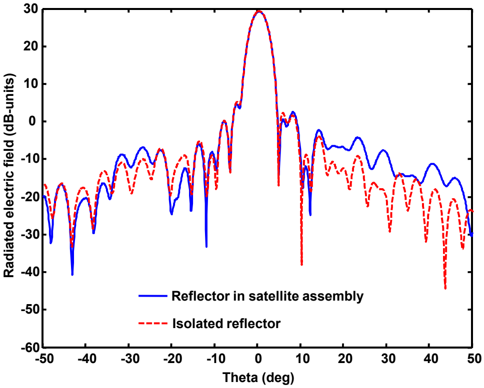

(b)

Fig. 7.11. Analysis of 1.5 m reflector in the presence of a 1.06 m reflector and satellite assembly: (a) radiated fields in $\phi = 0$ deg and (b) radiated fields in $\phi = 90$ deg.

the presence of neighboring structures, following remarks must be considered in the establishment of safe communication link.

1. In general it is observed that the surface current distribution and radiation patterns are influenced by many factors mainly the location of the antenna with respect to the satellite platform, the shape of the satellite platform itself, the presence of obstacles and the influence of other antennas on the satellite.

2. Antenna pattern distortions can be seen in Fig. 7.9 and Fig. 7.11 where diffractions from the surrounding satellite structure environment lead to significant variations up to 10 dB in the power levels in certain angular directions. For example, one might not want about 2 dB higher side lobe at $\theta \approx -5°$ in Fig. 7.9(a). Similarly, the null in the pattern at $\theta \approx \pm 17°$ might be unwanted.

3. From the surface currents shown in Fig. 7.8 and Fig. 7.10, the side lobes of the radiation pattern of the feed horn itself are assumed to be a cause of strong surface currents on the satellite body just near the excited feed horn. These current magnitudes cause radiations in unwanted directions. Furthermore, appropriate heat analysis might have to be carried out for any rise of temperature inside the satellite structure due to this unwanted current flow.

Therefore in conclusion it is of importance to accurately predict the antenna pattern distortions due to its surrounding satellite structure environment e.g. satellite body, supporting structure, other antennas etc., which might lead to unwanted side lobes, null pattern or a potential outage in the communication link. These pattern distortions are dependent on several factors, mainly the location of the antenna with respect to the satellite platform, the shape of the satellite platform itself, the presence of obstacles and the influence of other antennas on the satellite. The implemented SE-MLFMM accelerated MoM bases solution of IEs together with adaptive singularity treatment and higher order current discretization enables highly accurate and efficient analysis of such complex structures.

7.3 Surface Current Synthesis for Customized Radiation Pattern

Synthesis of antenna structures for customized radiation characteristics is often appreciated in radar systems and satellite communications. Customizations such as improvement in antenna gain or reduction of side lobe levels in certain directions etc., are typically obtained (e.g. [42–44]) with the aid of optimization algorithms (e.g. [45–49]). In the present work, as a preliminary effort, investigation has been made in the reconstruction of reflector surface currents for customized radiation pattern through the use of inverse equivalent current method.

7.3.1 Methodology

In the approach investigated here, following steps are considered for the synthesis of antenna surface currents for optimized/customized radiated fields.

1. MLFMM-MoM based computation of surface currents on the preliminarily designed antenna. From these currents, the electric fields are computed on a sphere in the far zone of the antenna under consideration.

2. The far zone electric field samples are scaled in the desired angular range. In present examples, the electric fields are customized such that the first few side lobes are further suppressed by a few dB of magnitude while keeping the main lobe power distribution un-altered.

3. These scaled electric fields are then mapped to inverse equivalent surface currents on reflector surface using ECM solver. Furthermore, the radiated fields are computed from these scaled ECM currents for the validity of the ECM solution.

4. Now these ECM currents are responsible for customized radiated fields. For the realization of these currents various techniques are reviewed which can be worked out in detail in future.

7.3.2 Examples

A focus-fed 1.06 m offset parabolic reflector has been selected for the purpose of this investigation. Initially the radiated fields of this reflector have been computed with MLFMM-MoM. For the validation of ECM solver, first these E-fields have been mapped to reconstruct the inverse equivalent surface currents on the reflector. These currents are shown in Fig. 7.12. Both currents are identical and it validates the ECM solver. Next, the MoM fields are scaled according to the needs of a certain application which states that the radiated fields in the angular region $4^\circ < |\theta| < 20^\circ$ be further suppressed by about 0.5-3 dB. Two separate simulations of ECM solver have been carried out which correspond to the 0.5 dB and 3 dB side lobe suppression in the given angular region. In the scaling process of electric fields, the phase of the fields is kept

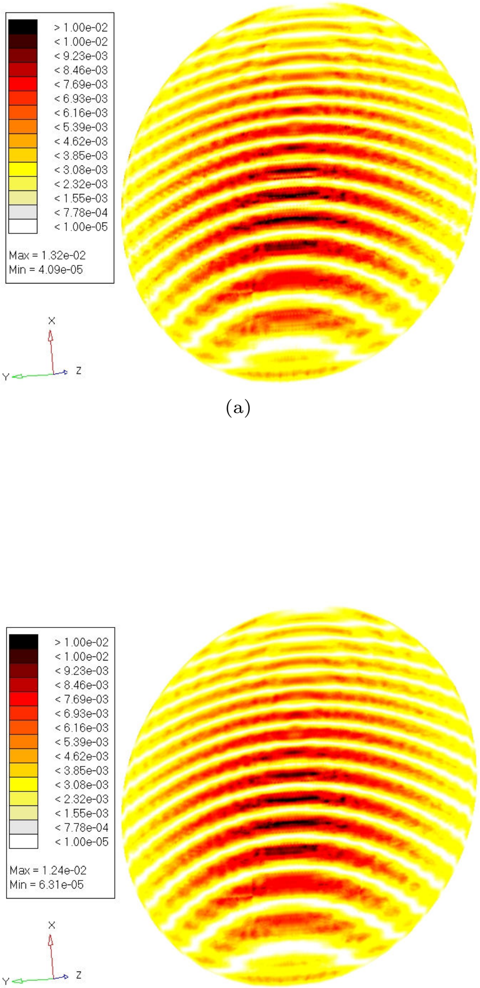

(b)

Fig. 7.12. Surface currents on the reflector antenna obtained for: (a) MoM-IE based analysis and (b) ECM based synthesis. The ECM currents in (b) have been obtained from the near field samples with 1° angular resolution in both θ and ϕ directions located on a sphere of radius 1000 km from the antenna.

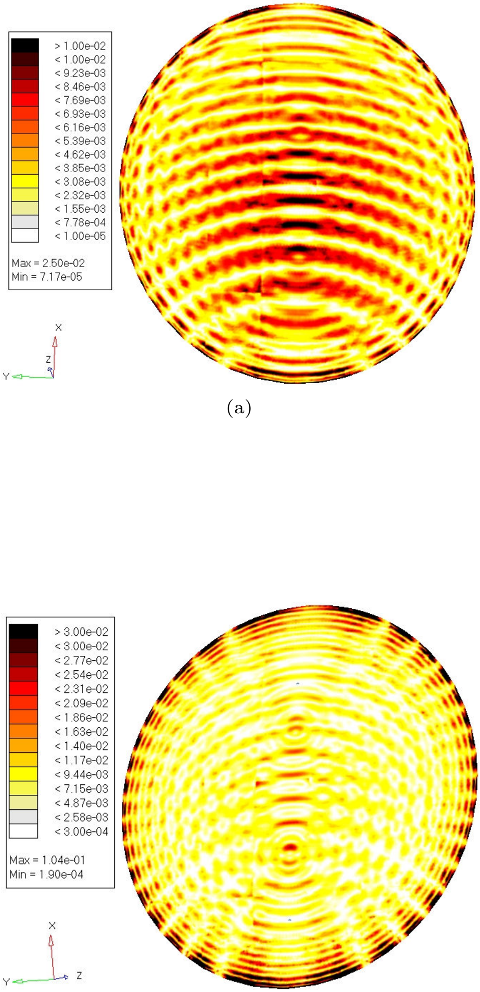

(a)

(b)

Fig. 7.13. Surface currents on the reflector antenna obtained with ECM solver for: (a) 0.5 dB side lobe suppression and (b) 3 dB side lobe suppression. Note the different scaling in (b).

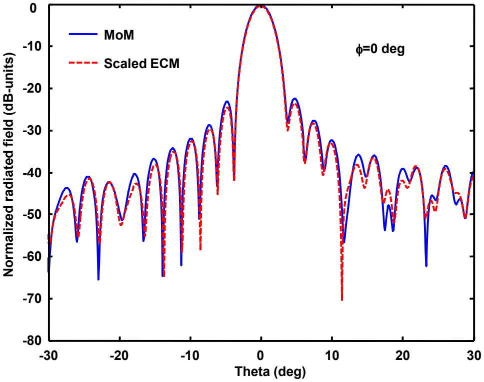

(a)

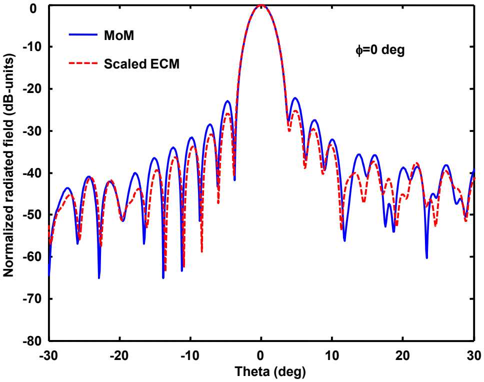

(b)

Fig. 7.14. Radiated fields obtained for: (a) scaled ECM surface currents of Fig. 7.13(a) with 0.5 dB suppression in first few side lobes and (b) scaled ECM surface currents of Fig. 7.13(b) with about 3 dB SLL suppression in first few side lobes.

unchanged whereas the amplitude is modified to fulfill the desired power level. These customized radiated fields have then been mapped to inverse equivalent surface currents on the surface of the reflector using the ECM solver.

The resulting surface currents corresponding to these customized fields for 0.5 dB and 3 dB SLL suppression are shown in Fig. 7.13. The computations of inverse currents of Fig. 7.13 were carried out with about 1 million HO unknowns for electric field samples distributed equally with 1° resolution in both θ and ϕ direction on a sphere of radius 1000 m centered at the origin of the reflector coordinate system. The radiated fields computed from the inverse ECM currents are shown in Fig. 7.14 where the desired suppression is achieved to a great extent. However, it is to be noted that in the present investigation, the reduction in SLL is achieved at the cost of higher power levels partially in other angular directions and partially in cross polarization while keeping the main lobe power distribution unchanged.

7.3.3 Realization Review and Guidelines Towards Future Work

For the realization of inverse ECM currents shown in Fig. 7.13, which result in customized radiation pattern presented in Fig. 7.14 a few possible approaches are discussed in the following paragraphs. However, this work is referred for future consideration.

Surface shaping with geometrical optics based ray path adjustment: As a preliminary effort, the amplitudes and the phases of the aperture fields due to MoM currents, inverse ECM corresponding to unscaled field strengths and inverse ECM obtained with customized (scaled) field pattern have been computed and presented in Fig. 7.15. Deviations in the amplitudes and phases of the fields due to scaled pattern from those of the MoM or unscaled fields are visible. It is expected that by compensating the phase differences through adjusting the corresponding path differences using geometrical optics, the desired suppression in side lobes might be achieved. The path difference might be compensated through the shaping of the reflector surface. Therefore, efforts will be made in shaping the surface of the paraboloidal such that unscaled ECM phase/amplitude coincides with those of the scaled ECM.

Feed pattern synthesis using subreflector: Another possibility might be to design the feed structure suitable for the realization of inverse ECM currents. One solution might be to insert a subreflector which can reshape the feed pattern $\boldsymbol{H}$ incident on the main reflector such that the physical optics equivalent current

$$\boldsymbol{J}_s = 2\hat{n} \times \boldsymbol{H} \,, \tag{7.1}$$

best fit the inverse ECM currents of Fig. 7.13, where $\hat{n}$ is unit surface normal. This configuration results in a Cassegrain or Gregorian reflector.

Use of dynamically adjustable resistive sheets: In [131] resistive sheets with electrically adjustable conductivity are used to adaptively place nulls in the radiation pattern of reflector antennas. These resistive screens are composed of thin polymer composites the resistance of which can be controlled via an electrical signal. Material such as polypyrroles and polyanilines exihibit variations in their conductivity between 10^{-7} and 10^{3} S/cm [131]. It is expected that the inverse ECM currents might be worked out through the adjustment of surface conductivity with the use of such resistive sheets at appropriate locations on the reflector surface.

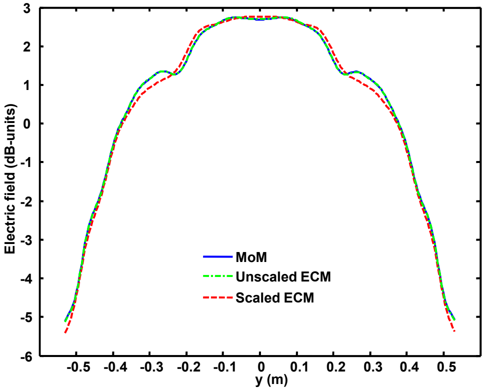

(a)

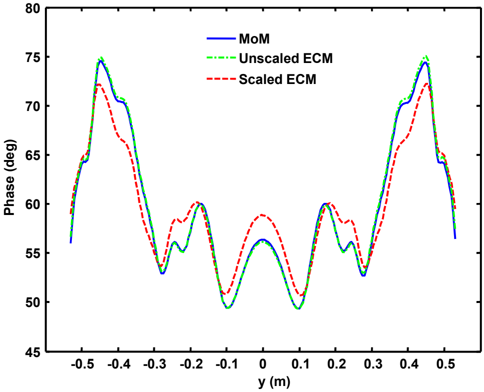

(b)

Fig. 7.15. Comparison of focal plane aperture field distribution computed at a horizontal cross-section of the reflector and obtained from the surface current distribution due to MoM (Fig. 7.12(a)), unscaled ECM (Fig. 7.12(b)), and with 3 dB SLL suppression (Fig. 7.13(b)). The amplitude of the electric field in dB is shown in (a) and its phase in degrees is given in (b).

Summary and Conclusion

The surface integral equation formulations have been considered for the efficient and accurate treatment of radiation and scattering problems of electromagnetics where the governing integral equations have been converted into a system of linear equations through method of moments employing Galerkin's approach with triangular hierarchical higher-order vector basis functions and adaptive treatment of singularities involved in the coupling integrals. The resulting system of linear equations have been solved using fast iterative solvers empowered with spherical harmonics expansion based MLFMM. The method has been proven to be an extremely powerful and versatile numerical technique for electromagnetic field simulation in antenna and scattering applications for arbitrarily shaped large structures.

The accuracy of MoM solutions of integral equations depends significantly on the calculation of the coupling integrals, which involve singular kernels. Quadrature rules are not directly applicable, especially for neighboring source and test domains, and special numerical treatment of such integrals is therefore necessary. Adaptive singularity cancellation technique has been proposed for the efficient, accurate and fully numerical treatment of the singular integrals. The *Arcsinh* transformation and the Radial Angular-R^2 transformation exactly cancel out the singularities of $\frac{1}{R}-$ and $\frac{\boldsymbol{R}}{R^3}-$type kernels where the time-consuming computations beyond the original source domains in case of near-singularities have been avoided through the use of adaptive versions of the above-mentioned techniques. Additionally, for given accuracies the dependence of the convergence on the height of observation point above the plane of source domain, which often demanded very large number of sample points especially for close proximities have been removed with the proposed adaptive singularity cancellation technique. Thus accurate computation of singular coupling integrals have been achieved with significantly fewer quadrature points independent of the heights of observation point above the plane of source domain resulting in higher computational efficiencies in the near-coupling evaluation.

Higher-order modeling of unknown source representation in the MoM formulations is essential in order to develop efficient algorithms for the computational electromagnetics. The widely used low order RWG basis functions in the expansion of unknown surface current densities suffer from the fundamental shortcoming that often dense geometrical discretization is necessary for sufficiently good accuracies. As a remedy hierarchical HO basis functions in the mixed order formulation have been implemented in the modeling of surface current densities and better accuracies with given number of unknowns compared with the LO counterparts have been achieved. Furthermore, sufficient reduction in the number of unknowns for a given problem and same accuracy has also been observed with HO modeling. The solution of large scale problems with integral equation formulations is hardly achievable without the proper use of fast solvers. Unfortunately the traditional MLFMM approaches become less efficient with HO due to their larger element dimensions. In contrast, the SE-MLFMM has been found considerably efficient in terms of memory and computation requirements even with HO current modeling, because of the efficient storage of the $\hat{k}$-space representations of the individual basis functions, and hence allows for very efficient iterative solution of the resulting equation system.

Thus the implemented SE-MLFMM accelerated MoM solution of integral equation formulation incorporating adaptive singularity cancellation technique and higher-order surface current modeling has been applied in the analysis of various applications of practical interest. Spacecraft reflector antennas have been studied in isolation as well as in complex environments. This enables the accurate predictions of radiation pattern and current flows on the neighboring structures. Furthermore, surface current shaping has been investigated through the use of inverse equivalent currents for customized radiation patterns. The realization of thus obtained surface currents has been postponed for future work for which a few propositions are made.

A Vector Theorems

A.1 Gauss's Divergence Theorem

$$\iiint\limits_V \nabla \cdot \boldsymbol{F} dv \ = \ \oiint\limits_S \boldsymbol{F} \cdot \hat{n} \, ds \tag{A.1}$$

A.2 First Scalar Green's Theorem

$$\iiint\limits_V \left[a\nabla^2 b + \nabla a \cdot \nabla b\right] dv \ = \ \oiint\limits_S a\frac{\partial b}{\partial n} \, ds \tag{A.2}$$

Proof: Substituting $\boldsymbol{F} = a\nabla b$ in Gauss's divergence theorem (equation (A.1)), we get

$$\iiint\limits_V \nabla \cdot (a\nabla b) \, dv \ = \ \oiint\limits_S (a\nabla b) \cdot \hat{n} \, ds \tag{A.3}$$

Using the vector identity

$$\nabla \cdot (f\boldsymbol{F}) = f \left(\nabla \cdot \boldsymbol{F}\right) + \boldsymbol{F} \left(\nabla f\right)$$

in eq. (A.3), we get

$$\iiint\limits_V \left[a\nabla^2 b + \nabla a \cdot \nabla b\right] dv \ = \ \oiint\limits_S a \left(\nabla b \cdot \hat{n}\right) \, ds$$

From the definition of gradient operator,

$$\nabla f \cdot \hat{n} \ = \ \frac{\partial f}{\partial n}$$

Hence the above equation reduces to first scalar Green's theorem i.e.

$$\iiint\limits_V \left[a\nabla^2 b + \nabla a \cdot \nabla b\right] dv \ = \ \oiint\limits_S a\frac{\partial b}{\partial n} \, ds$$

A.3 Second Scalar Green's Theorem

$$\iiint\limits_V \left[a\nabla^2 b - b\nabla^2 a\right] dv \;=\; \oiint\limits_S \left[a\frac{\partial b}{\partial n} - b\frac{\partial a}{\partial n}\right]\, ds \tag{A.4}$$

Proof: Substituting $\boldsymbol{F} = b\nabla a$ in Gauss's divergence theorem (equation (A.1)) and proceeding in similar way as in paragraph A.2, we come up with

$$\iiint\limits_V \left[b\nabla^2 a + \nabla a \cdot \nabla b\right] dv \;=\; \oiint\limits_S b\frac{\partial a}{\partial n}\, ds \tag{A.5}$$

Subtracting eq. (A.5) from eq. (A.2), we get the second scalar Green's theorem i.e.

$$\iiint\limits_V \left[a\nabla^2 b - b\nabla^2 a\right] dv \;=\; \oiint\limits_S \left[a\frac{\partial b}{\partial n} - b\frac{\partial a}{\partial n}\right]\, ds$$

A.4 First Vector Green's Theorem

$$\iiint\limits_V \left[(\nabla\times\boldsymbol{a})\cdot(\nabla\times\boldsymbol{b}) - \boldsymbol{a}\cdot(\nabla\times\nabla\times\boldsymbol{b})\right] dv$$

$$= \oiint\limits_S (\boldsymbol{a}\times\nabla\times\boldsymbol{b})\cdot\hat{n}\, ds \tag{A.6}$$

Proof: Substituting $\boldsymbol{F} = \boldsymbol{a}\times\nabla\times\boldsymbol{b}$ in Gauss's divergence theorem (equation (A.1)) we get

$$\iiint\limits_V \nabla\cdot(\boldsymbol{a}\times\nabla\times\boldsymbol{b})\, dv \;=\; \oiint\limits_S (\boldsymbol{a}\times\nabla\times\boldsymbol{b})\cdot\hat{n}\, ds \tag{A.7}$$

Using the vector identity

$$\nabla\cdot(\boldsymbol{F}\times\boldsymbol{G}) = (\nabla\times\boldsymbol{F})\cdot\boldsymbol{G} - \boldsymbol{F}\cdot\nabla\times\boldsymbol{G}$$

with $\boldsymbol{F} = \boldsymbol{a}$, $\boldsymbol{G} = \nabla\times\boldsymbol{b}$ on the LHS of eq. (A.7) we get first vector Green's theorem i.e.

$$\iiint\limits_V \left[(\nabla\times\boldsymbol{a})\cdot(\nabla\times\boldsymbol{b}) - \boldsymbol{a}\cdot(\nabla\times\nabla\times\boldsymbol{b})\right] dv \;=\; \oiint\limits_S (\boldsymbol{a}\times\nabla\times\boldsymbol{b})\cdot\hat{n}\, ds$$

A.5 Second Vector Green's Theorem

$$\iiint\limits_V \bigg[\boldsymbol{a}\cdot(\nabla\times\nabla\times\boldsymbol{b}) - \boldsymbol{b}\cdot(\nabla\times\nabla\times\boldsymbol{a})\bigg]dv$$

$$= -\oiint\limits_S \bigg[\boldsymbol{a}\times\nabla\times\boldsymbol{b} + (\nabla\times\boldsymbol{a})\times\boldsymbol{b}\bigg]\cdot\hat{n}\,ds \tag{A.8}$$

Proof: Switching the positions of $\boldsymbol{a}$ and $\boldsymbol{b}$ in eq. (A.6) we get

$$\iiint\limits_V [(\nabla\times\boldsymbol{a})\cdot(\nabla\times\boldsymbol{b}) - \boldsymbol{b}\cdot(\nabla\times\nabla\times\boldsymbol{a})]\,dv$$

$$= \oiint\limits_S (\boldsymbol{b}\times\nabla\times\boldsymbol{a})\cdot\hat{n}\,ds \tag{A.9}$$

Subtracting first vector Green's theorem (eq. (A.6)) from eq. (A.9) results in second vector Green's theorem i.e.

$$\iiint\limits_V \bigg[\boldsymbol{a}\cdot(\nabla\times\nabla\times\boldsymbol{b}) - \boldsymbol{b}\cdot(\nabla\times\nabla\times\boldsymbol{a})\bigg]dv$$

$$= -\oiint\limits_S \bigg[\boldsymbol{a}\times\nabla\times\boldsymbol{b} + (\nabla\times\boldsymbol{a})\times\boldsymbol{b}\bigg]\cdot\hat{n}\,ds$$

A.6 Scalar-Vector Green's Theorem

$$\iiint\limits_V \bigg[b\,(\nabla\times\nabla\times\boldsymbol{a}) + \boldsymbol{a}\nabla^2 b + (\nabla\cdot\boldsymbol{a})\,\nabla b\bigg]dv$$

$$= \oiint\limits_S \bigg[(\hat{n}\cdot\boldsymbol{a})\,\nabla b + (\hat{n}\times\boldsymbol{a})\times\nabla b + (\hat{n}\times\nabla\times\boldsymbol{a})\,b\bigg]\,ds \tag{A.10}$$

Proof: Let $\boldsymbol{a}$ and $\boldsymbol{b}$ be integrable vector functions in a volume V enclosed by a surface S. Consider following vector operations,

$$\begin{aligned}
\boldsymbol{b} &= b\hat{b} && \text{(A.11)}\\
\nabla\cdot\boldsymbol{b} &= \nabla b\cdot\hat{b} && \text{(A.12)}\\
\nabla^2\boldsymbol{b} &= \left(\nabla^2 b\right)\hat{b} && \text{(A.13)}\\
\nabla\times\boldsymbol{b} &= \nabla b\times\hat{b} && \text{(A.14)}
\end{aligned}$$

Note that the unit vector $\hat{b}$ is constant in a particular coordinate system in which the operator ∇ is defined.
Rewriting the first Curl-Curl operator appearing in Second Vector Green's Theorem:

$$\begin{aligned}
\boldsymbol{a}\cdot(\nabla\times\nabla\times\boldsymbol{b}) &= \boldsymbol{a}\cdot\left[\nabla\nabla\cdot\boldsymbol{b}-(\nabla\cdot\nabla)\,\boldsymbol{b}\right]\\
&= \boldsymbol{a}\cdot(\nabla\nabla\cdot\boldsymbol{b})-\boldsymbol{a}\cdot\nabla^2\boldsymbol{b} && \text{(A.15)}
\end{aligned}$$

From vector identities, we can write:

$$\begin{aligned}
\nabla\cdot(\boldsymbol{a}\nabla\cdot\boldsymbol{b}) &= (\nabla\cdot\boldsymbol{a})\,(\nabla\cdot\boldsymbol{b})+\boldsymbol{a}\cdot(\nabla\nabla\cdot\boldsymbol{b})\\
\Rightarrow\boldsymbol{a}\cdot(\nabla\nabla\cdot\boldsymbol{b}) &= \nabla\cdot(\boldsymbol{a}\nabla\cdot\boldsymbol{b})-(\nabla\cdot\boldsymbol{a})\,(\nabla\cdot\boldsymbol{b}) && \text{(A.16)}
\end{aligned}$$

Substituting (A.16) into (A.15) and making use of (A.11-A.13) we obtain:

$$\begin{aligned}
\boldsymbol{a}\cdot(\nabla\times\nabla\times\boldsymbol{b}) &= \nabla\cdot(\boldsymbol{a}\nabla\cdot\boldsymbol{b})-(\nabla\cdot\boldsymbol{a})\,(\nabla\cdot\boldsymbol{b})-\boldsymbol{a}\cdot\nabla^2\boldsymbol{b}\\
&= \nabla\cdot(\boldsymbol{a}\nabla\cdot\boldsymbol{b})-(\nabla\cdot\boldsymbol{a})\left(\nabla b\cdot\hat{b}\right)-\left(\boldsymbol{a}\nabla^2 b\right)\cdot\hat{b}\\
&= \nabla\cdot(\boldsymbol{a}\nabla\cdot\boldsymbol{b})-\left[(\nabla\cdot\boldsymbol{a})\,\nabla b+\left(\boldsymbol{a}\nabla^2 b\right)\right]\cdot\hat{b} && \text{(A.17)}
\end{aligned}$$

Also from Gauss's divergence theorem,

$$\begin{aligned}
\iiint\limits_V \nabla\cdot(\boldsymbol{a}\nabla\cdot\boldsymbol{b})\,dv &= \oiint\limits_S \hat{n}\cdot(\boldsymbol{a}\nabla\cdot\boldsymbol{b})\,ds\\
&= \oiint\limits_S (\hat{n}\cdot\boldsymbol{a})\,(\nabla b)\cdot\hat{b}\;ds && \text{(A.18)}
\end{aligned}$$

Taking volume integral of (A.17) over V and making use of (A.18) we get:

$$\iiint\limits_V \boldsymbol{a}\cdot(\nabla\times\nabla\times\boldsymbol{b})\,dv$$

$$= \iiint\limits_V \nabla \cdot (\boldsymbol{a} \nabla \cdot \boldsymbol{b})\, dv - \iiint\limits_V \Big[\boldsymbol{a} \nabla^2 b + (\nabla \cdot \boldsymbol{a}) \nabla b\Big] \cdot \hat{b}\ dv$$

$$= \oiint\limits_S (\hat{n} \cdot \boldsymbol{a}) (\nabla b) \cdot \hat{b}\ ds - \iiint\limits_V \Big[\boldsymbol{a} \nabla^2 b + (\nabla \cdot \boldsymbol{a}) \nabla b\Big] \cdot \hat{b}\ dv \qquad \text{(A.19)}$$

Utilizing the property of interchange of vector operations in the scalar triple product we can write the followings:

$$\begin{aligned} \hat{n} \cdot \boldsymbol{a} \times (\nabla \times \boldsymbol{b}) &= (\hat{n} \times \boldsymbol{a}) \cdot (\nabla \times \boldsymbol{b}) \\ &= (\hat{n} \times \boldsymbol{a}) \cdot \big(\nabla b \times \hat{b}\big) \\ &= (\hat{n} \times \boldsymbol{a}) \times \nabla b \cdot \hat{b} \qquad \text{(A.20)} \\ \hat{n} \cdot (\nabla \times \boldsymbol{a}) \times \boldsymbol{b} &= (\hat{n} \times \nabla \times \boldsymbol{a}) \cdot \boldsymbol{b} \\ &= (\hat{n} \times \nabla \times \boldsymbol{a})\, b \cdot \hat{b} \qquad \text{(A.21)} \end{aligned}$$

Substituting (A.11) and (A.19-A.21) in Second Vector Green's Theorem (equation (A.8)) we get:

$$\iiint\limits_V \Big[- b\, (\nabla \times \nabla \times \boldsymbol{a}) - \boldsymbol{a} \nabla^2 b + (\nabla \cdot \boldsymbol{a}) \nabla b\Big] \cdot \hat{b}\ dv$$

$$= - \oiint\limits_S (\hat{n} \cdot \boldsymbol{a}) (\nabla b) \cdot \hat{b}\ ds - \oiint\limits_S \Big[(\hat{n} \times \boldsymbol{a}) \times \nabla b + (\hat{n} \times \nabla \times \boldsymbol{a})\, b\Big] \cdot \hat{b}\ ds$$

$\Rightarrow$

$$\iiint\limits_V \Big[b\, (\nabla \times \nabla \times \boldsymbol{a}) + \boldsymbol{a} \nabla^2 b + (\nabla \cdot \boldsymbol{a}) \nabla b\Big] \cdot \hat{b}\ dv$$

$$= \oiint\limits_S \Big[(\hat{n} \cdot \boldsymbol{a}) (\nabla b) + (\hat{n} \times \boldsymbol{a}) \times \nabla b + (\hat{n} \times \nabla \times \boldsymbol{a})\, b\Big] \cdot \hat{b}\ ds \qquad \text{(A.22)}$$

Equation (A.22) is valid for arbitrary $\hat{b}$ and hence it is valid in general, i.e.

$$\iiint\limits_V \Big[b\, (\nabla \times \nabla \times \boldsymbol{a}) + \boldsymbol{a} \nabla^2 b + (\nabla \cdot \boldsymbol{a}) \nabla b\Big] dv$$

$$= \oiint\limits_S \Big[(\hat{n} \cdot \boldsymbol{a}) (\nabla b) + (\hat{n} \times \boldsymbol{a}) \times \nabla b + (\hat{n} \times \nabla \times \boldsymbol{a})\, b\Big] ds \qquad \text{(A.23)}$$

which is the desired Scalar-Vector Green's Theorem.

References

[1] G. Sarton and S. Gandz, "The invention of the decimal fractions and the application of the exponential calculus by Immanuel Bonfils of Tarascon (c. 1350)," *Isis*, vol. 25, no. 1, pp. 16–45, May 1936.

[2] D. E. Smith, *History of modern Mathematics*, 1906.

[3] S. Velamparambil, W. C. Chew, and J. Song, "10 million unknowns: Is it that big?" *IEEE Antennas Propag. Mag.*, vol. 45, no. 2, pp. 43–58, Apr. 2003.

[4] X. C. Wei and E. P. Li, "Fast solution for large scale electromagnetic scattering problems using wavelet transform and its precondition," *PIER*, vol. 38, pp. 253–267, 2002.

[5] W. C. Chew, J.-M. Jin, E. Michielssen, and J. Song, *Fast and Efficient Algorithms in Computational Electromagnetics.* Norwood, MA, USA: Artech House, Inc., 2001.

[6] T. F. Eibert, "A diagonalized multilevel fast multipole method with spherical harmonics expansion of the k-space integrals," *IEEE Trans. Antennas Propag.*, vol. 53, no. 2, pp. 814–817, Feb. 2005.

[7] J. Song, C.-C. Lu, and W. C. Chew, "Multilevel fast multipole algorithm for electromagnetic scattering by large complex objects," *IEEE Trans. Antennas Propag.*, vol. 45, no. 10, pp. 1488–1493, Oct. 1997.

[8] G. Manara, "Asymptotic methods in electromagnetics," *IEEE Antennas Propag. Mag.*, vol. 41, no. 5, pp. 83–84, Oct. 1999.

[9] R. Kouyoumjian, "Asymptotic high-frequency methods," *Proc. IEEE*, vol. 53, no. 8, pp. 864–876, Aug. 1965.

[10] W. Chew, L. Jiang, Y. Chu, M. Hastriter, and S. Velamparambil, "Recent advances in computational electromagnetics: from the very low frequency to ultra large scale problems," in *URSI EMTS*, 2004, pp. 736–738.

[11] W. C. Chew, M. S. Tong, and B. Hu, *Integral Equation Methods for Electromagnetic and Elastic Waves.* Morgan and Claypool Publishers, 2007.

[12] M. G. Duffy, “Quadrature over a pyramid or cube of integrands with a singularity,” *SIAM J. Numer. Anal.*, vol. 19, no. 6, pp. 1260–1262, Dec. 1982.

[13] D. R. Wilton, S. M. Rao, A. W. Glisson, D. H. Schaubert, O. M. Al-Bundak, and C. M. Butler, “Potential integrals for uniform and linear source distributions on polygonal and polyhedral domains,” *IEEE Trans. Antennas Propag.*, vol. 32, no. 3, pp. 276–281, Mar. 1984.

[14] S. Järvenpää, M. Taskinen, and P. P. Ylä-Oijala, “Singularity subtraction technique for high-order polynomial vector basis functions on planar triangles,” *IEEE Trans. Antennas Propag.*, vol. 54, no. 1, pp. 42–49, Jan. 2006.

[15] T. F. Eibert and V. Hansen, “Calculation of unbounded field problems in free space by a 3-D FEM/BEM-hybrid approach,” *J. Electromagn. Waves Appl.*, vol. 10, no. 1, pp. 61–78, Oct. 1996.

[16] T. F. Eibert and V. Hansen, “On the calculation of potential integrals for linear source distributions on triangular domains,” *IEEE Trans. Antennas Propag.*, vol. 43, no. 12, pp. 1499–1502, Dec. 1995.

[17] C. M. Butler, “Evaluation of potential integral at singularity of exact kernel in thin-wire calculations,” *IEEE Trans. Antennas Propag.*, vol. 23, no. 2, pp. 293–295, Mar. 1975.

[18] C. Huber, W. Rucker, R. Hoschek, and K. Richter, “A new method for the numerical calculation of cauchy principal value integrals in bem applied to electromagnetics,” *IEEE Trans. Magn.*, vol. 33, no. 2, pp. 1386–1389, Mar. 1997.

[19] C. J. Huber, W. Rieger, M. Haas, and W. M. Rucker, “The numerical treatment of singular integrals in boundary element calculations,” *ACES Journal*, vol. 12, no. 2, pp. 121–126, 1997.

[20] M. A. Khayat and D. R. Wilton, “Numerical evaluation of singular and near-singular potential integrals,” *IEEE Trans. Antennas Propag.*, vol. 53, no. 10, pp. 3180–3190, Oct. 2005.

[21] P. W. Fink, D. R. Wilton, and M. A. Khayat, “Issues and methods concerning the evaluation of hypersingular and near-hypersingular integrals in BEM formulations,” presented at the Intern. Conf. on Electromagnetics in Advanced Applications (ICEAA’05), Italy, Sept. 2005.

[22] Ismatullah and T. F. Eibert, “Adaptive singularity cancellation for efficient treatment of near-singular and near-hypersingular integrals in surface integral equation formulations,” *IEEE Trans. Antennas Propag.*, vol. 56, no. 1, pp. 274–278, Jan. 2008.

[23] Ismatullah and T. F. Eibert, “Adaptive singularity cancellation technique for near-singular and near-hypersingular integrals in surface integral equation formulations,” presented at the International URSI-Commission B Electromagnetic Theory Symposium (EMTS’07), Ottawa, Canada, July 26–28, 2007.

[24] Ismatullah and T. F. Eibert, “Near-singular and near-hypersingular surface integral evaluation by an adaptive singularity cancellation technique,” in *The Second European Conference on Antennas and Propagation (EuCAP’07)*, EICC, Edinburgh, UK, Nov. 11–16, 2007.

[25] J. Jin, *The Finite Element Method in Electromagnetics.* New York: John Wiley & Sons, Inc., 2002.

[26] B. M. Notaros, “Higher order frequency-domain computational electromagnetics,” *IEEE Trans. Antennas Propag.*, vol. 56, no. 8, pp. 2251–2276, Aug. 2008.

[27] E. Jørgensen, O. Kim, P. Meincke, and O. Breinbjerg, “Higher order hierarchical Legendre basis functions in integral equation formulations applied to complex electromagnetic problems,” *IEEE APS Intl. Symposium*, vol. 3A, pp. 64–67, July 2005.

[28] E. Jørgensen, J. L. Volakis, P. Meincke, and O. Breinbjerg, “Higher order hierarchical Legendre basis functions for electromagnetic modeling,” *IEEE Trans. Antennas Propag.*, vol. 52, no. 11, pp. 2985–2995, Nov. 2004.

[29] Y. Zhu and A. Cangellaris, *Multigrid Finite Element Methods for Electromagnetic Field Modeling.* Hoboken, New Jersey: John Wiley & Sons, Inc., 2006.

[30] D. K. Sun, J. F. Lee, and Z. Cendes, "Construction of nearly orthogonal Nedelec bases for rapid convergence with multilevel preconditioned solvers," *SIAM J. Sci. Comput.*, vol. 23, no. 4, pp. 1053–1076, 2001.

[31] J. C. Nédélec, "Mixed finite elements in R^3," *Numer. Math.*, vol. 35, no. 3, pp. 315–341, 1980.

[32] R. Graglia, D. Wilton, and A. Peterson, "Higher order interpolatory vector bases for computational electromagnetics," *IEEE Trans. Antennas Propag.*, vol. 45, no. 3, pp. 329–342, Mar. 1997.

[33] J. Webb, "Hierarchal vector basis functions of arbitrary order for triangular and tetrahedral finite elements," *IEEE Trans. Antennas Propag.*, vol. 47, no. 8, pp. 1244–1253, Aug. 1999.

[34] S. M. Rao, D. R. Wilton, and A. W. Glisson, "Electromagnetic scattering by surfaces of arbitrary shape," *IEEE Trans. Antennas Propag.*, vol. 30, no. 3, pp. 409–418, May 1982.

[35] B. Dembart and E. Yip, "The accuracy of fast multipole methods for maxwell's equations," *IEEE Comput. Sci. Eng.*, vol. 5, no. 3, pp. 48–56, 1998.

[36] S. Koc, J. Song, and W. C. Chew, "Error analysis for the numerical evaluation of the diagonal forms of the scalar spherical addition theorem," *SIAM J. Numer. Anal.*, vol. 36, no. 3, pp. 906–921, 1999.

[37] K. Donepudi, J. Song, J.-M. Jin, G. Kang, and W. Chew, "A novel implementation of multilevel fast multipole algorithm for higher order galerkin's method," *IEEE Trans. Antennas Propag.*, vol. 48, no. 8, pp. 1192–1197, Aug. 2000.

[38] T. Sarkar and A. Taaghol, "Near-field to near/far-field transformation for arbitrary near-field geometry utilizing an equivalent electric current and mom," *IEEE Trans. Antennas Propag.*, vol. 47, no. 3, pp. 566–573, Mar. 1999.

[39] A. Yaghjian, "An overview of near-field antenna measurements," *IEEE Trans. Antennas Propag.*, vol. 34, no. 1, pp. 30–45, Jan. 1986.

[40] T. F. Eibert and C. H. Schmidt, "Multilevel fast multipole accelerated inverse equivalent current method employing Rao-Wilton-Glisson discretization of electric and magnetic surface currents," *IEEE Trans. Antennas Propag.*, vol. 57, no. 4, pp. 1178–1185, Apr. 2009.

[41] Y. Alvarez, F. Las-Heras, and M. R. Pino, “Reconstruction of equivalent currentsdistribution over arbitrary three-dimensional surfaces based on integral equation algorithms,” *IEEE Trans. Antennas Propag.*, vol. 55, no. 12, pp. 3460–3468, Dec. 2007.

[42] Y. Rahmat-Samii and V. Galindo-Israel, “Shaped reflector antenna analysis using the Jacobi-Bessel series,” *IEEE Trans. Antennas Propag.*, vol. 28, no. 4, pp. 425–435, July 1980.

[43] O. Bucci, G. D’Elia, G. Mazzarella, and G. Panariello, “Antenna pattern synthesis: a new general approach,” *Proc. IEEE*, vol. 82, no. 3, pp. 358–371, Mar. 1994.

[44] F. Dubrovka, R. Dubrovka, O. Kim, V. Syrotyuk, and H. Khymych, “Synthesis of offset-fed Gregorian VSAT antennas,” in *Antenna Theory and Techniques, 2003. 4th International Conference on*, vol. 1, Sept. 2003, pp. 233–236.

[45] A. M. Wyant, “Genetic algorithm optimization applied to planar and wire antennas,” Master’s thesis, Department of Electrical Engineering, Kate Gleason College of Engineering, Rochester Institute of Technology, Rochester, New York, Aug. 2007.

[46] J. Johnson and V. Rahmat-Samii, “Genetic algorithms in engineering electromagnetics,” *IEEE Antennas Propag. Mag.*, vol. 39, no. 4, pp. 7–21, Aug. 1997.

[47] D. Gies and Y. Rahmat-Samii, “Particle swarm optimization (PSO) for reflector antenna shaping,” in *Antennas and Propagation Society International Symposium, 2004. IEEE*, vol. 3, June 2004, pp. 2289–2292.

[48] U. Diwekar, *Introduction to Applied Optimization.* Springer, 2008, vol. 22.

[49] T. Weise, *Global Optimization Algorithms: Theory and Application*, 2nd ed. FreeScience, 2009.

[50] O. Heaviside, “On electromagnetic waves, especially in relation to the vorticity of the impressed forces, and the forced vibration of electromagnetic systems,” *Philos. Mag.*, vol. 25, pp. 130–156, 1888.

[51] P. J. Nahin, “Oliver Heaviside,” vol. 262, no. 6, pp. 122–129, June 1990.

[52] S. J. Orfanidis, *Electromagnetic Waves and Antennas.* ECE Department, Rutgers University, New Jersey, 2008.

[53] J.-P. Bérenger, *Perfectly Matched Layer (PML) for Computational Electromagnetics (Synthesis Lectures on Computational Electromagnetics).* Morgan and Claypool Publishers, 2007.

[54] A. Sommerfeld, *Partial Differential Equations in Physics.* Academic Press, 1949.

[55] J.-M. Jin and D. J. Riley, *Finite Element Analysis of Antennas and Arrays.* Wiley-IEEE Press, 2008.

[56] K. F. Warnick, *Numerical Analysis for Electromagnetic Integral Equations.* Artech House Publishers, 2008.

[57] W. Wu, A. W. Glisson, and D. Kajfez, "A study of two numerical solution procedures for the electric field integral equation at low frequency," *Appl. Computational Electromagn. Soc. J.*, vol. 10, no. 3, pp. 69–80, 1995.

[58] T. Eibert, "Iterative-solver convergence for loop-star and loop-tree decompositions in method-of-moments solutions of the electric-field integral equation," *IEEE Antennas Propag. Mag.*, vol. 46, no. 3, pp. 80–85, June 2004.

[59] J. Mautz and R. Harrington, "An E-field solution for a conducting surface small or comparable to the wavelength," *IEEE Trans. Antennas Propag.*, vol. 32, no. 4, pp. 330–339, Apr. 1984.

[60] Y. Zhang, T. J. Cui, W. C. Chew, and J.-S. Zhao, "Magnetic field integral equation at very low frequencies," *IEEE Trans. Antennas Propag.*, vol. 51, no. 8, pp. 1864–1871, Aug. 2003.

[61] D. R. Wilton and A. W. Glisson, "On improving the electric field integral equation at low frequencies," in *URSI Radio Science Meeting Digest*, Los Angeles, CA, 1981, p. 24.

[62] R. Talhi, "Computational techniques and numerical analysis in e.m wave propagation and scattering : An overview and trends," in *Proc. EMTS 2007 - International URSI Commission B - Electromagnetic Theory Symposium*, Ottawa, ON, Canada, July 26-28 2007.

[63] A. Bondeson, T. Rylander, and P. Ingelström, *Computational Electromagnetics.* Springer, 2005.

[64] K. F. Warnick, “Computational electromagnetics,” Department of Electrical and Computer Engineering, Brigham Young University, Provo, UT, Tech. Rep., Sept. 2005.

[65] D. B. Davidson, *Computational Electromagnetics for RF and Microwave Engineering.* Cambridge University Press, 2005.

[66] A. F. Peterson, S. L. Ray, and R. Mittra, *Computational Methods for Electromagnetics.* New York: IEEE Press, 1998.

[67] A. Tzoulis, “Numerical modeling of electromagnetic problems with the hybrid finite element - boundary integral - multilevel fast multipole - uniform geometrical theory of diffraction method,” Ph.D. dissertation, Fachbereich Elektrotechnik und Informationstechnik der Technischen Universität Darmstadt, 2008.

[68] M. Kline, “An asymptotic solution of Maxwell’s equation,” *Commun. Pure Appl. Math.*, vol. 4, pp. 225–263, 1951.

[69] R. K. Luneberg, *Mathematical Theory of Optics.* Brown Univ. Press, Providence, RI., 1964.

[70] E. R. Pike and P. C. Sabatier, *Scattering: Scattering and Inverse scattering in Pure and Applied Science.* Academic Press, 2002, vol. 1.

[71] R. Bansal, *Engineering Electromagnetics: Applications.* CRC Press, 2006.

[72] W. L. Stutzman and G. A. Thiele, *Antenna Theory and Design.* John Wiley & Sons Inc, 1981.

[73] C. A. Balanis, *Advanced Engineering Electromagnetics.* Wiley, 1989.

[74] K. B. Wolf and G. Krotzsch, “Geometry and dynamics in refracting systems,” *Eur. J. Phys.*, vol. 16, no. 1, pp. 14–20, 1995.

[75] I. Gupta, C. Pistorius, and W. Burnside, “An efficient method to compute spurious end point contributions in PO solutions,” *IEEE Trans. Antennas Propag.*, vol. 35, no. 12, pp. 1426–1435, Dec. 1987.

[76] J. B. Keller, “Geometrical theory of diffraction,” *J. Opt. Soc. Am.*, vol. 52, no. 2, pp. 116–130, 1962.

[77] R. Kouyoumjian and P. Pathak, "A uniform geometrical theory of diffraction for an edge in a perfectly conducting surface," *Proc. IEEE*, vol. 62, no. 11, pp. 1448–1461, Nov. 1974.

[78] P. Y. Ufimtsev, "Method of edge waves in the physical theory of diffraction," *Izd-Vo Sov. Radio*, vol. V, pp. 1–243, 1962, [In Russian: translation prepared by the U.S. Air Force Foreign Technology Division, Wright Patterson AFB, Ohio; released for public distribution Sept. 7, 1971.].

[79] A. Taflove and S. C. Hagness, *Computational Electrodynamics: The Finite-Difference Time-Domain Method.* Artech House Publishers, 2000.

[80] K. Yee, "Numerical solution of initial boundary value problems involving Maxwell's equations in isotropic media," *IEEE Trans. Antennas Propag.*, vol. 14, no. 3, pp. 302–307, May 1966.

[81] R. Courant, K. Friedrichs, and H. Lewy, "Über die partiellen Differenzengleichungen der mathematischen Physik," *Mathematische Annalen*, vol. 100, no. 1, pp. 32–74, Dec. 1928.

[82] R. Courant, K. Friedrichs, and H. Lewy, "On the partial difference equations of mathematical physics," *IBM Journal*, pp. 215–234, Mar 1967, [English translation of [81].].

[83] J.-P. Berenger, "A perfectly matched layer for the absorption of electromagnetic waves," *J. Comput. Phys.*, vol. 114, no. 2, pp. 185–200, 1994.

[84] J. L. Volakis, A. Chatterjee, and L. C. Kempel, *Finite Element Method for Electromagnetics: Antennas, Microwave Circuits, and Scattering Applications.* Wiley-IEEE Press, 1998.

[85] J.-M. Jin and J. Volakis, "A finite-element-boundary integral formulation for scattering by three-dimensional cavity-backed apertures," *IEEE Trans. Antennas Propag.*, vol. 39, no. 1, pp. 97–104, Jan. 1991.

[86] T. F. Eibert, "Verknüpfung der Methode der Finiten Elemente mit einem Integralgleichungsverfahren für ebene geschichtete Strukturen," Ph.D. dissertation, Fachbereich Elektrotechnik der Bergischen Universität Wuppertal, 1997.

[87] R. F. Harrington, *Field Computation by Moment Methods.* New York: Wiley-IEEE Press, 1993.

[88] R. Harrington, "Origin and development of the method of moments for field computation," *IEEE Antennas Propag. Mag.*, vol. 32, no. 3, pp. 31–35, June 1990.

[89] C.-C. Lu and W. C. Chew, "The use of huygens' equivalence principle for solving 3-d volume integral equation of scattering," *IEEE Trans. Antennas Propag.*, vol. 43, no. 5, pp. 500–507, May 1995.

[90] R. A. Shore and A. D. Yaghjian, "Dual-surface integral equations in electromagnetic scattering," in *XXVIIth General Assembly of the International Union of Radio Science*, Maastricht, Netherlands, Aug. 17-24, 2002.

[91] R. Shore and A. Yaghjian, "Dual-surface integral equations in electromagnetic scattering," *IEEE Trans. Antennas Propag.*, vol. 53, no. 5, pp. 1706–1709, May 2005.

[92] T. B. A. Senior, "Impedance boundary conditions for imperfectly conducting surfaces," *Appl. Sci. Res. B*, vol. 8, no. 1, pp. 418–436, Dec. 1960.

[93] D. J. Hoppe and Y. Rahmat-Samii, *Impedance boundary conditions in electromagnetics.* Washington, DC: Taylor & Francis, 1995.

[94] V. Rokhlin, "Rapid solution of integral equations of classical potential theory," *J. Comput. Phys.*, vol. 60, no. 2, pp. 187 – 207, 1985.

[95] V. Rokhlin, "Rapid solution of integral equations of scattering theory in two dimensions," *J. Comput. Phys.*, vol. 86, no. 2, pp. 414 – 439, 1990.

[96] R. Coifman, V. Rokhlin, and S. Wandzura, "The fast multipole method for the wave equation: A pedestrian prescription," *IEEE Antennas Propag. Mag.*, vol. 35, no. 3, pp. 7–12, June 1993.

[97] J. Song, C. Lu, W. Chew, and S. Lee, "Fast illinois solver code (FISC)," *IEEE Antennas Propag. Mag.*, vol. 40, no. 3, pp. 27–34, June 1998.

[98] X.-Q. Sheng, J.-M. Jin, J. Song, C.-C. Lu, and W. C. Chew, "On the formulation of hybrid finite-element and boundary-integral methods for 3-d scattering," *IEEE Trans. Antennas Propag.*, vol. 46, no. 3, pp. 303–311, Mar. 1998.

[99] T. Eibert, "Modelling of integrated antenna - scatterer configurations by hybrid finite element - boundary integral - multilevel fast multipole methods," in *Progress in Electromagn. Research Symposium*, Pisa, 2004.

[100] M. Abramowitz and I. A. Stegun, *Handbook of Mathematical Functions: with Formulas, Graphs, and Mathematical Tables.* Dover Publications, 1968.

[101] V. Rokhlin, "Diagonal forms of translation operators for the Helmholtz equation in three dimensions," *Appl. Comput. Harmon. Anal.*, vol. 1, pp. 82–93, Dec. 1993.

[102] J. Rahola, "Diagonal forms of the translation operators in the fast multipole algorithm for scattering problems," *BIT Numerical Mathematics*, vol. 36, no. 2, pp. 333–358, June 1996.

[103] C. T. Tai, "Direct integration of field equations," *PIER*, vol. 28, pp. 339–359, 2000.

[104] Ismatullah, "Efficient numerical computation of near-singular and near hyper-singular potential integrals in MoM formulation," Master's thesis, Institut für Hochfrequenztechnik, Universität Stuttgart, 2007.

[105] P. Ylä-Oijala and M. Taskinen, "Calculation of CFIE impedance matrix elements with RWG and $\hat{n} \times$ RWG functions," *IEEE Trans. Antennas Propag.*, vol. 51, no. 8, pp. 1837–1846, Aug. 2003.

[106] J. Mautz and R. Harrington, "H-field, E-field, and combined-field solutions for conducting bodies of revolution," *Archiv für Elektronik und Übertragungstechnik (Electron. Commun.)*, vol. 32, pp. 157–164, 1978.

[107] M. A. Leontovich, "Investigation of propagation of radiowaves," Part II, Moscow, 1948.

[108] X. Q. Sheng, J. M. Jin, J. M. Song, W. C. Chew, and C. C. Lu, "Solution of combined-field integral equation using multilevel fast multipole algorithm for scattering by homogeneous bodies," *IEEE Trans. Antennas Propag.*, vol. 46, no. 11, pp. 1718 –1726, Nov. 1998.

[109] J. G. V. Bladel, *Electromagnetic Fields*, 2nd ed. Wiley-Interscience IEEE Press, 2007.

[110] L. Knockaert, "A general Gauss theorem for evaluating singular integrals over polyhedral domains," *Electromagnetics*, vol. 11, pp. 269–280, 1991.

[111] S. Järvenpää, M. Taskinen, and P. Ylä-Oijala, "Singularity extraction technique for integral equation methods with higher order basis functions on plane triangles and tetrahedra," *Int. J. Numer. Methods Eng.*, vol. 58, pp. 1149–1165, Aug. 2003.

[112] J. Eastwood and J. Morgan, "Higher-order basis functions for MoM calculations," *IEE Proc.: Sci. Meas. Technol.*, vol. 2, no. 6, pp. 379–386, Nov. 2008.

[113] D. Taylor, "Accurate and efficient numerical integration of weakly singular integrals in galerkin efie solutions," *IEEE Trans. Antennas Propag.*, vol. 51, no. 7, pp. 1630–1637, July 2003.

[114] S. Amini and N. D. Maines, "Regularization of strongly singular integrals in boundary integral equations," *Commun. Numer. Methods Eng.*, vol. 12, no. 11, pp. 787–793, 1996.

[115] Z. Huan-lin, N. Zhong-rong, and W. Xiu-xi, "Regularization of nearly singular integrals in the boundary element method of potential problems," *J. Appl. Math. Mech.*, vol. 24, no. 10, pp. 1208–1214, Oct. 2003.

[116] M. Khayat, D. Wilton, and P. Fink, "An improved transformation and optimized sampling scheme for the numerical evaluation of singular and near-singular potentials," in *IEEE Antennas and Propagation Society International Symposium*, June 2007, pp. 4845–4848.

[117] Ismatullah and T. F. Eibert, "Surface integral equation solutions by hierarchical vector basis functions and spherical harmonics based multilevel fast multipole method," *IEEE Trans. Antennas Propag.*, vol. 57, no. 7, pp. 2084–2093, July 2009.

[118] Ismatullah and T. F. Eibert, "Higher order surface integral equation solutions employing spherical harmonics based multilevel fast multipole method," in *IEEE AP-S / USNC-URSI Symposium*, North Charleston, South Carolina, USA, June 1–5, 2009.

[119] D. Davidson, "An evaluation of mixed-order versus full-order vector finite elements," *IEEE Trans. Antennas Propag.*, vol. 51, no. 9, pp. 2430–2441, Sept. 2003.

[120] Y. Saad, *Iterative Methods for Sparse Linear Systems*, 2nd, Ed., 2000.

[121] T. F. Eibert, "Advances in hybrid finite element - boundary integral modelling of three-dimensional radiation and scattering problems," in *Intern. ITG Conf. on Antennas*, Berlin, Sept. 2003, pp. 157–160.

[122] J. Liu and J.-M. Jin, "A highly effective preconditioner for solving the finite element-boundary integral matrix equation of 3-D scattering," *IEEE Trans. Antennas Propag.*, vol. 50, no. 9, pp. 1212–1221, Sept. 2002.

[123] R. F. Harrington, *Time-Harmonic Electromagnetic Fields.* Wiley-IEEE Press, 2001.

[124] K. Donepudi, J.-M. Jin, S. Velamparambil, J. Song, and W. C. Chew, “A higher order parallelized multilevel fast multipole algorithm for 3-D scattering,” *IEEE Trans. Antennas Propag.*, vol. 49, no. 7, pp. 1069–1078, July 2001.

[125] D. Ding, R.-S. Chen, Z. Fan, and P. Rui, “A novel hierarchical two-level spectral preconditioning technique for electromagnetic wave scattering,” *IEEE Trans. Antennas Propag.*, vol. 56, no. 4, pp. 1122–1132, Apr. 2008.

[126] T. F. Eibert, “Some scattering results computed by surface-integral-equation and hybrid finite-element – boundary-integral techniques, accelerated by the multilevel fast multipole method,” *IEEE Antennas Propag. Mag.*, vol. 49, no. 2, pp. 61–69, Apr. 2007.

[127] Ismatullah, C. H. Schmidt, and T. F. Eibert, “Nearly-orthogonal hierarchical vector basis functions employed for the discretization of inverse equivalent surface currents,” in *31st Annual AMTA Symposium*, Salt Lake City, Utah, USA, Nov. 1-6, 2009.

[128] A. Tzoulis and T. Eibert, “Efficient electromagnetic near-field computation by the multilevel fast multipole method employing mixed near-field/far-field translations,” *IEEE Antennas Wireless Propag. Lett.*, vol. 4, pp. 449–452, 2005.

[129] Ismatullah and I. E. Rana, “Implementation of the jacobi-bessel series method for radiation-pattern equations of an offset parabolic reflector antenna using mathcadő,” *IEEE Antennas Propag. Mag.*, vol. 47, no. 3, pp. 99–104, June 2005.

[130] Ismatullah and T. Eibert, “Modeling and design of offset parabolic reflector antennas using physical optics and multilevel fast multipole method accelerated method of moments,” *Multitopic Conference, 2006. INMIC ’06. IEEE*, pp. 377–382, Dec. 2006.

[131] R. Haupt, “Adaptive reflector antenna using smart resistive sheets,” *Electron. Lett*, vol. 42, no. 22, pp. 1257–1258, Oct. 2006.

Index